

**REPUBLIC OF TURKEY
AYDIN ADNAN MENDERES UNIVERSITY
GRADUATE SCHOOL OF NATURAL AND APPLIED SCIENCES
MECHANICAL ENGINEERING
2019-Ph.D.-**

**DESIGN AND DEVELOPMENT OF AN
UNMANNED AERIAL AND GROUND VEHICLES
FOR PRECISION PESTICIDE SPRAYING**

Fatih AKKOYUN

**Supervisor:
Prof. Dr. İsmail BÖĞREKÇİ**

AYDIN

REPUBLIC OF TURKEY
AYDIN ADNAN MENDERES UNIVERSITY
GRADUATE SCHOOL OF NATURAL AND APPLIED SCIENCES
AYDIN

The thesis with the title of “DESIGN and DEVELOPMENT of an UNMANNED AERIAL and GROUND VEHICLES for PRECISION PESTICIDE SPRAYING” prepared by the Fatih AKKOYUN, PhD Student at the Mechanical Engineering Program at the Department of Mechanical Engineering was accepted by the jury members whose names and titles presented below as a result of thesis defense on 24.12.2019.

	Title, Name Surname	Institution	Signature
<i>President :</i>	Prof. Dr. İsmail BÖĞREKÇİ	Aydın Adnan Menderes University	
<i>Member :</i>	Prof. Dr. Zeki KIRAL	Dokuz Eylül University	
<i>Member :</i>	Prof. Dr. Hasan ÖZTÜRK	Dokuz Eylül University	
<i>Member :</i>	Assoc. Prof. Dr. Pınar DEMİRCİOĞLU	Aydın Adnan Menderes University	
<i>Member :</i>	Asst. Prof. Dr. Adem ÖZÇELİK	Aydın Adnan Menderes University	

This Doctorate Thesis accepted by the jury members is endorsed by the decision of the Institute Board Members with Serial Number and date.

Prof. Dr. Gönül AYDIN
Institute Director

REPUBLIC OF TURKEY
ADNAN MENDERES UNIVERSITY
GRADUATE SCHOOL OF NATURAL AND APPLIED SCIENCES
AYDIN

I hereby declare that all information and results reported in this thesis have been obtained by my part as a result of truthful experiments and observations carried out by the scientific methods, and that I referenced appropriately and completely all data, thought, result information which do not belong my part within this study by virtue of scientific ethical codes.

24/12/2019

Signature

Fatih AKKOYUN

ÖZET

HASSAS TARIMSAL İLAÇLAMA İÇİN İNSANSIZ HAVA VE KARA ARAÇLARI TASARLANMASI VE GELİŞTİRİLMESİ

Fatih AKKOYUN

Doktora Tezi, Makine Mühendisliği

Tez Danışmanı: Prof. Dr. İsmail BÖGREKÇİ

2019, 167 s.

Günümüzde, bitki hastalıkları tarımsal üretimi etkileyen önemli sorunlardan birisi olarak karşımıza çıkmaktadır. Bitkileri hastalıklardan ve zararlı otların etkilerinden korumak hem tarımda üretimi artırmak hem de tarımın kalitesini yükseltmek için büyük önem taşımaktadır. Tarımsal ürünler, ülkemizde ve dünyada çeşitli ilaçlama yöntemleri kullanılarak korunabilmektedir. Bu yöntemlerin başında gelen ilaçlama yolu ile bitki koruma yöntemi üretimin kalitesini geliştirmek ve reelteyi artırmak amacıyla yaygın olarak kullanılmaktadır. Ancak bitkilerin korunmasında uygulanan geleneksel ilaçlama yöntemlerinin bitkilere ve toprağa büyük ölçüde zarar verdiği gözlenmektedir.

Son yıllarda gelişmiş ülkelerdeki tarımsal uygulamalarda robotların kullanımı hızla artmakta, tarımsal alanlarda özellikle uzaktan algılama ve hassas tarım çalışmalarında bu robotların kullanıldığı görülmektedir. Dahası, tarımsal üretimde yararlanılan fayda-maliyet oranı da dikkate alındığında, günümüzde hassas tarım uygulamalarında robotların kullanılmasının kaçınılmaz hale geldiği anlaşılmaktadır.

Günümüz gereksinimleri ve gelişen teknoloji göz önüne alınarak planlanmış olan bu çalışmada, ülkemizde yaygın olarak kullanılan tarımsal mücadele yöntemlerinin maliyetlerini, tarımsal üretimin miktarını ve kalitesini önemli ölçüde etkileyecek geleneksel ilaçlama yöntemlerine alternatif olabilecek bir tarımsal mücadele sistemi geliştirilmiştir. Çalışmada, yakın mesafeden doğrudan hedeflenen bitki üzerine ilaçlama yapılması, ilaçlama sırasında toprağa ve bitkilere verilen zararın en aza indirgenmesi hedeflenmiştir. Bu doğrultuda, özgün tasarım multispektral kamera, ilaçlama ünitesi, Yer Kontrol İstasyonu (YKİ) ve eşgüdümlü çalışabilen İnsansız Hava Aracı (İHA) ile İnsansız Yer Aracından (İYA) oluşan tarımsal mücadele mekanizması tasarlanmış ve geliştirilmiştir. Bu mekanizma, tarımsal ilaçlama uygulamaları için geleneksel yöntemlere kıyasla daha ileri düzey bir alternatif yöntem olarak ortaya çıkmaktadır.

Anahtar Kelimeler: Hassas Tarım, İHA, İYA, Uzaktan Algılama, Seçmeli İlaçlama.

ABSTRACT

DESIGN AND DEVELOPMENT OF AN UNMANNED AERIAL AND GROUND VEHICLES FOR PRECISION PESTICIDE SPRAYING

Fatih AKKOYUN

PhD Thesis, Mechanical Engineering

Supervisor: Prof. Dr. İsmail BÖĞREKÇİ

2019, 167 pp.

Nowadays plant diseases are one of the major problems for crop yields. To prevent negative effects of the plant diseases, enhancing the quality of products and reducing the costs are important elements for ideal crop yields. Crops can be protected from diseases using various methods. In agricultural pest control, it is inevitable to use pesticide spraying methods to improve product quality and increase the production rate. However, mostly the pesticide applications for plant protection are done by using traditional spraying methods that cause harmful effects on plants and soil.

In recent years, the use of robots in farming fields is swiftly increasing in developed countries especially in precision farming and remote sensing applications. At present, it became a necessity to use of robots in agriculture when examined to benefit-cost ratio.

Considering the fact that advanced technology and developmental needs, in this thesis, aerial and ground vehicles were developed for precision pesticide spraying to decrease the negative effects of chemicals, reduce the usage of pesticides and minimize toxic effects of conventional spraying applications. For this purpose, this study focuses on the agricultural pesticide spraying that sprays pesticides directly on plants to minimize the negative effects of pesticides on plants and soil. In line with this purpose a pest control system that consists of a custom-designed multispectral camera, a spraying unit, a Ground Control Station (GCS) and a co-operated Unmanned Aerial Vehicle (UAV) with Unmanned Ground Vehicle (UGV) were designed and manufactured. This system is an advanced pesticide spraying alternative in contrast with traditional methods for agricultural pesticide applications.

Keywords: Precision Farming, UAV, UGV, Remote Sensing, Selective Spraying

ACKNOWLEDGEMENTS

I would like to express my special appreciation and thanks to my advisor Prof. Bogrekci, who has been a tremendous mentor for me. I would like to thank him for encouraging my research and for allowing me to grow as a research scientist. I am grateful to Prof. Demircioglu, the precious support and fairness of whom lift the courage of all around her. I would like to thank to Prof. Kiral for his invaluable presence in my committee and rewarding advices.

Special thanks to my dear colleagues Orcun Ekin and Salih Vardin for their invaluable advice and feedback on my research and for always being so supportive of my work. I would also like to thank Halil İbrahim Taskaya and Nihat Bilge for their precious contributions.

Fatih AKKOYUN

TABLE OF CONTENTS

ÖZET	vii
ABSTRACT	ix
ACKNOWLEDGEMENTS	xi
1 . INTRODUCTION	1
2. LITERATURE REVIEW	6
2.1 Robotics	9
2.2 Unmanned Ground Vehicles	11
2.3 Unmanned Aerial Vehicles	11
2.4 Remote Sensing Technology	17
2.4.1 Remote Sensing Platforms	19
2.4.2 Plant Disease Detection	22
2.4.3 Normalized Difference Vegetation Index	27
3 . MATERIAL AND METHOD	29
3.1 Ground Control Station	32
3.2 Unmanned Ground Vehicle	37
3.2.1 Specifications of the UGV	38
3.2.2 The Chassis and Sensor Holder	40
3.2.3 FEM Analysis.....	43
3.3 Multispectral Camera for Plant Disease Detection	44
3.3.1 Spectral Imaging.....	46

3.3.2 Multispectral Camera – Spektra TSL128RN	47
3.3.3 The hardware of the Device	49
3.3.4 Calibrating Steps of the Device.....	52
3.3.5 Software for the Device	56
3.3.6 Measurements using NDVI Devices	58
3.4 Unmanned Aerial Vehicle	62
3.4.1 The Chassis and Arm.....	66
3.4.2 FEM Analysis	69
3.4.3 Modal Analysis	70
3.4.4 Performance of the Propellers	73
3.4.5 Flight Duration and Maximum Conditions	82
3.4.6 Strain Measurement.....	84
3.4.7 Other Parts	92
3.4.8 Specifications of the UAV	95
3.4.9 Flight Tests	96
3.5 Spraying Unit –Sprayer and Tank.....	99
4 . RESULTS AND DISCUSSION.....	103
4.1 The UGV	103
4.2 The Multispectral Camera	105
4.3 The UAV	115
4.4 The Sprayer.....	135

4.5 UGV and Multispectral Camera..... 138

4.6 Aerial Spraying UAV 145

5 . CONCLUSIONS..... 154

REFERENCES 156

RESUME..... 165



LIST OF ABBREVIATIONS

BDC	: Brushed Direct Current Motor
BLDC	: Brushless Direct Current Motor
CCW	: Counter Clockwise
CW	: Clockwise
DC	: Direct Current
dd	: Decimal degrees.
D-GPS	: Differential GPS
FoV	: Field of View
GCS	: Ground Control Station
GIS	: Geographic Information System
GPS	: Global Positioning System
HFoV	: Horizontal Field of View
LAI	: Leaf Area Index
NDVI	: Normalized Difference Vegetation Index
PCB	: Plastic Circuit Board
RPV	: Remotely Piloted Vehicle
RPM	: Revolutions Per Minute
RTK-GPS	: Real Time Kinematic GPS
sUAV	: Small Unmanned Aerial Vehicle
UAS	: Unmanned Aircraft System

UAV : Unmanned Aerial Vehicle

UGV : Unmanned Ground Vehicle

VFoV : Vertical Field of View

W : Watt



LIST OF FIGURES

Fig. 1.1. Well-structured soil (a), compacted soil (b) (Soil Works LLC, 2019).	2
Fig. 1.2. Spraying methods in agriculture (hand spraying machines (a), ground vehicles(b), aerial vehicles(c), unmanned vehicles(d)).	3
Fig. 1.3. Expected annual UAV sales for agriculture, public safety, and other markets (Jenkins and Vasigh 2013).	4
Fig. 1.4. The general structure of the developed system.....	5
Fig. 2.1. Conventional pesticide spraying methods.	6
Fig. 2.2. Ground vehicles (Tractors).	6
Fig. 2.3. Compacted soil examples from farming lands caused by ground vehicles (Aldaz, 2019).	7
Fig. 2.4. Pesticide drift caused by the distance of the sprayer mechanism of Piloted Aircraft (Beyond Pesticides Daily News Blog, 2019).	7
Fig. 2.5. Risking practitioner health (Kijewski, 2019).	8
Fig. 2.6. UAVs (a) Hummingbird, (b) Phantom Eye	12
Fig. 2.7. Estimated annual sales of Unmanned Aircraft Systems (Teal Group, 2017).	12
Fig. 2.8. Worldwide spending (\$bn) for UAVs (SIPRI, 2016).	13
Fig. 2.9. Sense and Avoid in UAS Research and Applications, (Limnaios et al., 2012).	13
Fig. 2.10. UAV Nomenclature Designation (U.S. Department of Defense, 2013).	14
Fig. 2.11. VTOL UAS (a) Draganflyer X6 VTOL UAS, (b) Yamaha RMAX VTOL aircraft.	15

Fig. 2.12. Classification of UAVs by range and altitude based (Eisenbei 2009)...	16
Fig. 2.13. Active and Passive Remote Sensors.....	18
Fig. 2.14. View of Earth from a camera on V-2 #13, launched on October 24, 1946, (Reichhardt, 2006).....	18
Fig. 2.15. The accuracy of measurement methods in relation to the object/area size (Limnaios et al., 2012).....	20
Fig. 2.16. Strengths and Weaknesses of UAVs and UGVs (Limnaios et al., 2012).	21
Fig. 2.17. Remote Sensing in farming, visible spectrum imaging (a), satellite-based thermal imaging (b), aircraft based thermal imaging (c).....	21
Fig. 2.18. Basic block diagram of commonly used Photodiode sensor.	22
Fig. 2.19. Advanced method output, spectral image data set (a), confocal image (b), lambda stack (c).....	23
Fig. 2.20. The percentage spectral reflectance of Austroepatorium inulifolium leaves. Each line of different colors represents measurements taken from separate plants. (Piyasinghe et al., (2018).	24
Fig. 2.21. A multispectral image from the DMCii satellite.	25
Fig. 2.22. Typical reflectance spectra of plants.	25
Fig. 2.23. Reflectance spectra of water, soil and vegetation in different wavelengths (SEOS, 2017).	26
Fig. 2.24. The reflectance of typical green vegetation in different wavelengths (SEOS, 2017).	26
Fig. 2.25. NDVI calculation example.	28
Fig. 3.1. Plant disease detecting and pesticide spraying steps.	29
Fig. 3.2. The relationship between major units.	30

Fig. 3.3. The relationship between control loop mechanisms.	30
Fig. 3.4. Schematic diagram of the precision spraying mechanism.	31
Fig. 3.5. Flowchart of the plant protection loop.	33
Fig. 3.6. Wireless communication between major units.	34
Fig. 3.7. Remote sensing system block diagram.....	35
Fig. 3.8. Plant disease-locating unit and GCS receiver.	35
Fig. 3.9. Scanning the target field for plant disease detection.	36
Fig. 3.10. 3D model of the designed UGV.....	37
Fig. 3.11. 3D Model (a) and assembly (b) of the UGV.....	40
Fig. 3.12. Block diagram of the UGV.....	41
Fig. 3.13. The layout of motor drivers and wiring.....	41
Fig. 3.14. The UGV with the sensor holder.....	42
Fig. 3.15. Chassis FEM.....	43
Fig. 3.16. Flanged coupler FEM.....	43
Fig. 3.17. OpenCV Image processing examples, primitive shape distance detecting (a), original image for plant disease detecting (b).	45
Fig. 3.18. The bitmap of a 24 Bit 320x240 pixel RGB Image.....	46
Fig. 3.19. Typical spectral reflectance of plants.	46
Fig. 3.20. Spectral image and reflectance of a plant.	47
Fig. 3.21. Reflectance of plant, water and soil.	47
Fig. 3.22. 3D model of the Multispectral Camera.	48

Fig. 3.23. Block diagram of the Multispectral Camera.	48
Fig. 3.24. Photodiode spectral responsivity.	50
Fig. 3.25. Schematic design of the board.	51
Fig. 3.26. The printable design of the board.....	51
Fig. 3.27. 3D Model of the board (a) and the Printed Circuit Board (PCB) (b). ...	52
Fig. 3.28. Relationship between Focal Length, FoV and sensor size.	52
Fig. 3.29. The 3D model of sensor and sensing area relationship (a) and simulation of the FoV (b).	53
Fig. 3.30. Calculation of the intersecting area.	54
Fig. 3.31. FoV of the sensors, vertical FoV (a), horizontal FoV (b).	54
Fig. 3.32. Intersecting parts for horizontal FoV.	54
Fig. 3.33. Focal Length Adjusting	56
Fig. 3.34. Adjustment focal length and target object distance of Varifocal lenses.	56
Fig. 3.35. Desktop Software for Calibration of Multispectral Camera.	57
Fig. 3.36. Desktop software for image acquisition of the multispectral camera. ..	57
Fig. 3.37. Multispectral Camera assembly.	58
Fig. 3.38. Multispectral camera units: electronic board and lenses (a), filters and laser module (b).	58
Fig. 3.39. PlantPen NDVI 300- NDVI.	59
Fig. 3.40. Sample plants, readings using Plant Pen NDVI device and categorized four different statuses of the sample plants.	60
Fig. 3.41. Raw data example.	61

Fig. 3.42. Fig tree leaves and grass.	61
Fig. 3.43. The multispectral camera and plane tree leave with dark red to brown background.	62
Fig. 3.44. Assembly of the UAV.	63
Fig. 3.45. Block Diagram of UAV.	64
Fig. 3.46. UAV Chassis 3D model (Isometric view).	67
Fig. 3.47. Draft of the UAV chassis for manufacturing.	67
Fig. 3.48. UAV prototyping images.	68
Fig. 3.49. Chassis FEA.	69
Fig. 3.50. VTOL UAV Arm design.	70
Fig. 3.51. Modal test setup.	70
Fig. 3.52. 3 Axis accelerometer and Modal Hammer.	71
Fig. 3.53. The shape of the UAV with defined Nodes and Traces.	71
Fig. 3.54. Three times repetition.	72
Fig. 3.55. First five mode shapes of a free-free beam (Chellapilla, 2016).	72
Fig. 3.56. Natural frequency analysis of the UAV chassis.	72
Fig. 3.57. Forces on a blade such as lift and drag (Propeller Theory, 2019).	73
Fig. 3.58. Schematic of a propeller propulsion system (McCormick, 1979).	74
Fig. 3.59. 3D Model of the propeller test mechanism a) precision scale, b) Junction point of the chassis and arm c) motor and gear reducer parts mounted on the motor holder, d) 3010 carbon fiber propeller.	77
Fig. 3.60. 3010 (a) and 3095 (b) propellers.	78

Fig. 3.61. Lever mechanism and VTOL UAV Arm lay-out.	78
Fig. 3.62. Power and angular velocity measurement method.	79
Fig. 3.63. VTOL UAV arm setup.	79
Fig. 3.64. Mounting of the gear reducer and the propeller.	80
Fig. 3.65. Measuring equipment: Oscilloscope, Multimeter, Current Clamp, IR Tachometer, Joystick and PWM Generator Board (a), Thrust testing mechanism (b).	80
Fig. 3.66. Thrust testing apparatus and measuring equipment.	81
Fig. 3.67. Measurand of the test system.	82
Fig. 3.68. Forces on a UAV.	82
Fig. 3.69. Maximum Strain on the VTOL UAV arm (isometric view).	85
Fig. 3.70. Maximum Strain on the VTOL UAV arm.	85
Fig. 3.71. Bridge on VTOL UAV Arm.	86
Fig. 3.72. Rosette type strain gauge layout.	86
Fig. 3.73. Block diagram of the strain measurement system.	87
Fig. 3.74. Shield Grounding for Noise Reduction	88
Fig. 3.75. The bridge on the VTOL UAV Arm.	89
Fig. 3.76. Strain on the X axis.	90
Fig. 3.77. Strain on the Y axis.	91
Fig. 3.78. Strain on the XY axis.	91
Fig. 3.79. Main Gear.	92
Fig. 3.80. Main gear tensile tests.	93

Fig. 3.81. Cross-section view of the designed gear reducer (draft for manufacturing).	93
Fig. 3.82. Schematic of the PDB.	95
Fig. 3.83. The small UAV.	96
Fig. 3.84. Flight logs for Square path.....	97
Fig. 3.85. Flight logs for S-line path.	97
Fig. 3.86. The small UAV in the test field.	98
Fig. 3.87. The spraying unit.....	100
Fig. 3.88. Sprayer units and layout.	100
Fig. 3.89. SEM image of a sponge (Wu et al., 2015).	101
Fig. 3.90. Image of the tank with and without the foam.	101
Fig. 3.91. Full-cone nozzle.	102
Fig. 3.92. Spraying area calculation.	102
Fig. 4.1. The UGV.	104
Fig. 4.2. FEA result of the UGV.....	104
Fig. 4.3. Structural static analysis for the flanged coupler of the UGV.	105
Fig. 4.4. The multispectral camera (Spektra TSL128-RN).	105
Fig. 4.5. Image from the NDVI measurement for grass.....	107
Fig. 4.6. NIR and Red band outputs of the grass from the Spektra TSL128-RN.	107
Fig. 4.7. NDVI outputs of the grass from the Multispectral camera.	107
Fig. 4.8. NIR and Red band outputs of fig tree leaves from the Spektra TSL128-RN.	108

Fig. 4.9. NDVI outputs of fig tree leaves from the Spektra TSL128-RN.	108
Fig. 4.10. Planetree leaves for NDVI measurement.	109
Fig. 4.11. NIR and Red band output of Planetree leaves from the Multispectral Camera.	109
Fig. 4.12. NDVI output of Planetree leaves from the Multispectral Camera.	110
Fig. 4.13. Plant disease detection test.	110
Fig. 4.14. Test leaves for plant disease detection.	111
Fig. 4.15. Scanning process and direction.	111
Fig. 4.16. NDVI results for three scanned leaves.	113
Fig. 4.17. NDVI result chart for three scanned leaves.	114
Fig. 4.18. NDVI and LAI composed result chart for three scanned leaves.	114
Fig. 4.19. Manufactured VTOL UAV.	115
Fig. 4.20. Stress concentration on chassis.	116
Fig. 4.21. Stresses on joints.	116
Fig. 4.22. Strain result.	117
Fig. 4.23. FoS result.	117
Fig. 4.24. Displacement result.	118
Fig. 4.25. VTOL UAV Arm Stress (a), Strain (b), FoS (c) and displacement (d) analysis results.	119
Fig. 4.26. Power - angular velocity relationship.	124
Fig. 4.27. Power - thrust relationship.	124
Fig. 4.28. Thrust - angular velocity relationship.	125

Fig. 4.29. Theoretical vs experimental result comparison for propeller 3010.....	126
Fig. 4.30. Theoretical vs experimental thrust of the 3095 Propeller	126
Fig. 4.31. Flight duration of the UAV.....	127
Fig. 4.32. The strain on the 3010 propeller for 524 Rad/s.....	128
Fig. 4.33. The effect of the centrifugal force on the 3010 propeller for 524 Rad/s.	128
Fig. 4.34. The measured relationship among battery weight, payload and flight duration.	129
Fig. 4.35. Maximum Strain on the VTOL UAV arm (side view).....	129
Fig. 4.36. Principal Strain comparison.....	131
Fig. 4.37. Shear Strain comparison.	132
Fig. 4.38. Main Gear Analysis.....	132
Fig. 4.39. 3D Printed Main Gear.	133
Fig. 4.40. Manufactured gear reducer assemble.	134
Fig. 4.41. Aluminum Power Distribution Board.....	134
Fig. 4.42. Sprayer UAV.	135
Fig. 4.43. The sprayer.	136
Fig. 4.44. Spraying area for the 1.5 m boom with four nozzles.....	137
Fig. 4.45. Spraying pattern for the 1.5 m boom with four nozzles.	137
Fig. 4.46. Images from field tests.	138
Fig. 4.47. The mounted gimbal and the multispectral camera on the UGV.	139
Fig. 4.48. Planted cucumbers in the planter.	139

Fig. 4.49. NDVI result of the cucumber plant.	139
Fig. 4.50. Extended image for NDVI result of the cucumber plant.	140
Fig. 4.51. Healthy Percentage using NDVI with LAI.	141
Fig. 4.52. NDVI Data including only Vegetation.	141
Fig. 4.53. NDVI Data for under 0.5.	142
Fig. 4.54. Planted cucumbers in the planter.	142
Fig. 4.55. Spectral band results for planted cucumbers in the planter.	144
Fig. 4.56. Healthy Percentage using NDVI with LAI.	144
Fig. 4.57. NDVI Data including only Vegetation.	144
Fig. 4.58. NDVI Data for under 0.66.	145
Fig. 4.59. The small UAV in the test field and flight log.	145
Fig. 4.60. Spraying pattern testing setup.	147
Fig. 4.61. Spraying pattern for 1-meter height while UAV is hovering, front view (a), side view (b).	148
Fig. 4.62. Spraying pattern for 2-meter height while UAV is hovering, front view (a), side view (b).	150
Fig. 4.63. Spraying pattern for 1-meter height with (b) and without (a) propeller effect.	151
Fig. 4.64. Spraying pattern for 2-meter height with (b) and without (a) propeller effect.	151

LIST OF TABLES

Table 1.1. Worldwide crop losses are due to pests, diseases and weeds (Arya and Perelló 2010).	2
Table 2.1. Precision and conventional farming pros and cons (Katalin, 2011).	8
Table 2.2. Comparison of Small Unmanned Aerial Systems (Stark, Smith, and Chen 2013).	16
Table 2.3. Pros and cons of the different type of UAVs (levels: high=2; medium=1; low=0) (Eisenbei 2009).	21
Table 2.4. Overall accuracies for classifying 6 crop species.	23
Table 2.5. Different wavelengths used for measuring NDVI.	28
Table 3.1. Raw Data acquired by UGV.	36
Table 3.2. Specifications of the UGV.	39
Table 3.3. Components of the UGV.	39
Table 3.4. Components of the Multispectral Camera.	49
Table 3.5. Components of the VTOL UAV.	65
Table 3.6. Components of the VTOL UAV (Continued).	66
Table 3.7. Electronic components used for data acquisition and their descriptions.	88
Table 3.8. Material properties of pure Copper and Aluminum (Meulenbroeks, 2014).	93
Table 3.9. Market price properties of pure Copper and Aluminum (Meulenbroeks, 2014).	94
Table 3.10. Specifications of the UAV.	96

Table 3.11. S-line path target coordinates.	98
Table 3.12. Square path target coordinates.	99
Table 3.13. Z-line path target coordinates.	99
Table 3.14. Sprayer properties.	100
Table 4.1. PlantPen 300 NDVI device test results.	106
Table 4.2. Color gradient for spectral bands.	106
Table 4.3. Scanning sequence of the Spektra TSL128-RN.	108
Table 4.4. Multispectral Camera outdoor field test results.	108
Table 4.5. Spektra TSL128-RN indoor test results.	110
Table 4.6. FEA analysis result of the VTOL UAV chassis.	115
Table 4.7. Experimental Modal Test result.	119
Table 4.8. Mode Shapes.	119
Table 4.9. Modal analysis result.	120
Table 4.10. Modal analysis result comparison.	121
Table 4.11. 3095 propeller theoretical results.	121
Table 4.12. 3010 propeller theoretical results.	121
Table 4.13. 3010 propeller experimental test results.	122
Table 4.14. 3010 propeller temperature test results.	122
Table 4.15. 3010 propeller performance test results.	123
Table 4.16. 3095 propeller temperature test results.	123
Table 4.17. RMSE values for the 3010 and 3095 Propeller.	126

Table 4.18. Maximum flight conditions for the UAV.....	126
Table 4.19. Weight and Payload Relationship for the UAV.	128
Table 4.20. Force vs voltage relationship in theory.	129
Table 4.21. Experimental strain results.	130
Table 4.22. SolidWorks simulation results.....	131
Table 4.23. Main gear tensile tests results.....	133
Table 4.24. Specifications of the Aluminum PDB.....	135
Table 4.25. Tank with sponge.	136
Table 4.26. Tank without sponge.....	136
Table 4.27. Positioning deviation in meters.	146
Table 4.28. Spraying distance and spraying pattern comparison.....	152

LIST OF APPENDICES

- 1- Embedded Codes and Desktop Software
- 2- Drawings of the UAV and UGV
- 3- Analysis Results for UAV and UGV (FEA and CFD)



1. INTRODUCTION

Plant diseases are one of the major problems for crop yields. Pesticide chemicals are commonly used in traditional pest control to protect plants from these diseases in agriculture (TCTOB 2017). The most common method of pest control is the usage of pesticides that either kill pests or inhibit their development (Sarwar 2015).

Pesticide consists of chemicals to remove the harmful effects of pests from a diseased plant. Half of all pesticides that common in agricultural applications are used on the five main crops, cereals, corn, rice, cotton and soya. It is a well-known fact that the hazards of chemical pesticide usage, although statistics are difficult to gather about its hazardous. According to the World Health Organization (WHO), pesticides are causing more than 200,000 root losses every year and poisoning at least three million people. It is estimated that about 25 million agricultural workers are poisoned from spraying applications every year (Abdou 2018; Jeyaratnam 1990). Present chemical pesticides used in spraying applications are much more fading, but they may consist of highly toxic content to some non-target organisms. Pesticide leaks in watercourses mainly by way of direct spraying application, aerial spray drift and run-off from treated areas. Groundwater feeds soil and moves slowly and once its water sources are contaminated, they may remain so for many decades.

Chemical pesticides are powerful and effective solutions for protecting farming fields. Usage of pesticides protects the crop health and improves the crop yield by increasing the farming efficiency. Mostly, farmers and foresters choosing the pesticide spraying method as a first option in order to protect farming fields from the diseases. In 1998, herbicides accounted for 49% of world pesticide use, followed by insecticides at 27%, fungicides at 20% et al. 4% (Wetzel, Duchesne, and Laporte 2006).

Conservative estimates of total annual losses in crop production by diseases, insects and weeds worldwide are 220 billion US\$ corresponding to 31-42% of all losses indicated in Table 1 (Arya and Perelló 2010).

Table 1.1. Worldwide crop losses are due to pests, diseases and weeds (Arya and Perelló 2010).

Crop Losses due	Percentage (%)
Diseases	14.1
Insects	10.2
Weeds	12.2
Total av. losses	36.5

According to the marketing researches on global crop protection using chemicals, it is estimated to be valued around USD 54.89 Billion in 2016. And it is projected to reach up to USD 70.57 Billion by 2021 (MarketsandMarkets 2016).

In our country, commonly used pesticide spraying methods can be classified into three categories: ground vehicle, aerial vehicle and hand spray machines. Ground vehicles are widely used for spraying pesticide on plants that causes soil compaction and damage on plant roots. These vehicles exert waste gas that directly pollutes agricultural plants.

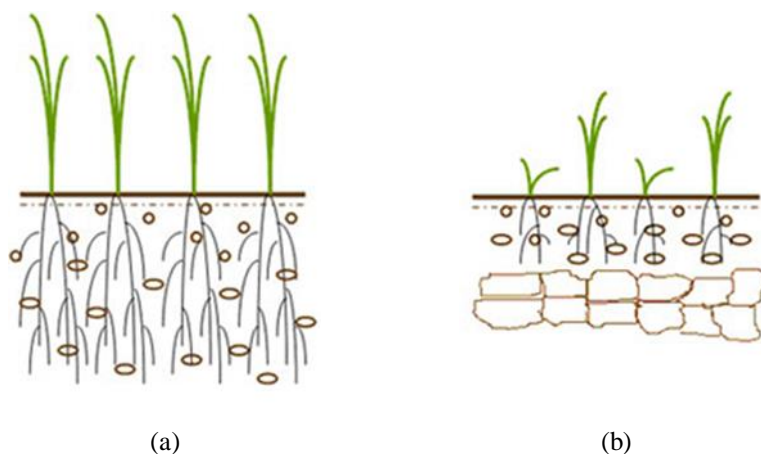


Fig. 1.1. Well-structured soil (a), compacted soil (b) (Soil Works LLC, 2019).

Conventionally used aerial vehicles for pesticide spraying are named piloted aerial vehicles. These vehicles mainly have no ability to spray pesticides on the plants from close distances because of the safe flying altitude requirement. The altitude, the wind affects dispersion and the drift caused by aircraft decreases the efficiency of pesticides. It requires qualified personnel with the high cost to perform it. Hand

spray machines are one of the commonly used pesticide spraying methods. This method requires manpower and risks practitioner health. Typically, it is used to spray pesticides for small scale areas.

Conventional methods are not the entire solution for plant protection. It is obvious that using these methods decreases the efficiency of crop fields, negatively affect farming fields by using more chemicals. These methods affect soil, plants as well as plant roots and increases the farming costs, therefore are not adequate for precision farming.

In agricultural pest control, to improve product quality and increase production rate, it is inevitable to use precision pesticide spraying vehicles instead of conventional spraying methods.

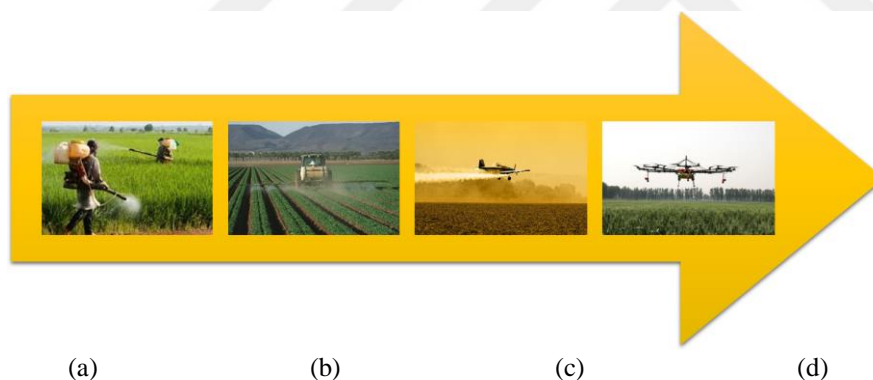


Fig. 1.2. Spraying methods in agriculture (hand spraying machines (a), ground vehicles(b), aerial vehicles(c), unmanned vehicles(d)).

Precision farming is a farming management concept based on managing inputs at required quantity hence it provides economic benefit in crops and reduces the effect of environmentally hazardous substances. It aims to limit inputs, raise effectiveness with the help of control systems, avoid waste of resources, increase gross yield. More specifically, precision farming aims to decrease expense of chemicals such as fertilizer and pesticide, reduce harmful effects to the environment, provide quality product in high quantity and effective flow of information for crop management (Jenkins and Vasigh 2013; TCTOB 2017).

Plant protection is the process that protects plants from diseases and other pests to increase crop yields and its quality (TCTOB 2017). For this purpose, agricultural

pesticide spraying is used for plant protection as an agricultural pest control method. In our country, plant diseases are the common factor that affects crop yields and stand against the optimization principle of precision farming.

Nowadays with the help of advanced technology, UAV production costs are decreasing and their abilities are continuously increasing. In developed countries, UAVs are widely used and expanding in agriculture, especially in precision farming and remote sensing applications. Many experts forecast that the usage of UAVs will rise swiftly in agricultural applications (Toscano, M., 2016). Recent years UAVs step forwards most especially in commercial agriculture and in the future it is foreseen that 80% of UAV applications will be related to agricultural applications (Camhi 2016; Unmanned Vehicle University 2016).

Developed countries extensively use robots in agriculture for controlling agricultural lands. In agriculture, the usage of UAVs and UGVs are centered on precision farming and remote sensing applications. Remote sensing in agriculture provides information about plant health problems, growth rates, hydration and diseases. In precision farming, UAVs helps to improve pesticide spraying and control the status of the health of the crops (Jenkins and Vasigh 2013). Today, some developed countries have the ability to spray plants about one-meter altitude using UAVs. As an example, UAVs are used for spraying rice fields in Japan (Unmanned Vehicle University 2016).

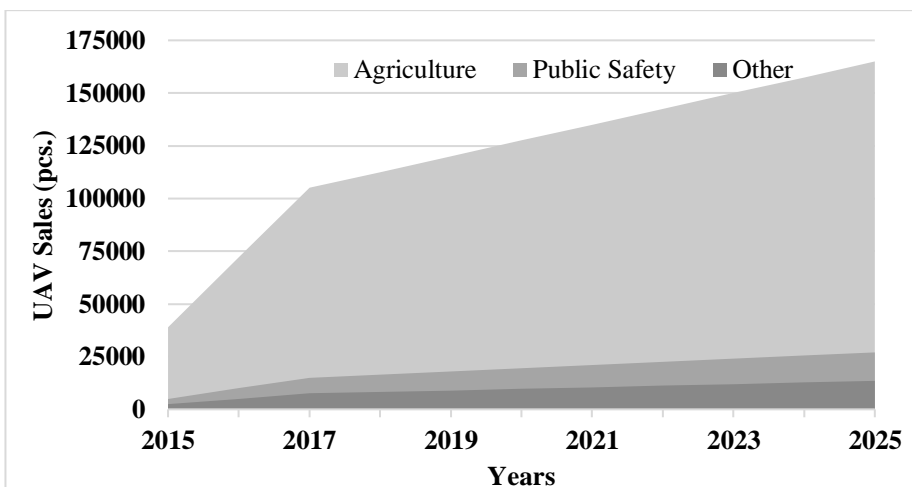


Fig. 1.3. Expected annual UAV sales for agriculture, public safety, and other markets (Jenkins and Vasigh 2013).

With the help of advanced technology, robots could provide adequate precision pesticide spraying applications for precision farming. Taking into account the selective pesticide spraying requirement for the agricultural pest control applications and the possibilities of the advanced technology, an alternating agricultural pest control system is developed in order to use for precision pesticide spraying. The aim of the thesis study is to develop a precision pesticide spraying system, using coordinated UAV and UGV in order to provide an alternative solution among conventional spraying methods. Remote monitoring and coordination processes between these units achieved using a personal computer (PC) as a Ground Control Station (GCS). In line with this direction, an aerial and a ground robot with a spectral imaging sensor are designed, developed and manufactured. It is proposed that the developed system limits the usage of chemicals for pesticide spraying, increases the efficiency of the crop fields and decreases production costs. The general structure of the developed system is shown in Fig 1.4.

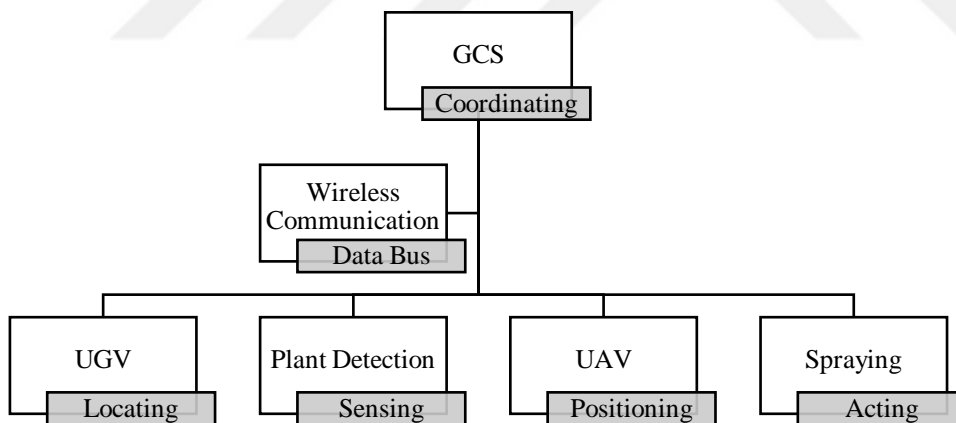


Fig. 1.4. The general structure of the developed system

2. LITERATURE REVIEW

In order to protect plants, using non-chemical methods there are alternative solutions such as cultivation for pest and weed control, biological applications for pest control, mechanical and laser cutting applications for weed control. However today, pesticide spraying is playing a dominant role in plant protection applications. Typically, conventional methods for pesticide spraying are used widely in farming. These spraying methods are mainly classifiable by three as ground vehicles, aerial vehicles and hand spray machines shown in Fig. 2.1, respectively.



Fig. 2.1. Conventional pesticide spraying methods.

In pesticide spraying applications, ground vehicles (Fig. 2.2) are commonly preferred for spraying due to their high carrying capability and wide spraying ranges. However, these vehicles have adverse effects such as soil compaction, which is indicated in Fig. 2.3, cause damage to plants especially harm their roots and exert waste gas over the plants.



Fig. 2.2. Ground vehicles (Tractors).



Fig. 2.3. Compacted soil examples from farming lands caused by ground vehicles (Aldaz, 2019).

Piloted aerial vehicle (Fig. 2.4) is an alternative solution that used in long-range pesticide spraying applications. These vehicles are not able to spray pesticides closer to the plant due to their safe flying altitude. The flying altitude and the wind affect dispersion and the drift caused by aircraft decreases the efficiency of pesticide applications. It requires qualified and skilled pilots with high labor costs to do it.



Fig. 2.4. Pesticide drift caused by the distance of the sprayer mechanism of Piloted Aircraft (Beyond Pesticides Daily News Blog, 2019).

Hand spray machine is a common pesticide spraying method in conventional farming that is not adequate for spraying large-scale farming fields. This method (Fig. 2.5) requires manpower and risks practitioner health. Typically, it is used to spray pesticides in small scales areas such as gardens.



Fig. 2.5. Risking practitioner health (Kijewski, 2019).

Conventional methods are not a complete solution for protecting farming fields from pests and diseases. It is obvious that using conventional methods for spraying decreases the efficiency of crop yields. Especially these methods affect agricultural fields by using excessive chemicals and negatively affect soil, plants as well as plant roots. In addition, conventional methods are not proper solutions for precision farming applications. A comparison of conventional and precision farming applications is shown in Table 2.1.

Table 2.1. Precision and conventional farming pros and cons (Katalin, 2011).

Traditional Farming	Precision Farming
Unit of treatment and organization: the field that is regarded as a homogenous arable site	Unit of treatment and organization: arable site that is regarded as different from one point to the other and at “field level” heterogeneous
Nutrient management based on average sample taking	Nutrient management based on GPS and point-like sample taking
Average survey on plant deceases and damage and intervention if necessary	Plant protection treatments based on GPS and point-like sample taking
Sowing with same plant number and variety	Plant species and plant variety-specific sowing
Same machine operation practice	Machine-operation adjusted to the arable site
Unified plant stock in space and time	Unified plant stock organized into homogeneous blocks at arable sites
Few data influencing decision preparation	A lot of data influencing decision preparation

Precision farming aims to combine geo-positioning systems with conventional farming applications (Pecze, 2001). Precision farming applications mainly include

remote sensing and processing of data acquired by remote sensing with the help of geo-positioning systems. With the help of advanced technology and using geo-positioning systems, it is possible to determine the exact location of farming fields and the location of a plant on it. All the same, in conventional farming, without using geo-positioning systems the farming field is the smallest unit for applying an agricultural pest control method. Precision farming differs from conventional farming by applying treatments on the exact locations of a farming field. Using the advanced computer systems and data acquisition via geo-information systems (GIS: Geographic Information System) provide us to evaluate overall status of a farming field. Moreover, it is possible to make economic decisions upon to the acquired data.

With the help of precision farming, it is possible to increase the yield of production and decrease the environmental effects while increasing the quality by lowering the costs. It is a known fact that precision farming is one of the important tools of sustainable farming in recent days (Pecze, 2001).

2.1 Robotics

Recently robotic related technology steps forward in many applications. In the near future, it is foreseen that it will be dominating end-user and industrial applications. This technology is helpful in many ways by providing mobility, enhancing service capability, increasing the efficiency of the products. It has great potential to increase the comfort by transforming lives and work practices (SRAeuRobotics, 2014).

Today robotics is already the key driver of competitiveness and flexibility in large scale manufacturing industries. A relatively low developed, service robots used in non-manufacturing areas such as agriculture, transport, healthcare, security and utilities are expected to become the largest area of global robot sales (SRAeuRobotics, 2014). The robotic industry is seen by some economic forecasters as the next boom industry, similar to the IT boom in 2000. The Japanese government has predicted that the robotics industry will soon expand to become a \$13.2 billion dollar industry. South Korean have committed to nurturing their nation's robot industry as they believe it has the potential to grow into a \$39.4 billion dollar industry (Turner, 2009).

There are many definitions for defining robots such as; "A robot is a reprogrammable, multifunctional manipulator designed to move material, parts,

tools or specialized devices through variable programmed motions for the performance of a variety of tasks” (RIA, 1979). “A robot is an automatic, servo-controlled, freely programmable, multi-purpose manipulator with several degrees of freedom. Variably programmed operations make possible execution of a multiplicity of tasks” (ISO, 1996). A device with degrees of freedom that can be controlled” (JIRA, 1971). By general agreement, a robot is a programmable machine that imitates the actions or appearance of an intelligent creature—usually a human. It is a mechanical or virtual artificial agent, usually an electro-mechanical machine that is guided by a computer program or electronic circuitry. Robots can be autonomous or semi-autonomous and range from humanoids such as Honda's Advanced Step in Innovative Mobility (ASIMO) and TOSY's TOSY Ping Pong Playing Robot (TOPIO) to industrial robots, collectively programmed 'swarm' robots, and even microscopic nanorobots (Fletcher 2014).

To qualify as a robot, a machine must be able to:

- Sensing and perception: it acquires the information from its surroundings,
- Carrying out different tasks: it moves or manipulates the objects by locomotion or manipulating
- Re-programmable: it can be re-programmable to achieve different tasks,
- It functions autonomously and/or interacts with human beings.

A robot is a machine that gathers information about its environment (senses) and uses that information (thinks) to follow instructions to do work (acts) (Tirgul and Naik, 2016).

Robots are especially desirable for certain work functions because, unlike humans, they never get tired; they can endure physical conditions that are uncomfortable or even dangerous for a human being; they can operate in airless conditions; they do not get bored by repetition; and they cannot be distracted from the task at hand (Tirgul and Naik, 2016).

Robots can be classified by type of locomotion such as stationary, wheeled, legged, flying and other robots. On this basis, Unmanned Ground Vehicles (UGV) is a type of wheeled locomotion robots and Unmanned Aerial Vehicles (UAV) included in flying locomotion robots.

2.2 Unmanned Ground Vehicles

An unmanned ground vehicle (UGV) is a vehicle that operates on the ground and without an onboard human operator on it. These unmanned vehicles have sensors to observe the environment and have the ability to make a decision about its movement. There are different techniques for controlling the unmanned ground vehicle such as (Shinde and Chorage, 2016):

- Command control mode: In this mode, it is considered the human decision making and providing navigation commands based on the live video signal received from a camera mounted on UGV,
- Gesture control mode: In this mode, it is considered the hand gesture movement, where UGV controlled using commands sent based on the hand movement mapped by the IMU unit,
- Raptor control mode: In this mode, it is considered the motion tracking system implemented through an image processing system,
- Automatic cruising mode: In this mode, it is considered the UGV has a self-guided locomotion capability using a pre-determined mission as a guide.

2.3 Unmanned Aerial Vehicles

A UAV is commonly known as a drone that flies without a human pilot on its board. It has the capability to fly with the help of inertial sensor and navigation technologies by controlling remotely or autonomously considering pre-determined flight destinations (Limnaios et al., 2012). Mostly the line of flight is remotely monitored by a ground control system (GCS) in order to intervening while an emergency situation has occurred. The “UAV” term consists of fixed and rotary wings UAVs, lighter-than-air UAVs, lethal aerial vehicles, decoys and targets, alternatively piloted aircrafts, and uninhabited combat aerial vehicles (Ma et al. 2013).

The beginning of pilotless flight started with Tesla when he believed an armed, pilotless-aircraft could be used as an aerial defense system for a country in 1915 [19]. The first known step for a powered UAV was A. M. Low's "Aerial Target" of 1916 (US-ARM UAS, 2010). In 1919, Elmer Sperry who is the creator of gyroscope and autopilot technology used a pilotless aircraft to sink a battleship as part of demonstration of gyroscope-guided technology (US-ARM UAS, 2010). The first scale RPV (Remote Piloted Vehicle) was implemented by the model airplane

enthusiast Reginald Denny in 1935 (SAHAM, METU, 2013). In 1964, US initiated their highly classified UAVs into their first combat missions. (NAT-GEO, 2013).

In February 2013, it was reported that UAVs were used more than 50 countries, several of them have their own UAVs such as Iran, China and Turkey. Only the U.S. has procured more than 11,000 drones for military applications. Aviation firms, research universities and researchers of governments, are rushing for designing next-generation aircraft, ranging in size from robotic moths and hummingbirds to Boeing's Phantom Eye (NAT-GEO, 2013).



Fig. 2.6. UAVs (a) Hummingbird, (b) Phantom Eye .

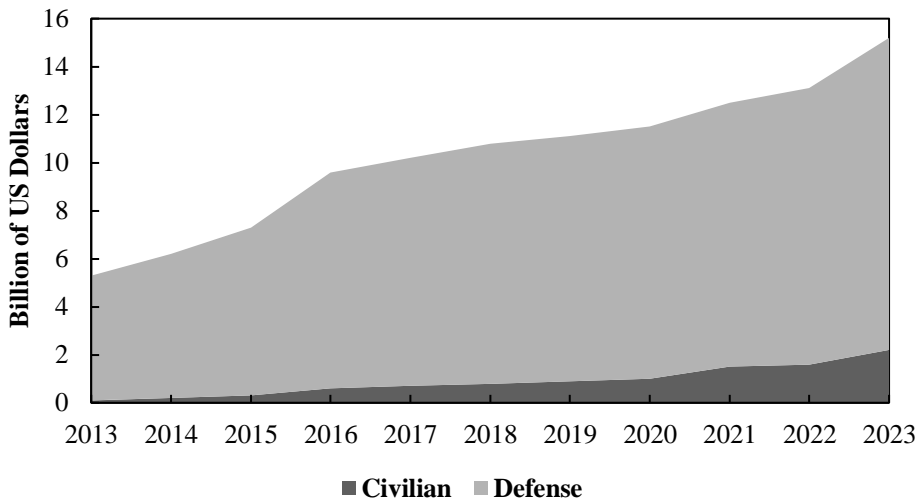


Fig. 2.7. Estimated annual sales of Unmanned Aircraft Systems (Teal Group, 2017).

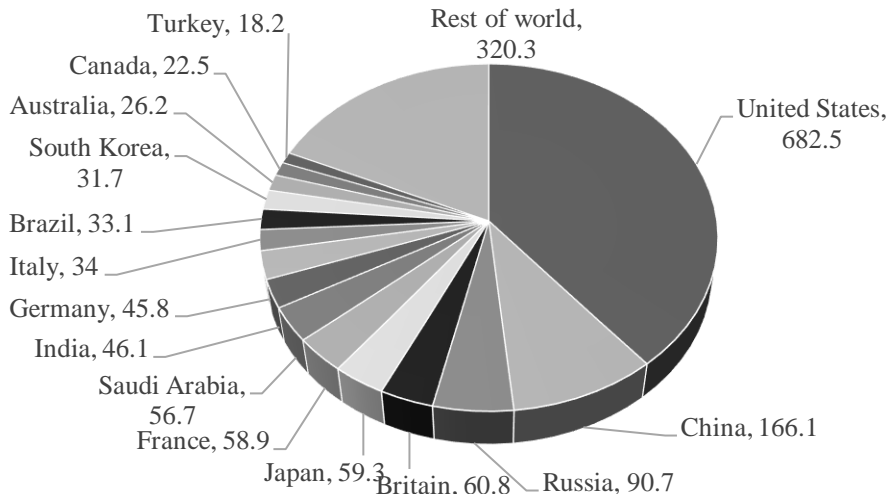


Fig. 2.8. Worldwide spending (\$bn) for UAVs (SIPRI, 2016).

Recently, the well-known international organizations – such as EUROCONTROL, the European Aviation Safety Agency (EASA) and the Federal Aviation Administration (FAA) adopted unmanned aircraft system (UAS) as the correct official term. The changes in the acronym are caused by the following aspects:

For UAS the term “unmanned” refers to the flying without a pilot on-board. The term “aircraft” indicates that it is a kind of aircrafts and has the ability to airworthiness. The term “system” means that it is not just a flying vehicle but a system including a GCS, communication units and take-off and landing systems. A typical UAS comprises system elements in three major segments.

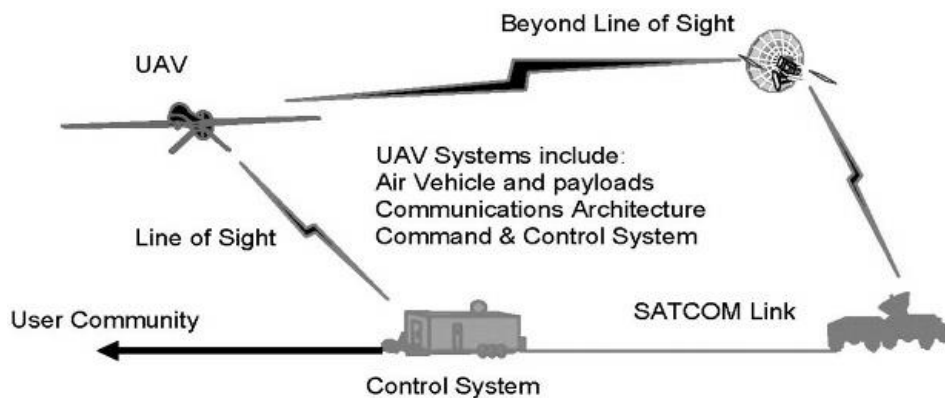


Fig. 2.9. Sense and Avoid in UAS Research and Applications, (Limnaios et al., 2012).

There are six significant types of UAS platforms classified by considering the flying altitude and endurance limits. These UAS types are;

- **MAV** (Micro or Nano Air Vehicles)
- **VTOL** (Vertical Take-Off & Landing)
- **LASE** (Low Altitude, Short-Endurance)
- **LALE** (Low Altitude, Long Endurance)
- **MALE** (Medium Altitude, Long Endurance)
- **HALE** (High Altitude, Long Endurance)

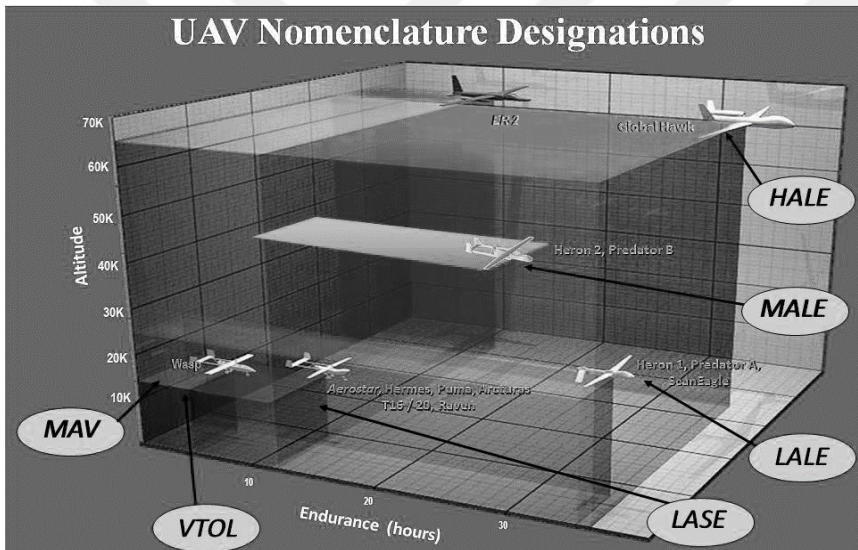


Fig. 2.10. UAV Nomenclature Designation (U.S. Department of Defense, 2013).

This study focuses on VTOL UAV that is a part of VTOL UAS. The VTOL aircrafts are typically chosen when limitations of terrain because they require no take-off, launcher or specialized landing place. These types of aircrafts operate at varying altitudes related to their missions, but commonly used to fly at low altitudes. High power consumption for hovering vertically and flight decreases the flight duration of a VTOL UAV. However, the largest sizes of VTOL UAVs where increased lifting capabilities comply with more flight duration. Fig. 2.10. shows two well-known examples VTOL type UAS named Draganflyer X6 and Yamaha RMAX (Fig. 2.11).

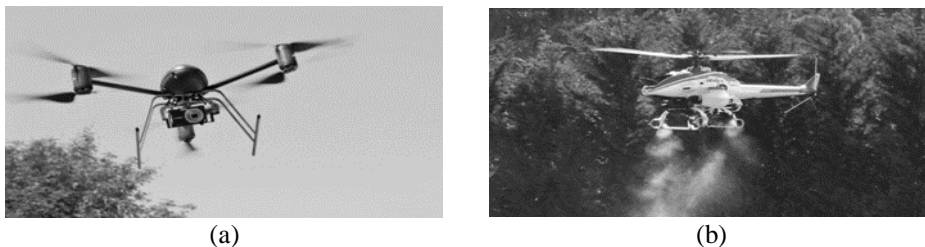


Fig. 2.11. VTOL UAS (a) Draganflyer X6 VTOL UAS,
(b) Yamaha RMAX VTOL aircraft.

LASE (Low Altitude, Short-Endurance) systems, also known as sUAS, small unmanned aircraft systems, also obviate the need for runways with aircraft optimized for easy field deployment/recovery and transport. The aircraft component of these systems typically weighs between 2–5 kg, with wingspans <3 m to enable launching from miniature catapult systems, or by hand. Compromises between weight and capability tend to reduce endurance and communication ranges to 1–2 h and within a few km of ground stations.

LALE (Low Altitude, Long Endurance) Typically at the upper end of the “sUAS” weight designation by the United States Federal Aviation Administration (FAA), these UAS may carry payloads of several kgs at altitudes of a few thousand meters for extended periods.

MALE (Medium Altitude, Long Endurance) aircraft are typically much larger than low-altitude classes of UAVs, operating at altitudes up to 9,000 m on flights hundreds of km from their ground stations lasting many hours.

HALE (High Altitude, Long Endurance) are the largest and most complex of the UAS, with aircraft larger than many general-aviation manned aircraft. These UAVs may fly at altitudes of 20,000 m or more on missions that extend thousands of km. Some HALE aircraft have flight durations over 30 h, and have set records for altitude and flight duration (Watts et al., 2012).

There is also another classification of UAVs by range and altitude based on as shown in Fig. 2.12.

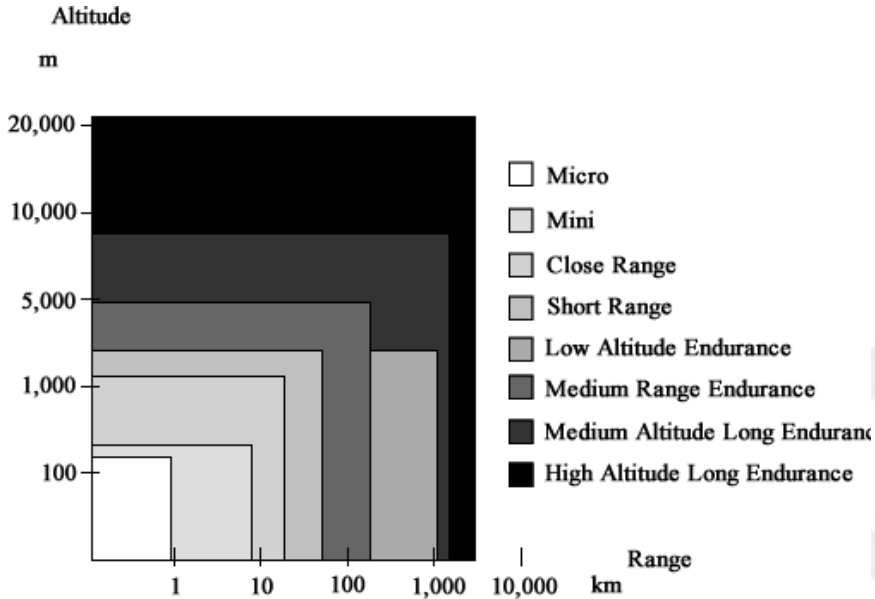


Fig. 2.12. Classification of UAVs by range and altitude based (Eisenbei 2009).

Table 2.2. Comparison of Small Unmanned Aerial Systems (Stark, Smith, and Chen 2013).

UAS	Type	Endurance (min)	Modes	Max Payload (g)
Hummingbird (Ascending Technologies GmbH, 2013)	Multi-Rotor	12	A+M	200
SkyJib (Droidworx, 2012)	Multi-Rotor	-	M	5000
CropCam (CropCam, 2012)	Fixed-Wing	55	A+M	145
Hex Flyer Pro (Prioria Robotics, Inc., 2013)	Fixed-Wing	12	A+M	-
Qball-X4 (Quanser, 2012)	Multi-Rotor	15	A+M	400
Spectra AP (RP Flight Systems, 2008)	Fixed-Wing	45	-	1800
eBee (senseFly, 2013)	Fixed-Wing	45	A	-
CoaX Board (Skybotix, 2010)	Multi-Rotor	-	A+M	60
Gatewing UX5 (Trimble, 2013)	Fixed-Wing	50	A	269
Penguin C UAS (UAV Factory, 2013)	Fixed-Wing	1200	A+M	-
Penguin B UAV (UAV Factory, 2013)	Fixed-Wing	1200	A+M	10000

Penguin BE UAV (UAV Factory, 2013)	Fixed-Wing	110	A+M	6600
Wolverine III (Viking Aerospace, LLC, 2012)	Helicopter	45	A+M	6800
YAK-5 (Viking Aerospace, LLC, 2012)	Fixed-Wing	40	A+M	4000g
R-Max Unmanned Helicopter(Yamaha M. Co., 2002)	Helicopter	150	A+M	28000
Pteryx(Trigger Composites, 2013)	Fixed-Wing	120	A+M	1000
MK Hexa-XL (HiSystems GmbH, 2013)	Multi-Rotor	13	A+M	1500

Many applications can be done by UAVs, such as military, agriculture, surveillance. UAVs also have wide range of applications in civilian scenarios (Azfar and Hazry, 2013). UAVs can accomplish various monitoring missions using vision sensors, including remote sensing, traffic monitoring, forest protection, reconnaissance, remote mapping, search and rescue (Chung-Cheng Chiu et al. 2011).

2.4 Remote Sensing Technology

Remote sensing is the science of obtaining information about objects or areas from a distance, typically from aircraft, satellite or radars (NOAA, 2013). It is the process of gathering data about an object without directly touching it with the sensor. It acquires data by gathering its inputs using electromagnetic radiation or sound waves which is reflected from the targets of interest (Abdulrahman, 2010).

Remote sensors obtain data by detecting the energy that is reflected from Earth (NOAA, 2013) and converts it to information by measuring the electromagnetic radiation that is reflected, emitted and absorbed by objects in various spectral regions of electromagnetic waves as shown in Fig. 2.13. To measure this magnetic radiation, both active and passive sensors are used for remote sensing applications (IEEE, 2012).

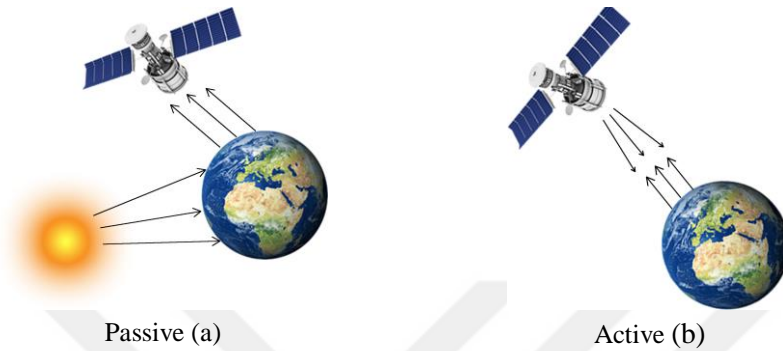


Fig. 2.13. Active (b) and Passive (a) Remote Sensors.

A passive system generally consists of an array of sensors, which records the amount of electromagnetic radiation emitted by the surface. An active system transmits a specific amount of energy to the targeted object and measures the radiation that is reflected or backscattered from that object. (IEEE, 2012).

The beginnings of remote sensing technology are based on photography. The first aerial images of the earth were captured using cameras attached to balloons and kites in the mid-nineteenth century. During World War I, aerial views captured by cameras mounted on airplanes were used for military reconnaissance.

This method of aerial photography became the standard for depicting the earth's surface from a vertical (looking straight down) or oblique (at various angles, generally less than 45°) perspective from that time until the 1960s (IEEE, 2012). Fig 2.14. shows the first photo from space in black-white color.

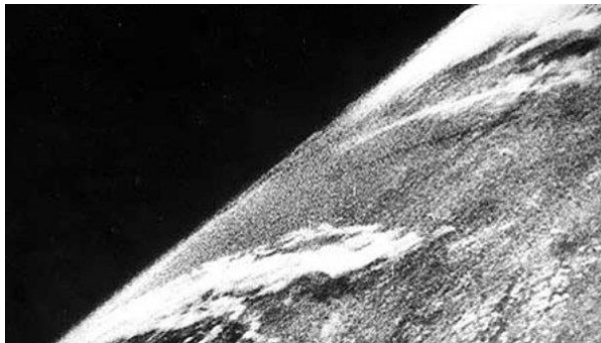


Fig. 2.14. View of Earth from a camera on V-2 #13, launched on October 24, 1946, (Reichhardt, 2006).

Satellites developed by Russian and American space programs expanded the field of vision in the 1960s by obtaining views from beyond Earth's atmosphere. Landsat, Nimbus, ERS, RADARSAT and UARS are satellite programs used for earth observation. Images collected by NASA's Landsat satellite program, first launched in 1972, are used to monitor a number of environmental factors including water quality, glacier recession, sea ice movement, invasive species encroachment, coral reef health, land use change, deforestation rates and population growth. Satellite imagery is also used to assess damage from natural disasters such as fires, floods, and tsunamis, and subsequently, plan disaster relief and flood control programs (IEEE, 2012).

2.4.1 Remote Sensing Platforms

Mostly, Earth Observation (EO) data acquired by using satellites, airborne (multi-hyperspectral), UAV and ground vehicles (Udelhoven, 2012). Satellites provide multispectral imaging with limited return interval that takes days to get new images from satellite for end-user. Airborne vehicles have the capability to obtain images on demand for both multispectral and hyperspectral imaging but the cost of airborne applications is high. UAVs provide panchromatic, multispectral and hyperspectral EO data with low cost and on demand. UAV-based remote sensing studies have been carried out for many decades. In the late 1970's fixed-wing remote-controlled aircrafts have been investigated for first motorized UAV photogrammetry experiments. A quarter-century later the first high-resolution digital elevation models (DEMs) using autonomously controlled helicopter UAVs were generated. Today there are many other UAV-systems like motorized paragliders, quad-rotor systems, blimps, kites and balloons in use (Niethammer et al. 2010).

UAVs combined with remote sensing technology have been aiming to make use of the current technologies in order to acquire the spatial data about land cover, resource, and the environment for processing remote sensing data, modeling, analyzing, including aircraft control, sensor, remote control, communication, Differential Global Positioning System (D-GPS), and remote sensing application (Ma et al. 2013). Because of the high frequency and high resolution from UAVs, using these vehicles as remote sensing platforms offers the unique ability for repeated deployment for the acquisition of high temporal resolution data at very high spatial resolution (Laliberte, 2011).

The accuracy of measurement methods shown in Fig. 2.15 for ground and aerial vehicles, in relation to the object/area size.

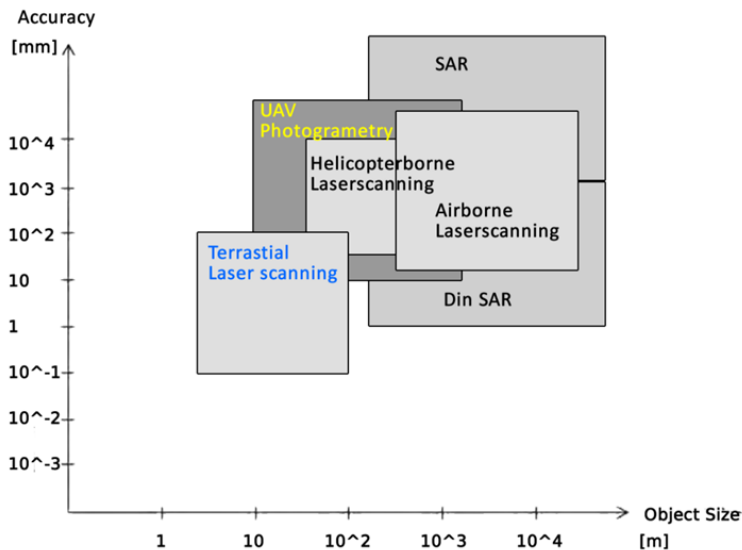


Fig. 2.15. The accuracy of measurement methods in relation to the object/area size (Limnaios et al., 2012).

Compared to manned aircraft systems, major advantages of UAVs are that they can be used in high-risk situations without endangering human life and inaccessible areas, also at low altitudes and at flight profiles close to the objects where manned systems cannot be operated. These regions are, for example, natural disaster sites, e.g. mountainous and volcanic areas, flood plains, earthquake and desert areas, and scenes of accidents. Furthermore, in cloudy and drizzly weather conditions, the data acquisition with UAVs is still possible, when the distance to the object permits flying below the clouds (Ma et al. 2013).

Furthermore, in cloudy and drizzly weather conditions, the data acquisition with UAVs is still possible, when the distance to the object permits flying below the clouds (Ma et al. 2013).

Strength and weaknesses of aerial and ground vehicles indicated in Fig. 2.16.

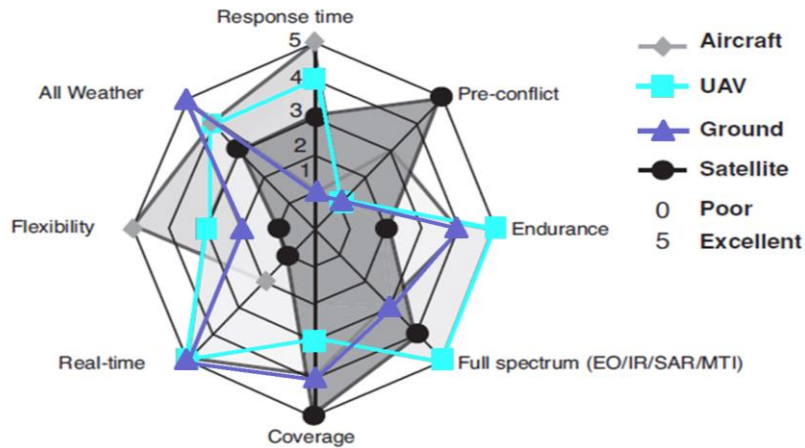


Fig. 2.16. Strengths and Weaknesses of UAVs and UGVs (Limnaios et al., 2012).

In addition, one fundamental advantage of using UAVs is that they are not burdened with the physiological limitations and economic expenses of human pilots. Supplementary advantages are the real-time capability and the ability for fast data acquisition while transmitting the image, video and orientation data in real-time to the ground control station (Limnaios et al., 2012). The pros and cons of the different types of UAVs indicated in Table 2.3 for Remote Sensing Applications. UAVs also used for aerial photography, Normalized Difference Vegetation Index (NDVI), thermal imaging in agricultural fields examples shown in Fig. 2.17. They also used for pest spraying, disease monitoring for precision farming applications.

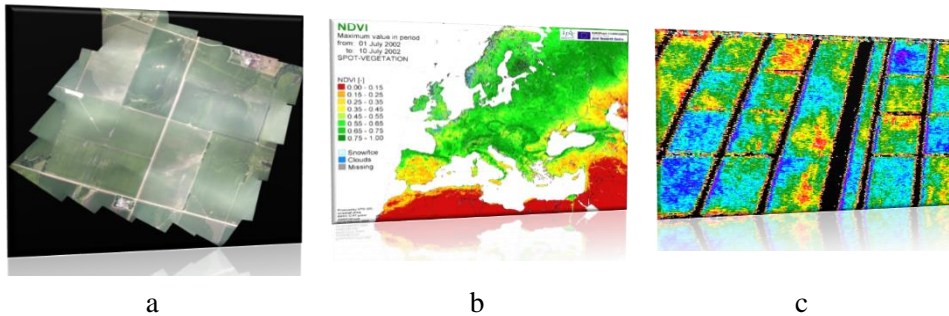


Fig. 2.17. Remote Sensing in farming, visible spectrum imaging (a), satellite-based thermal imaging (b), aircraft based thermal imaging (c).

Table 2.3. Pros and cons of the different type of UAVs (levels: high=2; medium=1; low=0) (Eisenbei 2009).

Type of aircraft	Range	Endurance	Weather and wind dependency	Maneuverability
Balloon	0	2	0	0
Airship	2	2	0	1
Gliders/Kites	1	0	0	0
Fixed wing gliders	2	1	1	1
Propeller & Jet engines	2	2	1	1
Rotor-kite	2	1	0	1
Single rotor	1	1	1	2
Coaxial	1	2	1	2
Multi-copters	1	1	1	2

2.4.2 Plant Disease Detection

Most common commercially available solutions for detecting plant disease use light emitting diodes (LED) and photodiode combined in an electronic circuit (Fig 2.18) but with the lack of plant disease detecting efficiency. The inability of these LED-based plant disease-detecting sensors to discriminate between healthy and diseased plants limits its application in precision farming (Askraba et al. 2016).

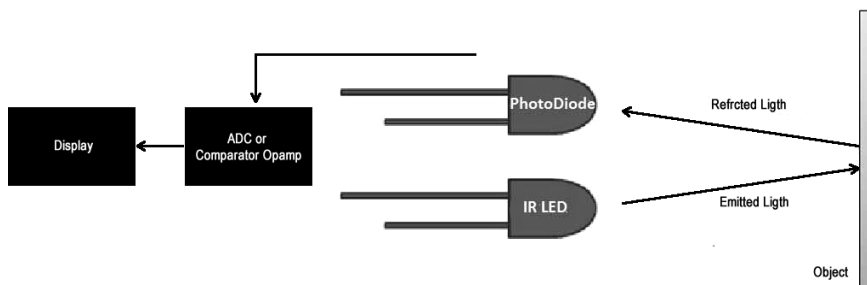


Fig. 2.18. Basic block diagram of commonly used Photodiode sensor.

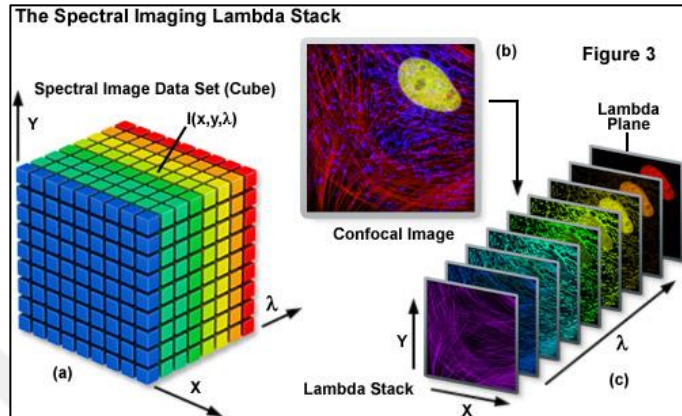


Fig. 2.19. Advanced method output, spectral image data set (a), confocal image (b), lambda stack (c).

Plants show different reflectance in terms of reflected intensity by using more bands respect to this significant difference in the electromagnetic spectrum which allows more accurate plant discrimination. In a study hyperspectral analysis of weeds and crops has been carried out from satellite and aerial platforms. The results are shown in Table 2.4 for classifying 6 predetermined crop species.

Table 2.4. Overall accuracies for classifying 6 crop species.

Bands	Accuracy
3	48%
7	81%
13	87%
22	90%

The overall accuracies increased from 56% to 90% for 3 bands to 22 bands for classifying 6 crop species (Paap et al. 2008). Using more wavelength bands in the electromagnetic spectrum where plants show different optical reflectance in terms of reflected light intensity provides more accurate plant disease discrimination.

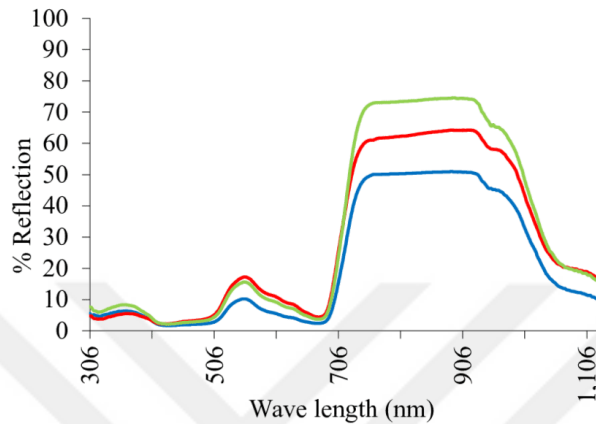


Fig. 2.20. The percentage spectral reflectance of *Austro eupatorium inulifolium* leaves. Each line of different colors represents measurements taken from separate plants. (Piyasinghe et al., (2018).

Multispectral imaging combines two or more spectral imaging bands in a single optical system. The imaging bands has relatively large bandwidth when compared with Hyperspectral imaging. Typically, a multispectral system uses a combination of different bands combined in a single system. These bands are:

- Visible spectrum that consists blue, green and red bands (400 - 760nm),
- Near Infrared (NIR) band (0.7 - 1 μm),
- Short-Wave Infrared (SWIR) band (1 - 1.7 μm),
- Mid-Wave Infrared (MWIR) band (3.5 - 5 μm),
- Long-Wave Infrared (LWIR) band (8 - 12 μm).



Fig. 2.21. A multispectral image from the DMCii satellite.

A multispectral image (Fig. 2.21) from the DMCii satellite to identify fresh vegetation indicated in red color. The image obtained from the orbit using red, green and NIR spectral bands (DMCii, 2011; Eichenholz et al., 2010).

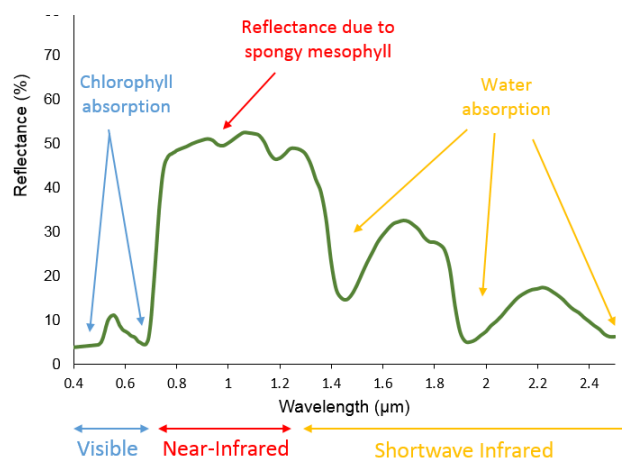


Fig. 2.22. Typical reflectance spectra of plants.

Plant reflectance of the wavelengths in one channel are mean values (Fig. 2.22). It is possible to use these mean values in different bands of the electromagnetic

spectrum for discriminating the plants from soil and water as shown in Fig. 2.23 the reflectance of water, soil and vegetation in different wavelengths.

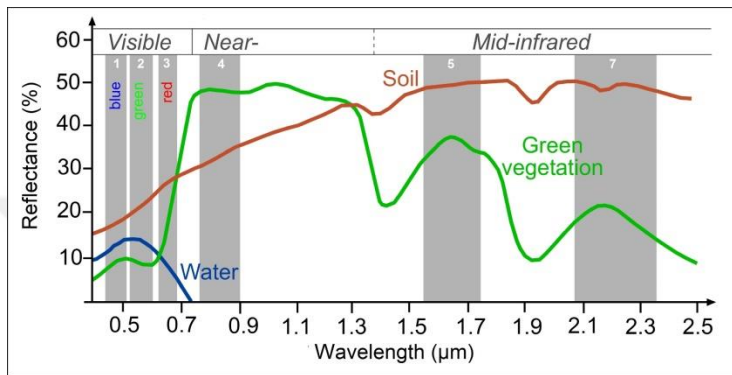


Fig. 2.23. Reflectance spectra of water, soil and vegetation in different wavelengths (SEOS, 2017).

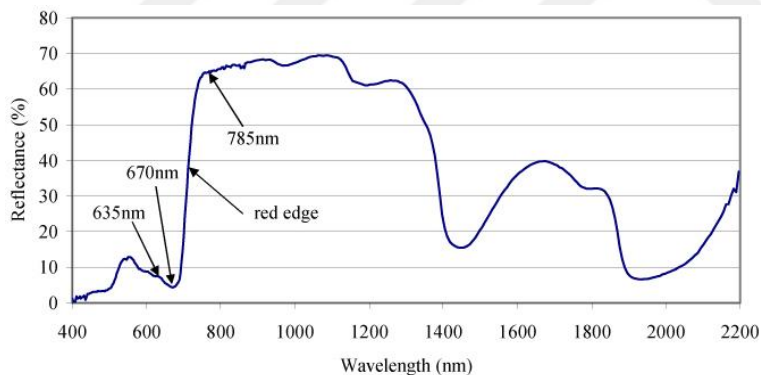


Fig. 2.24. The reflectance of typical green vegetation in different wavelengths (SEOS, 2017).

NDVI and PRI are commonly used methods and results calculated from measurements of electromagnetic radiation reflected from canopy surfaces. They are correlated with canopy variables such as:

- light use efficiency (LUE),
- biomass and crop yield,
- crop and forest phenology,
- canopy growth,
- photosynthetic performance/ CO_2 Uptake.

Normalized Difference Vegetation Index (NDVI) bands are centered at 650 nm (Fig. 2.24) and 810 nm with 50 nm and 40 nm Full Width Half Maximum (FWHM), respectively. Photochemical Reflectance Index (PRI) bands are centered at 532 nm and 570 nm with 10 nm FWHM.

PRI devices measure the Photochemical Reflectance Index in two narrow wavelength bands centered close to 531 nm and 570 nm. PRI is sensitive to changes in carotenoid pigments that are indicative of photosynthetic light use efficiency, the rate of carbon dioxide uptake, or as a reliable water-stress index. As such, it is used in studies of vegetation productivity and stress.

NDVI devices compare reflected light at two distinct wavelengths, 660 and 740 nm. The pigment in plant leaves - chlorophyll - strongly absorbs visible light (from 0.4 to 0.7 μm) for use in photosynthesis. The cell structure of leaves, on the other hand, strongly reflects near-infrared light (from 0.7 to 1.1 μm) as indicated in Fig. 2.24. The differences in plant reflectance in the visible and near-infrared wavelengths are used to calculate the NDVI index. NDVI is directly related to the photosynthetic capacity and hence energy absorption of plant canopies (PSI PlantPen, 2017).

2.4.3 Normalized Difference Vegetation Index

The formula of the NDVI method can be used to discriminate the green level of plants. It is indicated in Eqn. 2.1. Calculations of NDVI for a given pixel always result in a number that ranges from minus one (-1) to plus one (+1); however, no green leaves give a value close to zero. A zero means no vegetation and closes to +1 (0.8 - 0.9) indicates the highest possible density of green leaves.

$$NDVI = \frac{NIR - VIS}{NIR + VIS} \quad (2.1)$$

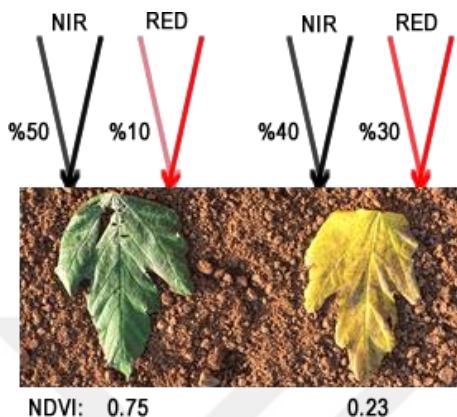


Fig. 2.25. NDVI calculation example.

In general, the variations in the reflectance between 550nm and 800nm can be used to discriminate between different plants and weeds (Paap et al., 2008). There are also many various indices using different bands in the electromagnetic spectrum for vegetation and a few of them are shown in Table 2.5.

Table 2.5. Different wavelengths used for measuring NDVI.

Vegetation Index	Abbreviation	Equation (nm)	Reference
Normalized Difference Vegetation Index	NDVI	$\frac{NIR - RED}{NIR + RED}$	Aparicio et al., (2004)
Renormalized Difference Vegetation Index	RDVI	$\frac{800n - 670nm}{\sqrt{800n + 670nm}}$	Glenn et al. (2010)
Simple Ratio	SR	$\frac{NIR}{RED}$	Ahamed et al. (2011)
Green-Blue NDVI	GBNDVI	$\frac{NIR - (GREEN + BLUE)}{NIR + (GREEN + BLUE)}$	Wang et al. (2007)
Infrared Percentage Vegetation Index	IPVI	$\frac{NIR}{NIR + RED} (NDVI + 1)$	Kooistra et al. (2003)
Blue-Normalized Difference Vegetation Index	BNDVI	$\frac{MIR - NIR}{MIR + NIR}$	Xie et al. (2007)
Enhanced Vegetation Index	EVI	$\frac{2.6(NIR - RED)}{(NIR + 6RED + 7.5BLUE)}$	Nagler et al. (2007)

3. MATERIAL AND METHOD

In general, precision farming aims to increase the benefit-cost ratio by reducing the inputs and increasing the outputs. In line with this direction, it is important to decrease the usage of chemicals in pesticide spraying applications. This thesis study focused on decreasing the usage of pesticides by spraying only predetermined target locations. For this purpose, a multispectral camera is designed, developed, and integrated with a GPS module and an RF transceiver. It is a plant disease detecting and locating unit, which was used for specifying target plants in a farming field. A ground vehicle is designed and developed in order to locate the target point while the vehicle scanning the field via the multispectral camera and GIS module. An aerial sprayer designed and developed for spraying the predetermined locations in the farming field.

The relationship between these units was shown in Fig. 3.1. The spraying process has three main stages: In the first stage, a ground vehicle scans (green path on Fig. 3.1) a desired farming field for collecting field data and transfers it to a base station. In order to minimize elapsed time and the usage of pesticides at the second stage, the base station evaluates the obtained field data and determines target locations for spraying. In the last stage, an aerial sprayer sprays the predetermined target locations with the help of GIS (yellow path on Fig. 3.1).

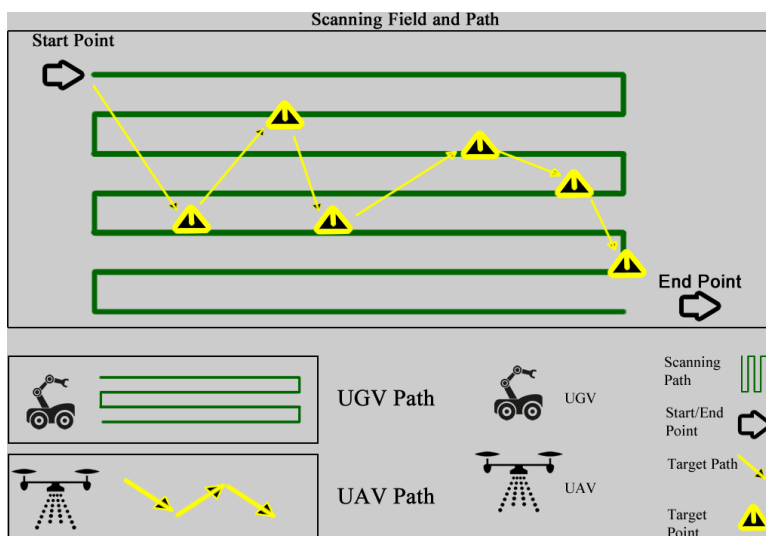


Fig. 3.1. Plant disease detecting and pesticide spraying steps.

This thesis study has three main sections (Fig. 3.2) similar to a closed-loop controlled robotic application. It aims to achieve precise spraying difficulties in pesticide spraying applications for plant protection. In line with this purpose, three main units are used as a loop in order to accomplish the sensing, planning, and acting tasks.

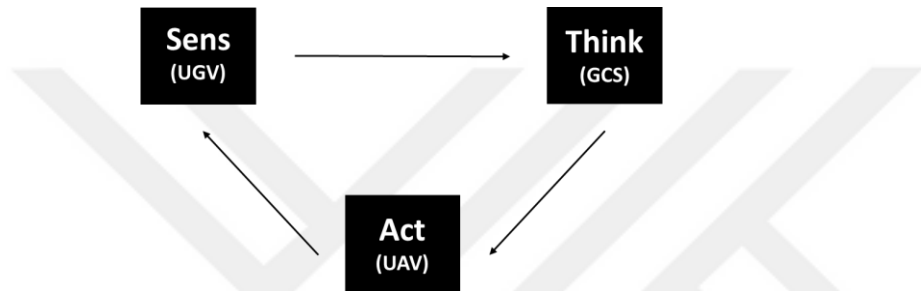


Fig. 3.2. The relationship between major units.

The sensing mechanism consists of a custom-designed UGV and the Multispectral camera that mounted on it for obtaining the health status of a desired plant. Planning is the second mechanism named GCS that accomplishes coordination between sensing and acting mechanisms using a computer. The acting mechanism is composed from the UAV and a spraying unit to accomplish aerial spraying missions. All units involve wireless communication modules to provide communication between the main units. The relationship between these units and subunits are indicated in Fig. 3.3.

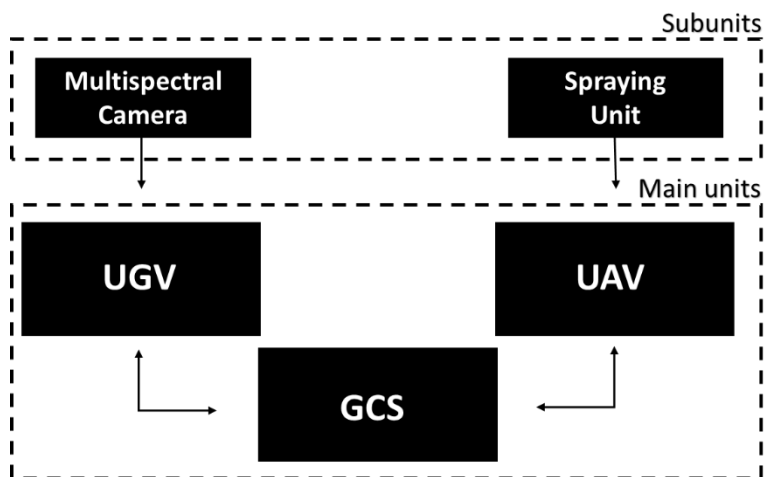


Fig. 3.3. The relationship between control loop mechanisms.

3.1 Ground Control Station

The GCS functions as a coordinator between sensing and acting mechanisms by using a personal computer (PC) and an RF transceiver. This station coordinates the mechanisms to achieve spraying difficulties such as reducing the costs, decreasing elapsed time and minimizing the harmful effects of the chemicals for providing ideal spraying. The main processes of these units summarized in three steps:

- get raw data from the sensing unit,
- process the data for finding disease and determines spraying locations,
- transfer target locations to the acting mechanism for initiating the spraying application.

An explanation of the plant disease-detecting steps and spraying processes are shown as a flow chart in Fig. 3.5.

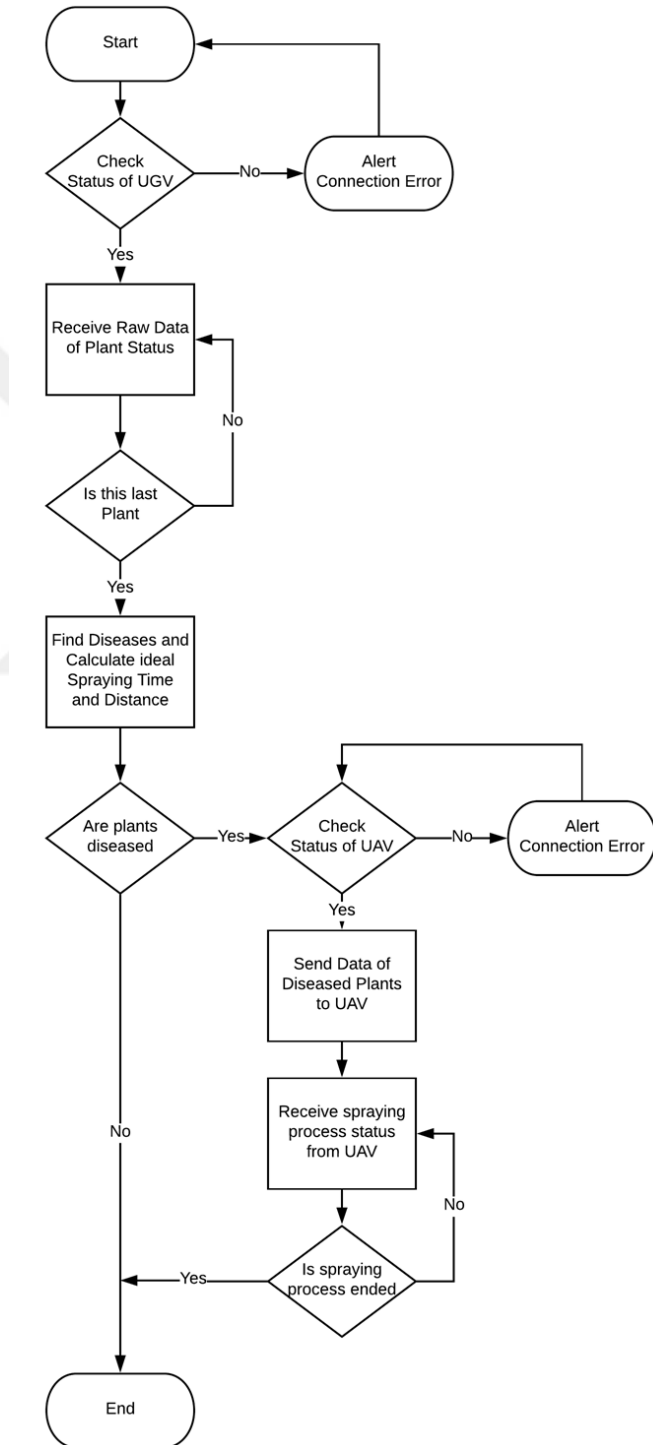


Fig. 3.5. Flowchart of the plant protection loop.

External communication between the major units is achieved by using Radio Frequency (RF) transceivers with a multiple access method for providing simultaneous communication and the multiple access methods is a proper way for communication when there are more than two units available (Frenzel and Louis 2008).



Fig. 3.6. Wireless communication between major units.

In this study the communication between main units is achieved by using Frequency Division Multiple Access (FDMA) and Time-Division Multiple Access (TDMA) multiple access methods to provide a robust communication solution. TDMA method is used for remote monitoring of the subunits statuses. FDMA method is chosen for remote control because it does not requires synchronization, divided frequencies provides simultaneous communications and each divided frequency band is allocated to a different device so it provides continuous data transmission.

In order to implement the plant disease locating process a multispectral camera (Fig. 3.8) integrated with a GPS module and an RF transceiver and its block diagram is shown in Fig 3.7. Block diagrams of the disease-locating units are shown in Fig. 3.8.

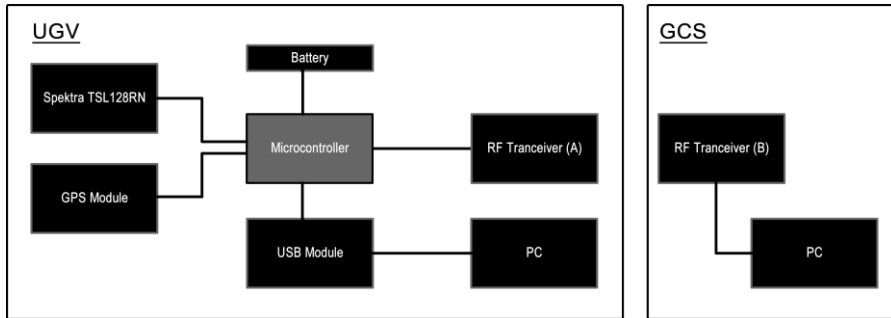


Fig. 3.7. Remote sensing system block diagram

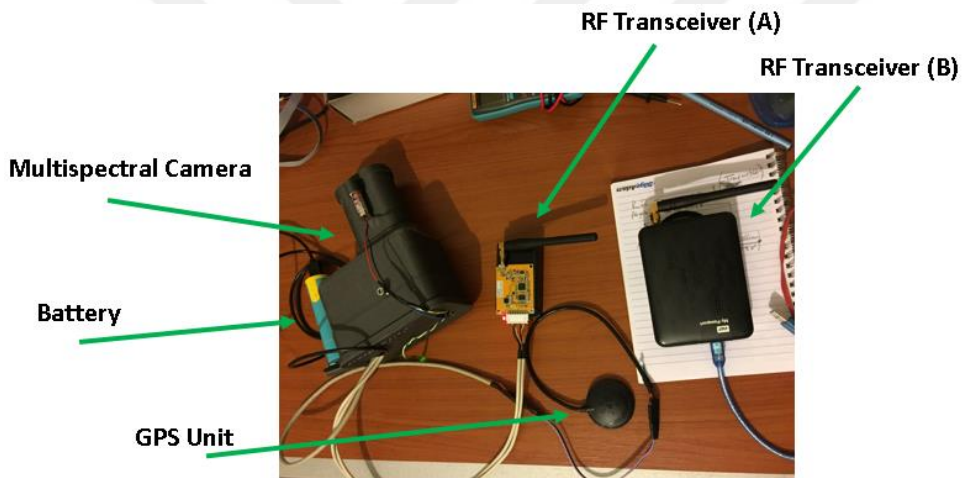


Fig. 3.8. Plant disease-locating unit and GCS receiver.

A custom-designed two-band spectral camera is used as a plant disease detection device that vertically mounted (Fig. 3.8) on the UGV to investigate the surface of the targeted area. The sensing device is suitable to use in daylight between 09:00, 16:00 hours. In addition, other details of this sensing unit are explained in the plant disease detecting chapter.

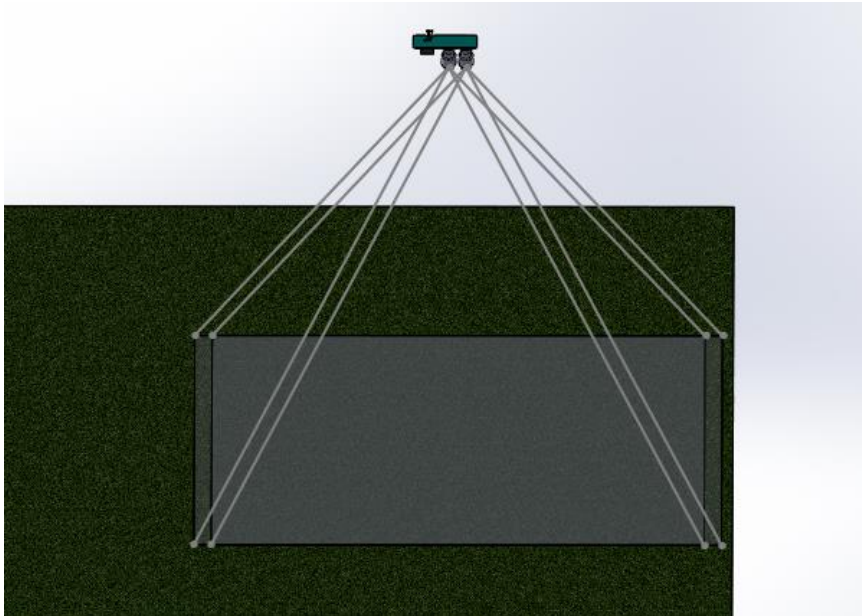


Fig. 3.9. Scanning the target field for plant disease detection.

The UGV is a remotely controlled (RC) vehicle that has the ability to acquire and send the status of plants to the GCS. While it is moving in the field, it continuously sends raw data of the status of the plants. This raw data includes row number, time duration, latitude, longitude, altitude, NDVI value. An example of data transferred between UGV and GCS is shown in Table 3.1.

Table 3.1. Raw Data acquired by UGV.

Row ID	GPS DATA	\$GNRMC	UTC of position				
			Position status (A = data valid, V = data invalid)				
			Latitude (DDmm.mm)				
			Latitude direction: (N = North, S = South)				
			Longitude (DDDmm.mm)				
			Longitude direction: (E = East, W = West)				
			Speed over ground, knots				
			Track made good, degrees True				
			Date: dd/mm/yy				
RED DATA	Px 1	Px 2	Px 3	Px 4	Px 5	Px 6	Px 7
NIR DATA	Px 1	Px 2	Px 3	Px 4	Px 5	Px 6	Px 7

In order to initialize the spraying mission ideal flight duration is formulated in order to reduce flying time and for increasing the spraying capability of the sprayer UAV.

$$Mission \begin{cases} start & ideal\ flight\ duration \geq \left(2 \times \left(\frac{\sum_{i=1}^n di}{V_s} + d_T \cdot C_p \right) \times SF \right) \\ idle & ideal\ flight\ duration < \left(2 \times \left(\frac{\sum_{i=1}^n di}{V_s} + d_T \cdot C_p \right) \times SF \right) \end{cases}$$

where, d: distance between two check points (target spraying point (m)), Vs: Vehicle Speed, dT: spraying delay time (s), Cp: check point count, SF: Safety Factor (0.8).

3.2 Unmanned Ground Vehicle

In order to develop a low cost UGV which is proper for terrain applications, many parameters should be considered such as payload capacity, cruising duration, slope of the terrain, rolling friction. For this study, it is aimed to design and develop a UGV which is suitable for loose sand conditions with 10° angle for low speed applications. The 3D model of the designed vehicle is shown in Fig. 3.10.

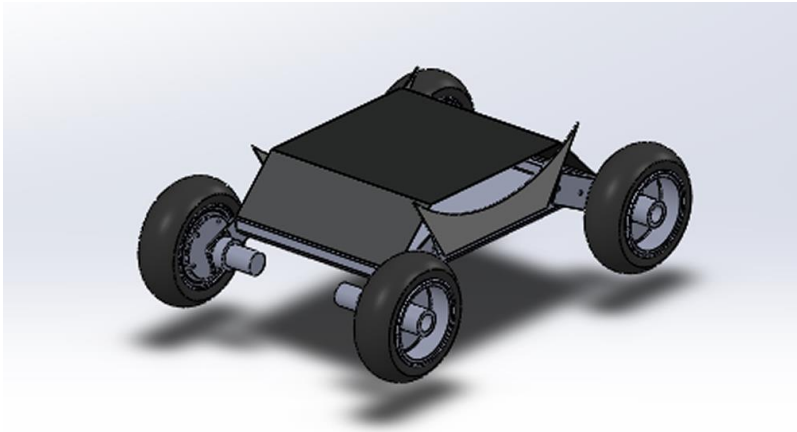


Fig. 3.10. 3D model of the designed UGV.

For a ground vehicle, it is possible to use Newton's second law to calculate a required driving force for a known mass and acceleration. The slope of the desired terrain, rolling friction coefficient and air dragging force should be considered in order to determine this driving force. Using the sum of these force equations (Eqn. 3.1) results it is possible determine maximum torque and power requirements for desired conditions (Meriam and Kraige, 2001).

$$F_{Total} = F_{accel} + F_{slope} + F_{roll} + F_{air} \quad (3.1)$$

where:

$$F_{accel} = m \cdot a \quad (3.2)$$

where: m: mass (kg), acceleration (m/s²).

$$F_{slope} = s m g \quad (3.3)$$

where: s: upward slope, m: mass, g: gravitational force.

$$F_{roll} = cr \cdot m \cdot g \quad (3.4)$$

where: cr : rolling friction coefficient, m: mass, g: gravitational force.

$$F_{air} = \rho \cdot cd \cdot A \cdot \frac{v_{wind}^2}{2} \quad (3.5)$$

where: ρ : density of air (kg/m³), cd : coefficient of air resistance, A : frontal area in (m²), v_{wind} : wind velocity (m/s).

$$P = T \times \omega \quad (3.6)$$

where: P: Power (W), T: Torque (Nm), ω : angular velocity.

3.2.1 Specifications of the UGV

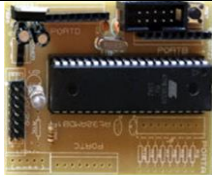
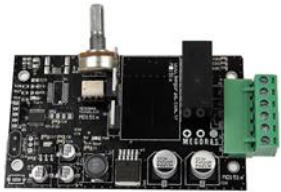
Specific parameters and main properties of the developed UGV are listed in Table 3.2.

Table 3.2. Specifications of the UGV.

Max. Payload:	5 kg
Max. Speed:	1.76 m/s (6.46 km/h)
Max. Slope:	10 °
Drive Power:	4 x 4 wheels (80W DC Electric Motors)
Steering Method:	Four Wheel Skid Steering
Motor driving method:	PWM
Cruise Duration:	60 min
Weight:	25 kg
Material:	Al 6068, Al 6068, Al 1010, Steel ST37 (profile tubes and sheet)
Dimension:	567 x 385 x 230 (mm)

The main components for the UGV are listed in Table 3.3.

Table 3.3. Components of the UGV.

Product	Specifications	Description & Images
Microcontroller	Atmega32A 8 Bit 32 I/O 16 MHz Timer	
BDC Motor	60mm Gear DC Motor 12-24V 200Rpm Stall Torque: 30kg/cm	
BDC Motor Driver	MD151A BDC Motor Driver Voltage: 9-40V Max load: 12V/20A or 24V/10A Bidirectional PWM driving.	

Battery	Li-Po 1800mAh 14.8V 65C	
---------	----------------------------------	--

3.2.2 The Chassis and Sensor Holder

The UGV has Brushed Direct Current (BDC) motors that are driven by Direct Current (DC) motor drivers for providing proportional forward and backward locomotion. In order to increase maneuverability in difficult terrains the skid steering method is used to steer of the UGV. Pulse Width Modulation (PWM) method is used for driving motor at desired speed. Lithium polymer (Li-Po) batteries are used because of their lightweight structure. A battery level indicator sensor is used to monitor remaining battery level and an electronic development board is used as movement control unit for directing the vehicle. For positioning of the UGV, an electronic compass and a Global Positioning System (GPS) module is mounted on it. An assembled image of the UGV is shown in Fig. 3.11.

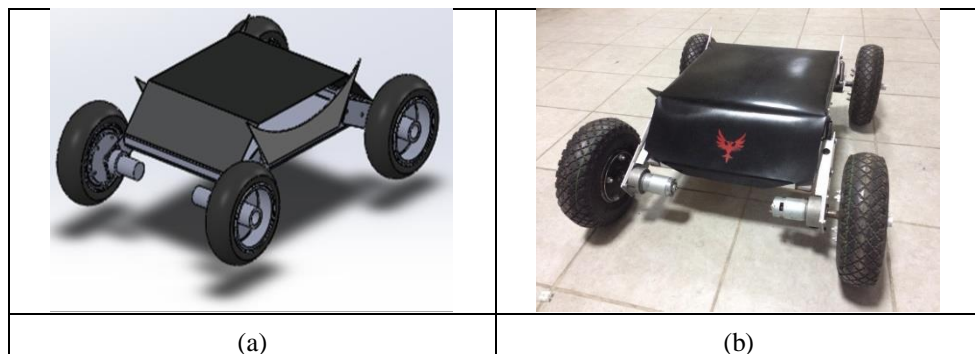


Fig. 3.11. 3D Model (a) and assembly (b) of the UGV.

A multispectral camera is mounted on this vehicle (Fig 3.14) and integrated with the UGV, which is integrated with a Microcontroller Unit (MCU) used for determining diseased plants. A dedicated MCU and an RF transceiver module is used for communication between UGV and GCS in order to establish the plant disease-detecting goal via an RF signals. The relationship among these units indicated as a block diagram in Fig. 3.12.

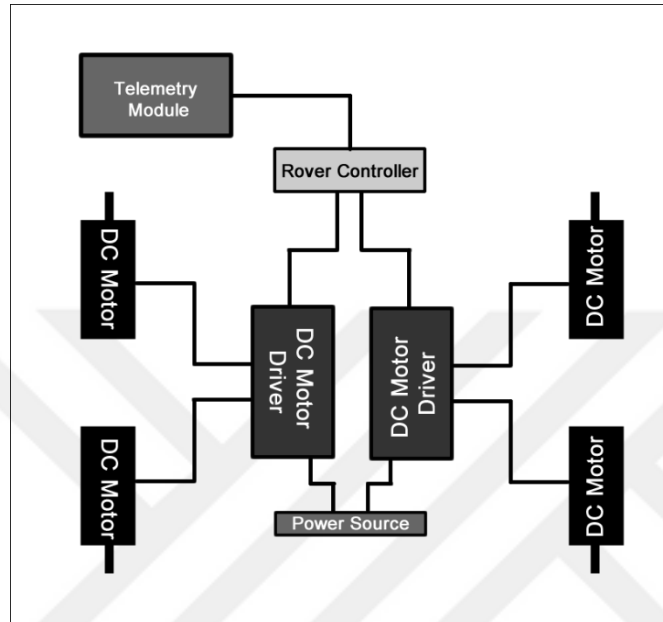


Fig. 3.12. Block diagram of the UGV.

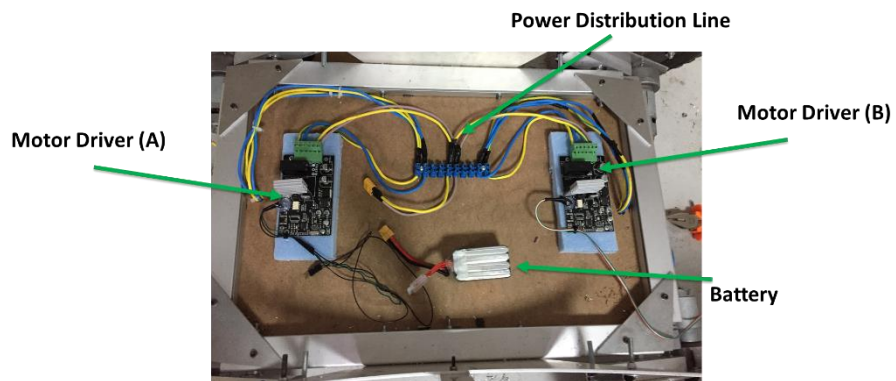


Fig. 3.13. The layout of motor drivers and wiring.

In order to minimize vibrations and damping the forces on Multispectral camera a Gimbal is used at the tip of the sensor holder, which mounted the UGV (Fig. 3.14).



Fig. 3.14. The UGV with the sensor holder.

3.2.3 FEM Analysis

Structural analysis is implemented for the chassis using SolidWorks simulation software. Hubs of the UGV are fixed as indicated in Fig. 3.15. and 400N force that includes the weight of the chassis and a 5 kg payload is applied in the vertical axis on the aluminum frame that used as the main holder part for the chassis of the UGV.

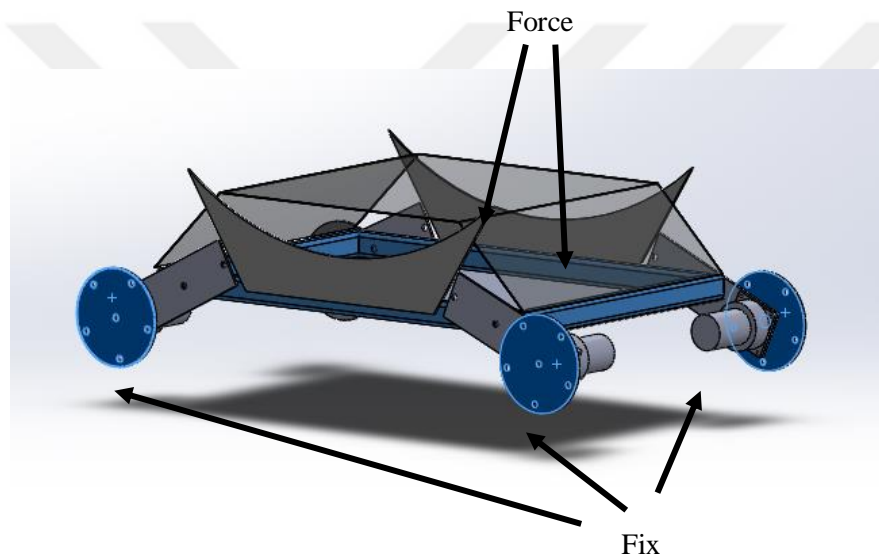


Fig. 3.15. Chassis FEM.

The flanged coupler static structural analysis is implemented using SolidWorks simulation software. The wheel connection points of the hub are fixed and a torque applied (Fig. 3.16) on the shaft hole of the flanged coupler in the direction of the motor rotation.

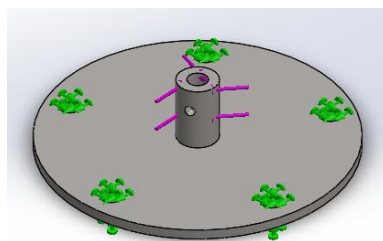


Fig. 3.16. Flanged coupler FEM.

3.3 Multispectral Camera for Plant Disease Detection

NDVI and PRI are both well-known methods in farming applications. These methods are used to calculate vegetation indices by the help of electromagnetic radiation that is backscattered from the surface of a targeted object. In general, plant disease detection devices use two wavelengths, i.e. the red and near-infrared bands for determining vegetation indices. The other solution is Photochemical Reflectance Index (PRI) measures two wavelength bands centered close to 531 nm and 570 nm that uses bands in the visible range.

In daylight a healthy plant reflects only 10% of the green color band and it is less for red and blue bands because of chlorophyll absorbance. However, above the red edge these plants reflect NIR wavelengths close to 50%. In this study, a very common measurement method named NDVI is to determine the density of green on farming fields instead of using image-processing methods in the visible spectrum. An NDVI device compares reflected light at two distinct wavelengths, close to 660 nm (Dark Red) and above 740 nm (Red Edge) (PlantPen 300, 2017). Farming fields are commonly investigated using these spectral bands in the visible red (Red) and near-infrared (NIR) bands (Rabatel et al., 2011). The most well-known plant reflectance indices are the Simple Ratio (SR) of NIR to Red reflectance and the normalized form of those two bands, named the Normalized Difference Vegetation Index (NDVI). The formulation of SR and NDVI are indicated in Eqn. (3.7) and (3.8).

$$SR = NIR/Red \quad (3.7)$$

where: SR: Simple Ratio, NIR: Near-infrared band and Red: Red band.

$$NDVI = \frac{NIR - Red}{(NIR + Red)} \quad (3.8)$$

where: NDVI: Normalized Difference Vegetation Index, NIR: Near-infrared band and Red: Red band.

Today, in farming applications, in order to detect diseases on plants, image processing and signal processing techniques are widely used. Image Processing is an advanced solution to detect a diseased plant in a farming field. For this purpose, there are many software and libraries for computer vision and machine learning. Open Source Computer Vision Library (OpenCV) is a good example for image processing applications (Bradski and Kaehler 2008). It is suitable for advanced robotic applications and supports C++, which is a general-purpose programming language (Stroustrup 1989). It includes many functions such as finding contours, calculating the area, determining the distance between two points and image filters to resolve an image swiftly (Fig. 3.17). However, these libraries need advanced hardware requirements and high capacity power sources with a lack of portability cause of the volume and weight of necessary hardware.

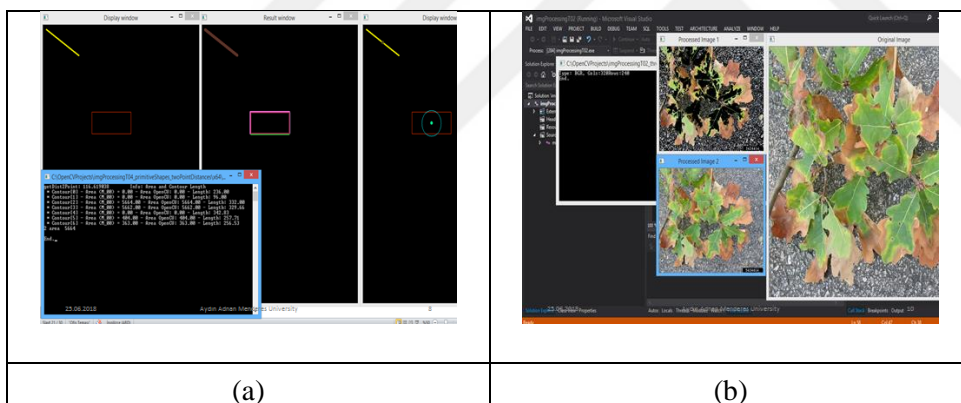


Fig. 3.17. OpenCV Image processing examples, primitive shape distance detecting (a), original image for plant disease detecting (b).

This study aims to detect diseases in crop yields for that reason the plant disease detection method used in this study should be suitable for outdoor applications. The proper solution for this kind of application is minimizing the inputs. An encoded image such as JPEG, GIF, PNG has too many digital numbers stored in it. A bitmap with three channels consists of 24-bit data for every pixel of an image. In addition, these pixels are consisting of 8 bits of RGB color for each channel (Liesch 1994). An example 320x240 image and partial bitmap of the image shown in Fig. 3.18.

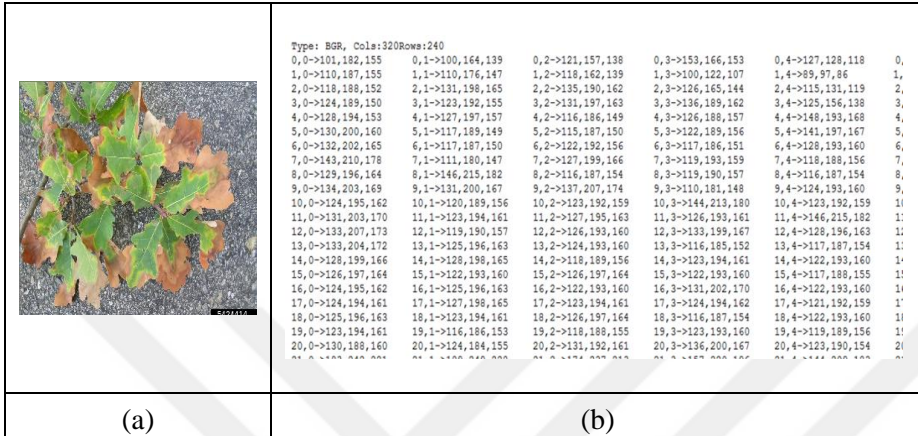


Fig. 3.18. The bitmap of a 24 Bit 320x240 pixel RGB Image

3.3.1 Spectral Imaging

There is another way to solve the plant disease-detecting problem, which uses electromagnetic spectrum that is not in the visible range. It is an alternative way to detect the healthiness of plants. A healthy plant absorbs nearly all visible bands of the electromagnetic spectrum except it reflects about 10% of the green band because of chlorophyll absorption as shown in Fig. 3.19. This specific property of the plants is commonly used to differentiate between diseased and healthy plants.

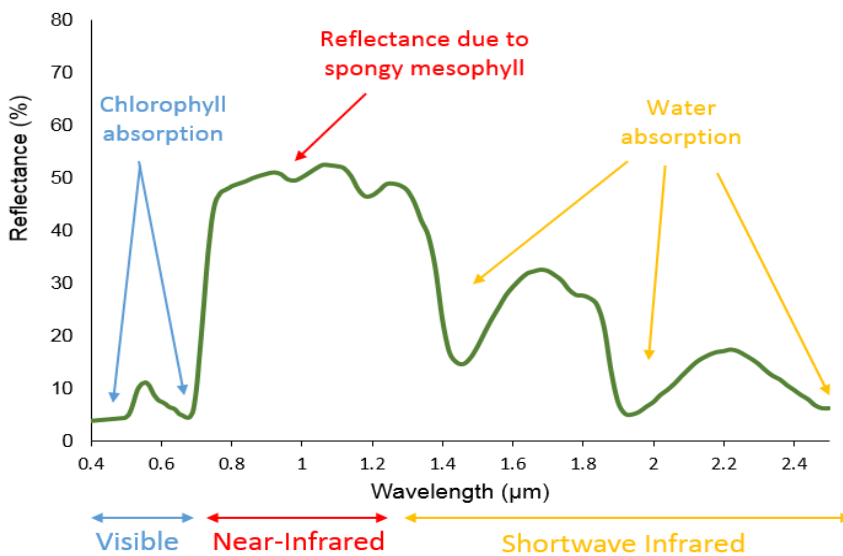


Fig. 3.19. Typical spectral reflectance of plants.

Typically the differences in the reflectance between 550nm and 800nm can be used to discrimination of plants (Paap, Askraba, Alameh, & Rowe, 2008) from water and soil because electromagnetic reflectance are differs for plants in these specific wavelengths. The spectral image and reflectance of a plant are shown in Fig. 3.20.

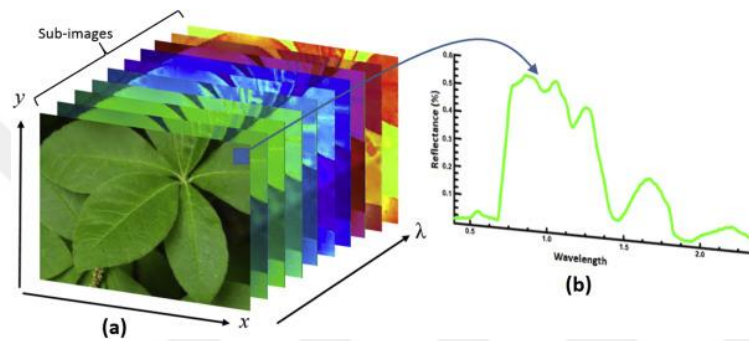


Fig. 3.20. Spectral image and reflectance of a plant.

In order to discriminate the status of a plant it is possible to use a passive sensor in daylight conditions. Sun emission contains both Red and NIR bands that are shown in Fig. 3.21.

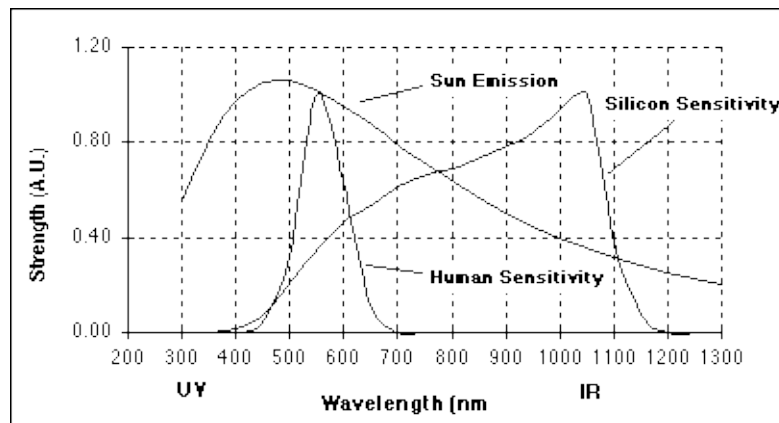


Fig. 3.21. Reflectance of plant, water and soil.

3.3.2 Multispectral Camera – Spektra TSL128RN

In this thesis, a custom-designed Multispectral Camera hardware and software designed and manufactured for detecting plant healthiness. The developed multispectral camera mounted on UGV as a disease-detecting sensor. It consists of line scanners, bandpass filters, varifocal lenses, laser modules, a microcontroller, a

wireless communication module and supports USB communication. A specialized software interface designed and coded for this device to utilize data acquiring from the sensor and calculating NDVI outputs. The 3D model of the designed device shown in Fig. 3.22 and its block diagram is shown in Fig. 3.23, respectively.

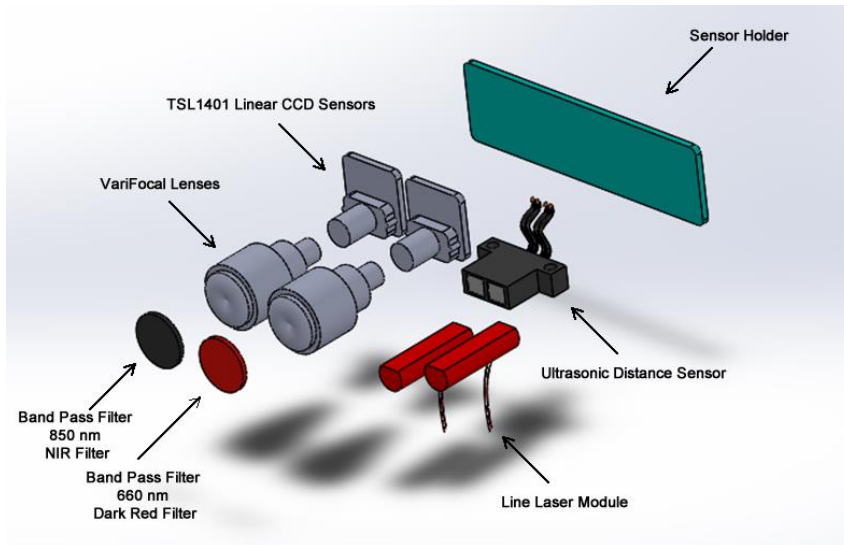


Fig. 3.22. 3D model of the Multispectral Camera.

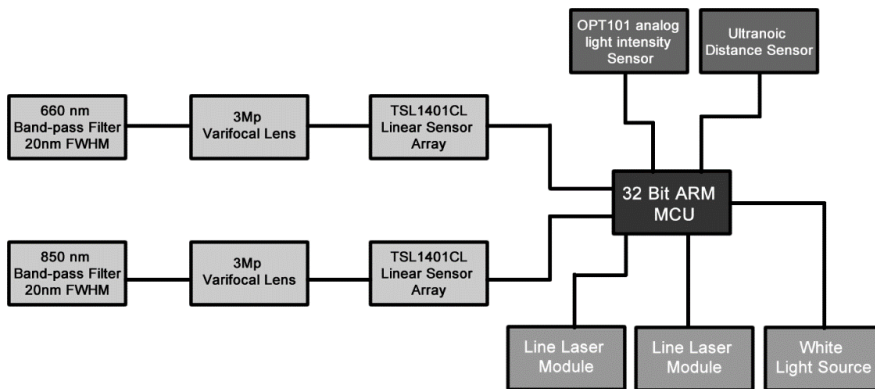
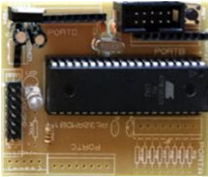


Fig. 3.23. Block diagram of the Multispectral Camera.

Table 3.4. Components of the Multispectral Camera.

Component	Model	Figure	Description
Line scanner	TSL1401CL		128X1 Linear CCD Sensor
850nm Bandpass filter	Optical Narrow Bandpass Filter		850NM Wavelength Bandpass Filter
660nm Bandpass filter	Optical Narrow Bandpass Filter		660NM Wavelength Bandpass Filter
Lens	Varifocal lens		3 Megapixel Fixed Iris M12 HD 2.8-12mm Varifocal Lens
Wireless Transceiver	DRF7020D27		GFSK transceiver Module -27dBm 433Mhz transparent RF module.
Microcontroller	At32MDB01		A custom designed development board is used for data acquisition.
USB interface	FT232RL FTDI		USB to serial UART Interface.
Laser module	Line Laser Module		Linear output Laser Module.

3.3.3 The hardware of the Device

The main sensor module TSL1401CL is a linear sensor array consists of a 128×1 array of photodiodes, associated charge amplifier circuitry, and an internal pixel data-hold function that provides simultaneous-integration start and stop times

for all pixels. It provides 400 Dots-Per-Inch (DPI) sensor pitch and operates at 8 MHz with a single 3-V to 5-V power supply. The voltage developed by the sensor at analog output (AO) with 1mV_{rms} output noise voltage is given in Eqn. (3.9).

$$V_{out} = V_{drk} + (R_e)(E_e)(t_{int}) \quad (3.9)$$

where: V_{out} is the analog output voltage for white condition V_{drk} is the analog output voltage for dark condition, R_e is the device responsivity for a given wavelength of light given in $V/(\mu\text{J}/\text{cm}^2)$, E_e is the incident irradiance in $\mu\text{W}/\text{cm}^2$, t_{int} is integration time in seconds.

The responsivity of the photodiode used in this line scanner sensor shown in Fig. 3.24 that indicates it is possible to sense both Red and NIR bands

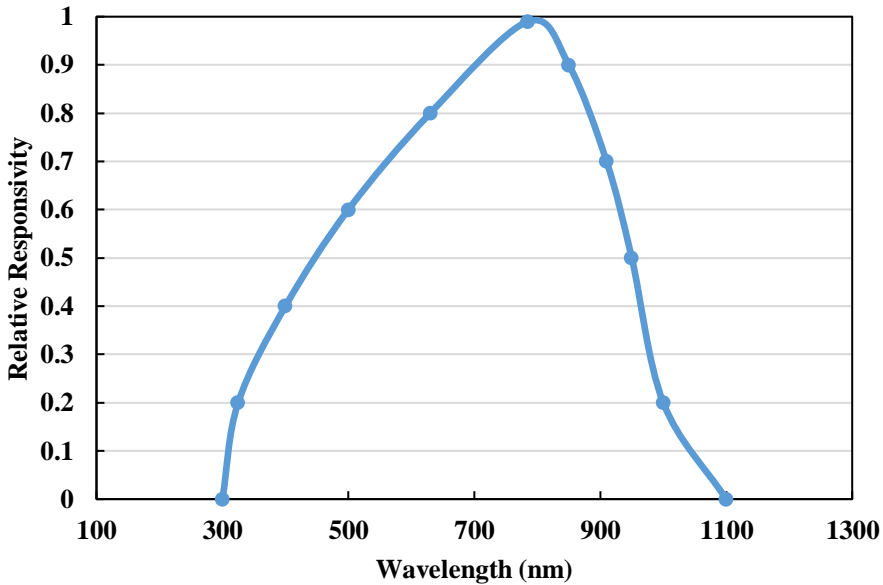


Fig. 3.24. Photodiode spectral responsivity.

An MCU is used in this multispectral camera to obtain output of the line scanner sensors and transfer it to the GCS. In line with the purpose, an electronic development board designed and PCBs are printed. The schematic design of this microcontroller board is shown in Fig 3.25 and its PCB design is shown in 3.26. 3D

model of the board is shown in Fig 3.27 (a) and the manufacturing image is shown in Fig 3.27 (b).

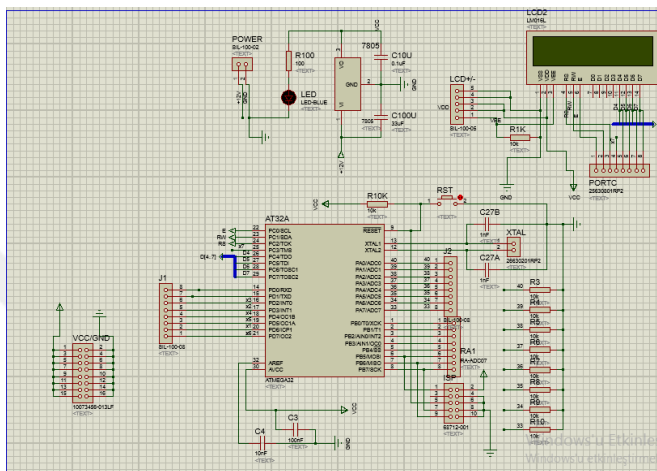


Fig. 3.25. Schematic design of the board.

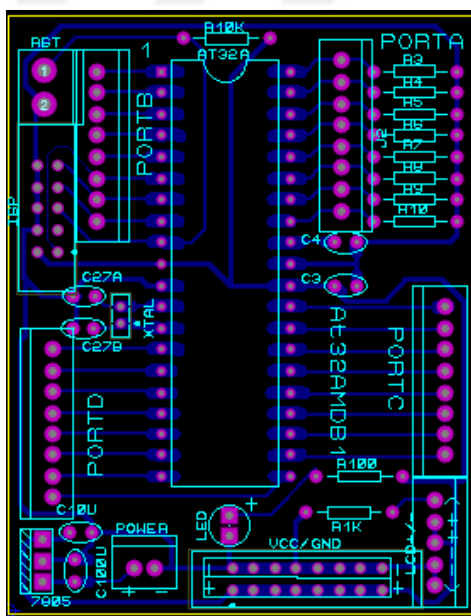


Fig. 3.26. The printable design of the board.

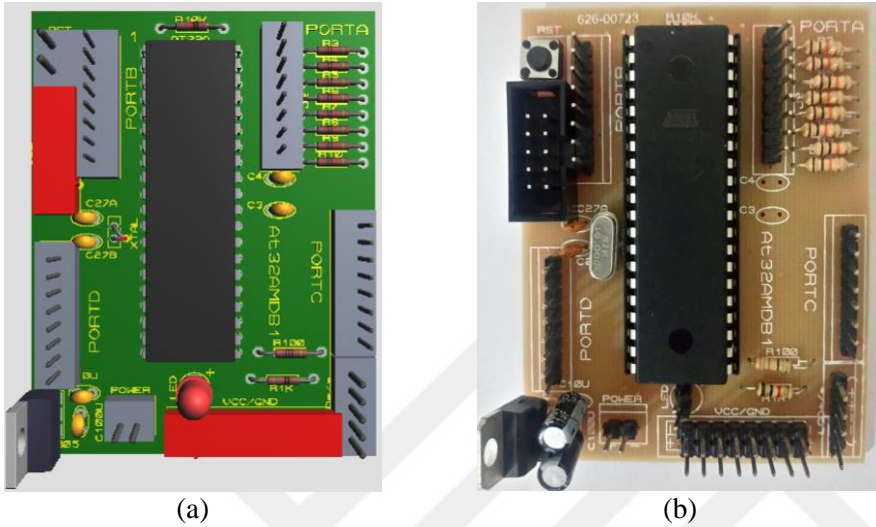


Fig. 3.27. 3D Model of the board (a) and the Printed Circuit Board (PCB) (b).

3.3.4 Calibrating Steps of the Device

Field of View refers to the visual angle of a lens. Horizontal FoV (HFoV) describes horizontal dimensions and Vertical FoV (VFoV) describes vertical dimensions of the measurement field. For calculating the Field of View (FoV) of the Multispectral Camera, the relationship between the focal length of a camera and sensor size is investigated (Fig 3.28).

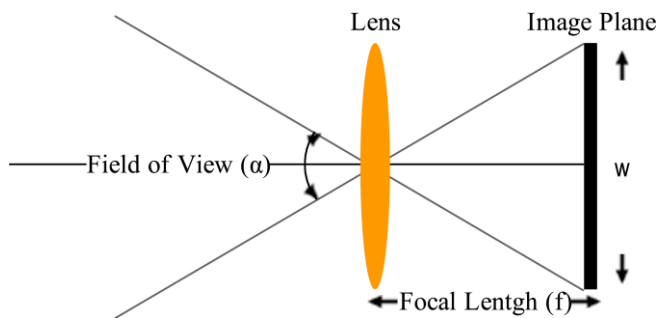


Fig. 3.28. Relationship between Focal Length, FoV and sensor size.

The FoV (α) can be calculated using trigonometry that is related to image plane dimension (w) and focal length (f) using the Eqn.(3.10) or (3.11).

$$\alpha = 2 \tan^{-1} \frac{\omega}{2f} \quad (3.10)$$

or

$$f = \frac{\omega}{2} \cot \frac{\alpha}{2} \quad (3.11)$$

Based on the above 3.11 using the image width ω , the field of view α and the focal length f can be calculated in pixels. This multispectral camera uses two separate lenses for two distinct bands. In order to eliminate non-coincident pixels for this camera a 3D model of FoV is simulated in computer modeling software as shown in Fig. 3.29 (a). Sensors of the multispectral camera are placed side by side and a target area is drawn to 1-meter distance from the sensors vertically. The angles of the sensors are for horizontal FoV and vertical FoV, 51.18° and 30.04° respectively as indicated in Fig. 3.29 (b).

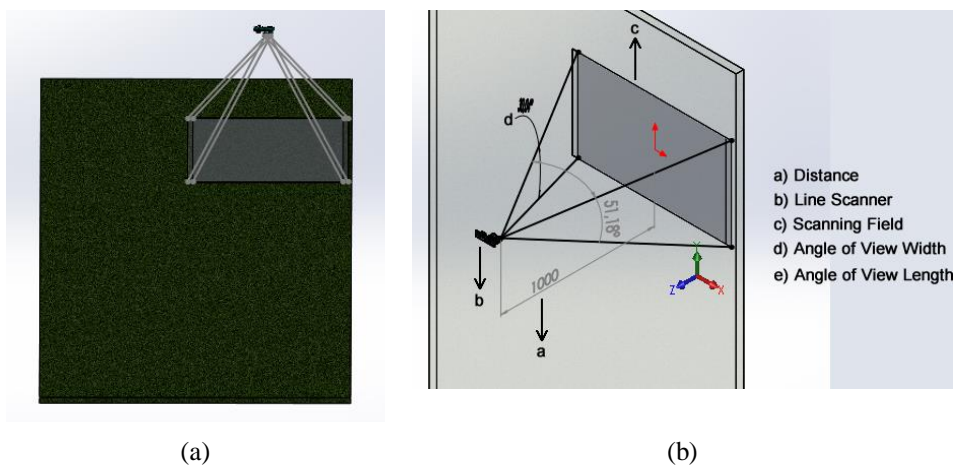


Fig. 3.29. The 3D model of sensor and sensing area relationship (a) and simulation of the FoV (b).

Total scanning FoV and the non-coincident area in 3D model of FoV are shown in Fig. 3.30 (a) and Fig. 3.30 (b), respectively.

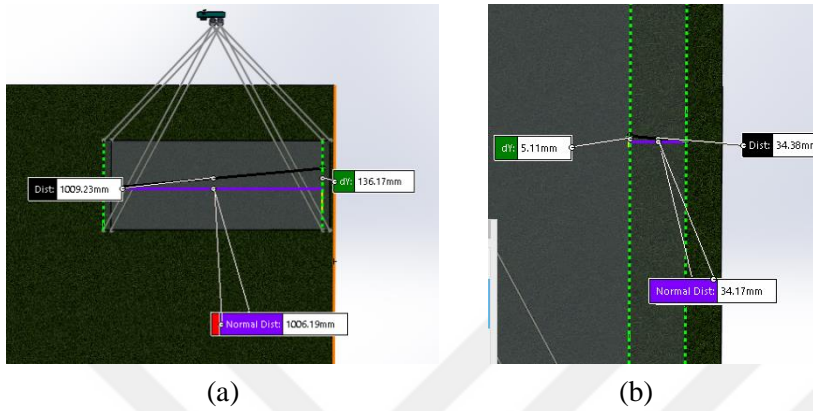


Fig. 3.30. Calculation of the intersecting area.

Horizontal and vertical FoVs of the sensors shown in Fig. 3.31.

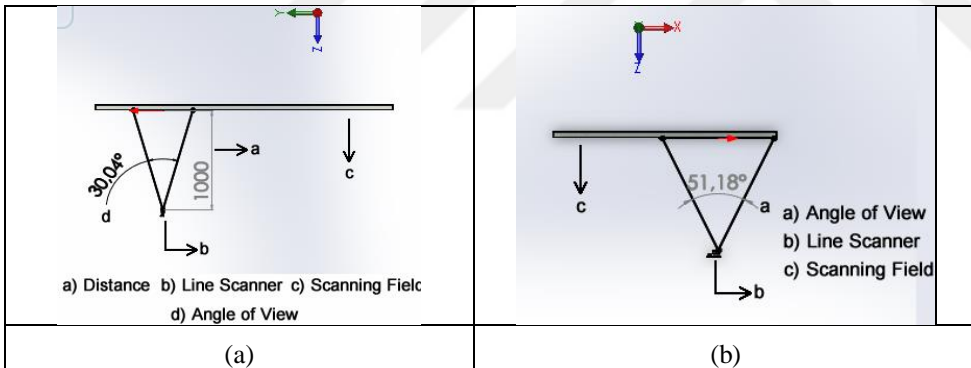


Fig. 3.31. FoV of the sensors, vertical FoV (a), horizontal FoV (b).

A simple 2D image demonstrated to explain intersection and difference to determine non-coincident pixels of sensors shown in Fig 3.32 for horizontal FoV.

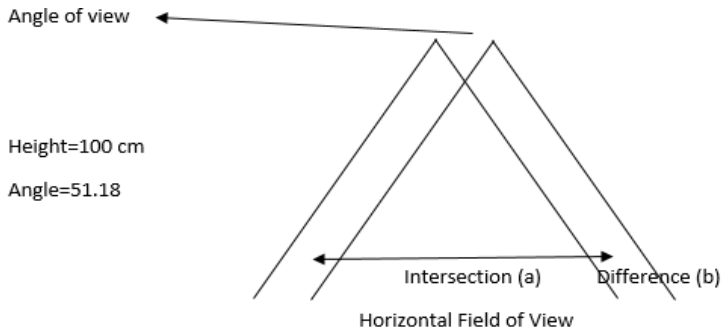


Fig. 3.32. Intersecting parts for horizontal FoV.

The ratio between intersecting view and non-coincident view V_R (3.12) is

$$V_R = V_i/V_d \quad (3.12)$$

non-coincident pixel count C_{pi} (3.13),

$$C_{pi} = \frac{C_p}{V_R} \quad (3.13)$$

intersecting pixel count C_{pii} is (3.14),

$$C_{pii} = C_p - C_{pi} \quad (3.14)$$

where intersecting view V_i , non-coincident view (difference) V_d , the pixel count of the sensor C_p , non-coincident pixel count C_{pi} , intersecting pixel count C_{pii} ,

For $V_i = 34.17$ mm, $V_d = 1006.19$ mm, $C_p = 128$, C_{pi} is calculated 4.35 (~ 5) pixels and 123 pixels are intersecting. For preventing from mounting and manufacturing errors 100 pixels Centered in Sensor are used and 14 pixels from left and right of the sensor are eliminated (3.15).

$$[1-14 \text{ not used, } 14-114 \text{ used, } 114-128 \text{ not used}] \quad (3.1)$$

In order to calibrate the focal length of the multispectral camera lenses a CCTV camera is used (Fig 3.33). A target object is settled in front of the camera at 1-meter distance. Focal adjustment of the lenses is set manually by rotating lenses until the target image is clearly seen and then lenses are fixed.

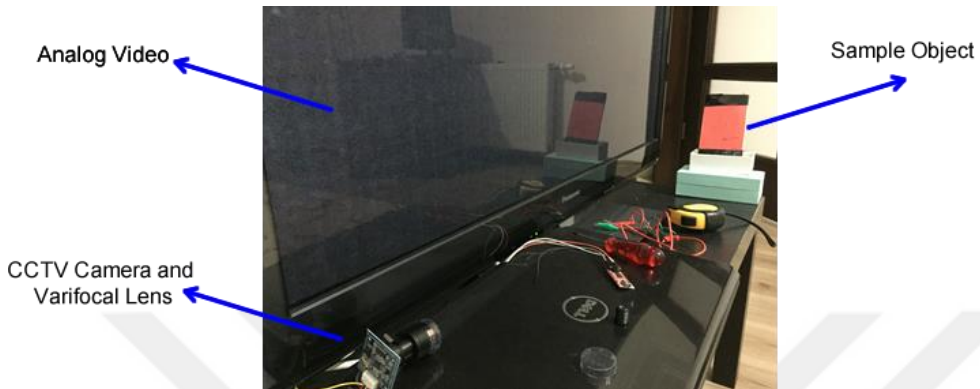


Fig. 3.33. Focal Length Adjusting

In order to calibrate multispectral camera color printed calibration images (Fig. 3.34) and the relative spectral responsivity of the sensors are investigated. Calibration stage completed in the day time between 09:00-16:00. Varifocal lens focusing and zoom is adjustment accomplished using a CCTV camera shown in Fig. 3.33.



Fig. 3.34. Adjustment focal length and target object distance of Varifocal lenses.

3.3.5 Software for the Device

A desktop software interface is shown in Fig. 3.35 used for calibrating of the Multispectral Camera unit. In this calibration stage, an interface is coded in C++ language as desktop software. This interface shows each received pixel in real-time for Red and NIR bands. It calculates NDVI results using these two bands and offsets for calibrating the Multispectral Camera.

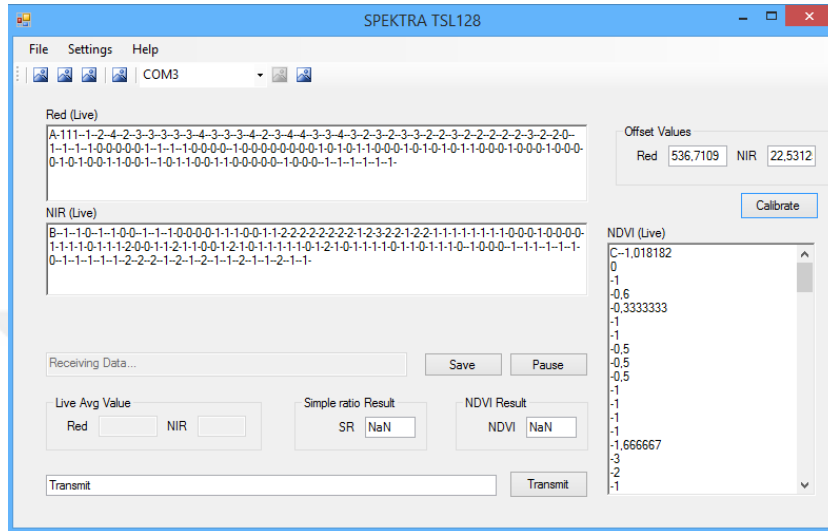


Fig. 3.35. Desktop Software for Calibration of Multispectral Camera.

In addition, another desktop software (Fig. 3.36) is coded for image acquisition from the Multispectral camera and is coded in the C++ language. This software shows real-time Simple Ratio (SR) with NDVI data and includes a scale to demonstrate the meaning of the results.

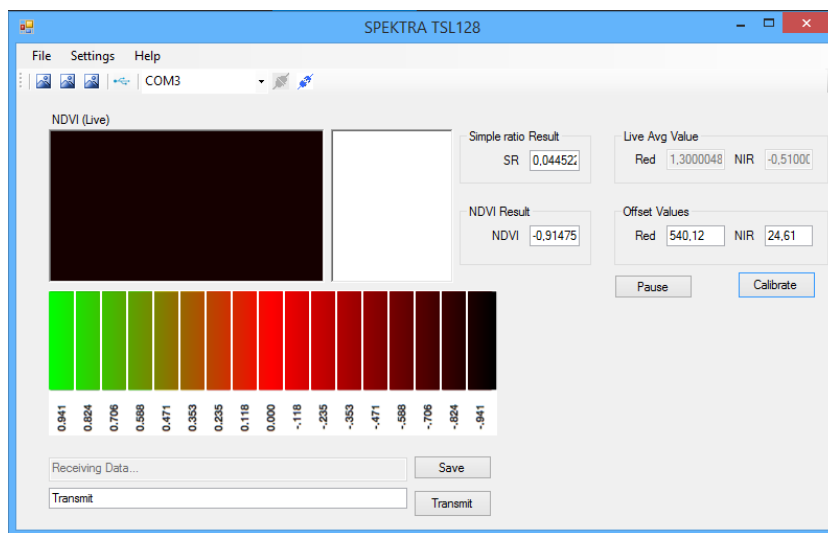


Fig. 3.36. Desktop software for image acquisition of the multispectral camera.

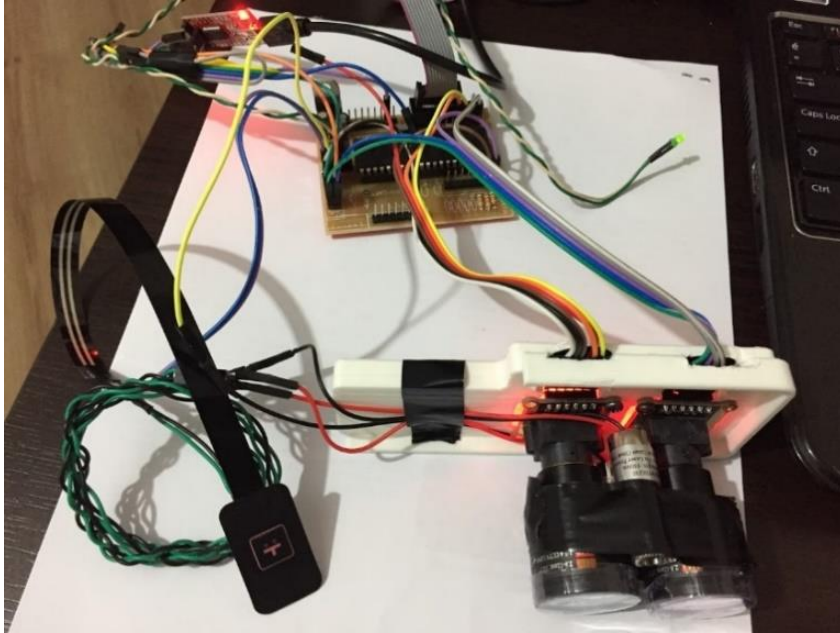
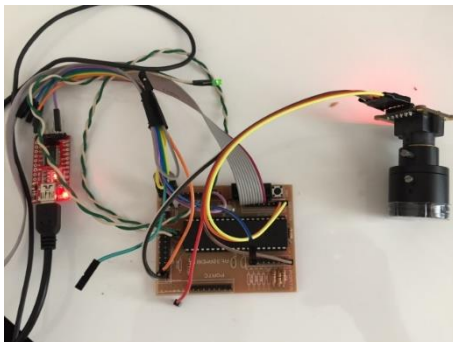


Fig. 3.37. Multispectral Camera assembly.



(a)



(b)

Fig. 3.38. Multispectral camera units: electronic board and lenses (a), filters and laser module (b).

3.3.6 Measurements using NDVI Devices

In order to evaluate obtained results from Multispectral Camera a commercial device named PlantPen NDVI 300- NDVI (Fig. 3.39) is used for preliminary NDVI tests. The NDVI measurement device is used in tests for finding the NDVI value of sample Plants.



Fig. 3.39. PlantPen NDVI 300- NDVI.

Three different plants are investigated (Fig. 3.40) and four leaves are tested for each plant. Four status are considered for each leaf named Diseased, Healthy, Old, Semi-healthy.

Multispectral camera tests are implemented for both indoor and outdoor. For each test, raw data (Fig. 3.41) is recorded that acquired from the multispectral camera and processed in Microsoft Excel. In order to calculate the response of each pixel offsets removed and coefficients applied according to the spectral responsivity of the sensor.

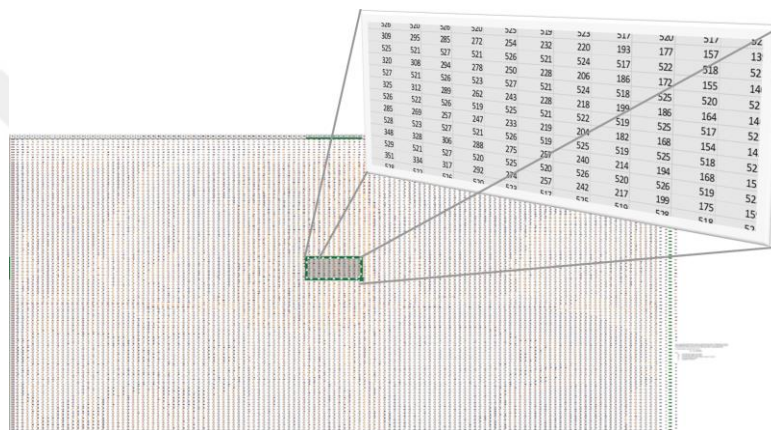


Fig. 3.41. Raw data example.

Fig tree leaves, grass and black background shown in Fig 3.42 are used in outdoor tests. Tests are repeatedly implemented 12 times during daytime and prevented from saturation for the multispectral camera.



Fig. 3.42. Fig tree leaves and grass.

Planetree leaves used in indoor tests for semi healthy and healthy leaf and background discrimination. The multispectral camera and leaves shown in Fig. 3.43



Fig. 3.43. The multispectral camera and plane tree leaf with dark red to brown background.

The custom-designed multispectral camera named Spektra TSL128-RN stands for:

- Spektra: Spectral Imaging,
- TSL: Line Scanner Code,
- 128: Pixel Count,
- R: Red Bandpass Filter,
- N: NIR Bandpass Filter.

3.4 Unmanned Aerial Vehicle

In recent years Mid-Size UAVs are becoming popular for civil applications such as transporting and agricultural spraying. These kinds of applications expected to be high power with bigger propellers to lift heavier payloads. Nowadays, the importance of Mid-Size UAVs is rapidly increasing for autonomous transporting and farmland administration. For this purpose, commonly used Small-Size and Mid-Size UAVs are typically constructed using carbon fiber frames because of rapid prototyping and procurable in markets. Nevertheless, these kinds of UAV chassis have manufacturing limits, costs are high and it is not adequate when size of chassis

should be larger. In order to achieve the lack of low-cost Mid-Size agricultural spraying UAV production, in this thesis a VTOL (Vertical Take-off and Landing) UAV designed, analyzed, developed and experimented using a testing mechanism. Parts of the UAV is modelled using SolidWorks in 3D and assembled (Fig 3.44). The chassis and the arm are separately assembled and analyzed.

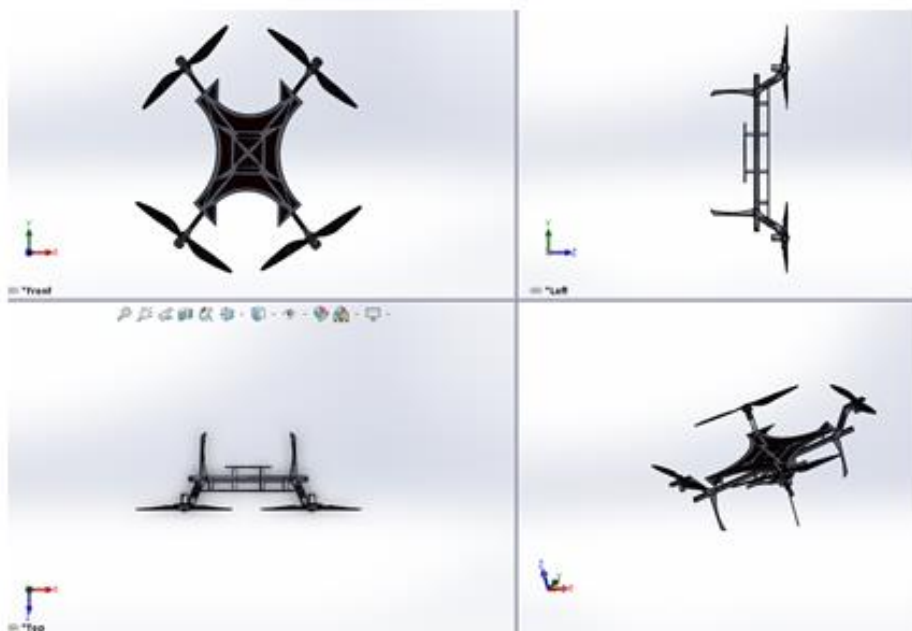


Fig. 3.44. Assembly of the UAV.

The designed VTOL UAV consists of four-rotors and it is named quadcopter in nomenclature. These four motors are driven by Electronic Speed Controllers (ESC) using Pulse Width Modulation (PWM) signal. Lithium polymer batteries are used due to their lightweight structure with high current performance. A battery level sensor is used to indicate the remaining battery level. A flight controller is used for hovering and maneuverability of the vehicle. Moreover, for positioning, an electronic compass and a Global Positioning System (GPS) module mounted on it. It also includes Inertial Measurement Units (IMU) such as gyroscope, accelerometer and barometer. An electronic development board is used as the main controller unit (MCU) for connecting to the GCS to establish the plant-spraying goal. An RF transceiver module is used to provide communication between UAV and GCS. A spraying boom is mounted on the vehicle with an electronic controller on it. The

relationship between these units shown in the block diagram of the VTOL UAV in Fig. 3.45 and materials are listed in Table 3.5.

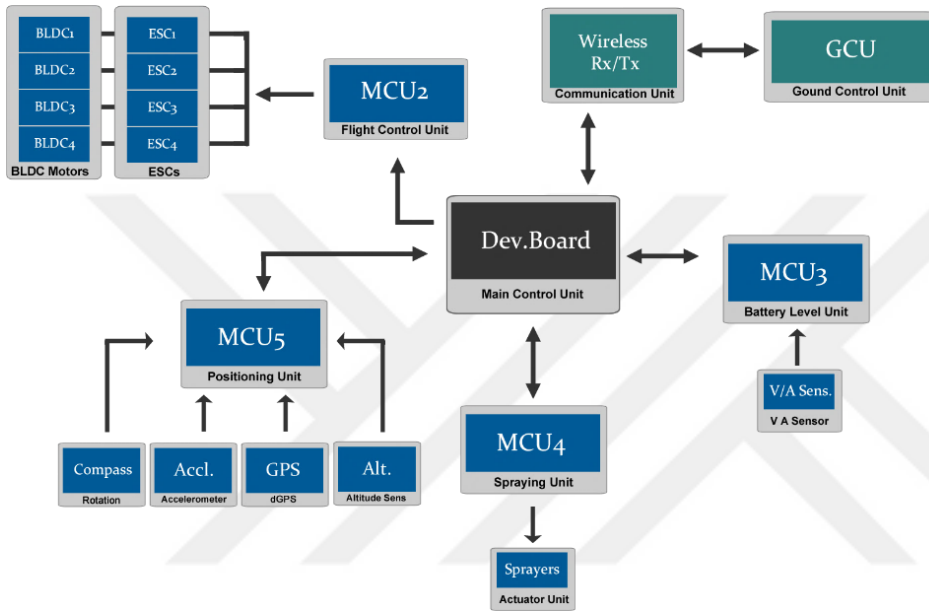


Fig. 3.45. Block Diagram of UAV.

Table 3.5. Components of the VTOL UAV.

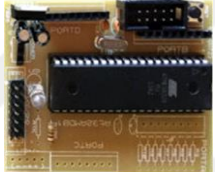
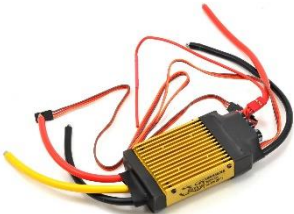
Product	Specifications	Description & Images
Multicopter Flight Control Board	Pixhawk PX4 PWM/(C)PPM/SBUS/Spektrum GPS Support Internal IMUs Compatible with VTOL UAVs	
Microcontroller	Atmega32A 8Bit 32 I/O 16 MHz Timer	
BLDC Motor	XNova 4535 520KV 6.5KW Max 180A	
ESC	Scorpion Commander V 59V 160A ESC Opto 59V 160A Opto ESC	
Propeller	Carbon Fiber Propellers 3010	
Wireless Transceiver	DRF7020D27 GFSK transceiver Module -27dBm 433Mhz transparent RF module.	

Table 3.6. Components of the VTOL UAV (Continued).

Battery	Li-Po 10000mAh 22.2V 25C 6S1P	
GPS	UART GPS NEO-8M-C NEO-8series u-blox 8 GNSS modules	
Voltage and Current Sensor	AttoPilot Voltage and Current Sense Breakout <ul style="list-style-type: none"> • 51.8V Max • 89.4A Max • Very low zero current offset • Analog output scaled for 3.3V ADC <ul style="list-style-type: none"> • Self Powered 	

3.4.1 The Chassis and Arm

In this study, the designed frame (Fig. 3.46) for the VTOL UAV is prototyped using Al 6063-T6 rectangle profile tubes and Al 6068-T6 sheet. It is constructed using weldable tempered aluminum alloys that have proof strength of 240 MPa and 310 MPa, respectively. Finally, total weight of the chassis is about 3.5 kg. It is suitable to lift up to 40 kg payload with 4.3 Factor of Safety (FoS). It is a low-cost solution and modifiable when compared to common carbon fibre frames in markets. The chassis of the UAV is designed in 3D modeling software and structural analysis is accomplished using Finite Element Method (FEM). The UAV chassis is manufactured by using most common industrial techniques according to the draft of the chassis.

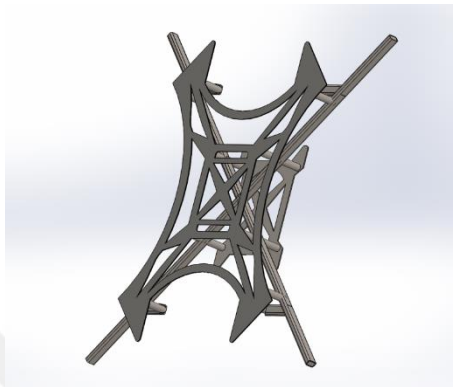


Fig. 3.46. UAV Chassis 3D model (Isometric view).

The chassis is constructed (Fig. 3.48) using weldable tempered aluminum alloys that have proof strength more than 240 MPa. Its draft for manufacturing is shown in Fig 3.47.

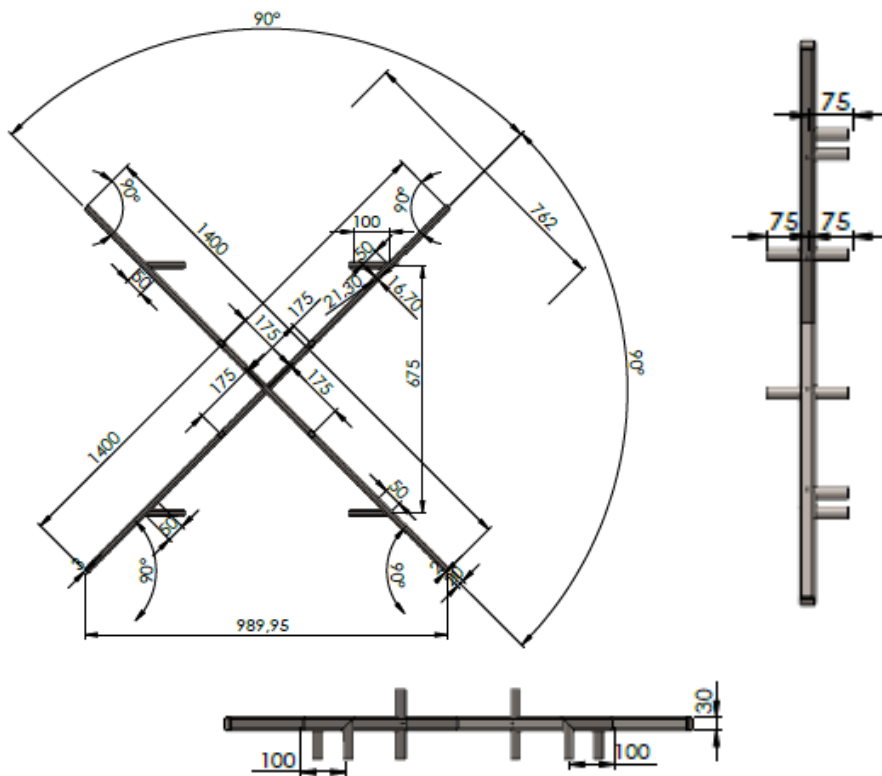


Fig. 3.47. Draft of the UAV chassis for manufacturing.

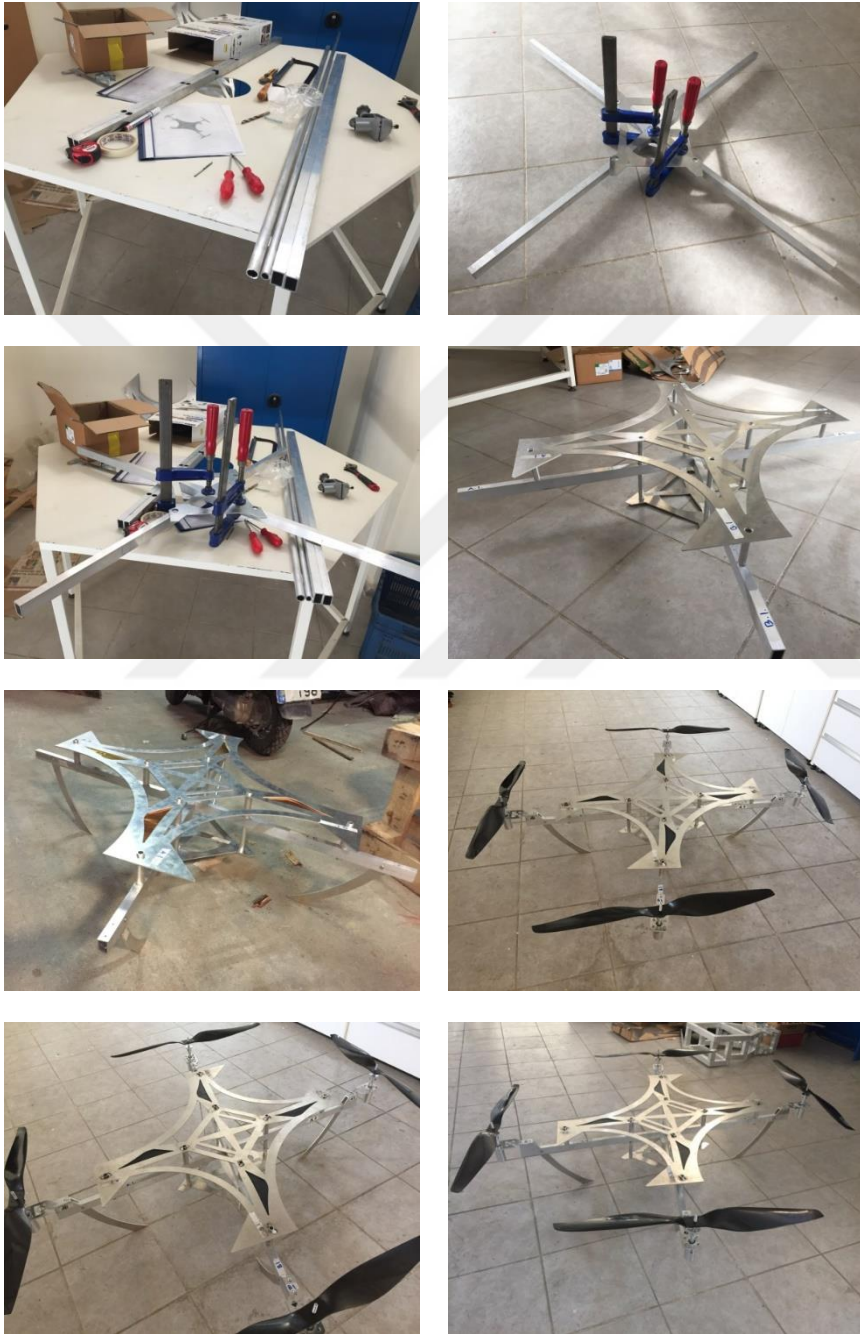


Fig. 3.48. UAV prototyping images.

FEA method is used to analyze frame for stress, strain, FoS and displacement parameters for chassis and manufacturing images are shown in Fig 3.48. Computer

based structural analysis results of the UAV chassis are compared with experimental test results for stress, strain, displacement and Factor of Safety (FoS) parameters.

3.4.2 FEM Analysis

The FEM analysis is accomplished using the SolidWorks Static Structural Simulation tool. The bottom plate of the UAV chassis is fixed and 250N force applied to the terminals of the chassis separately as shown in Fig.3.49.

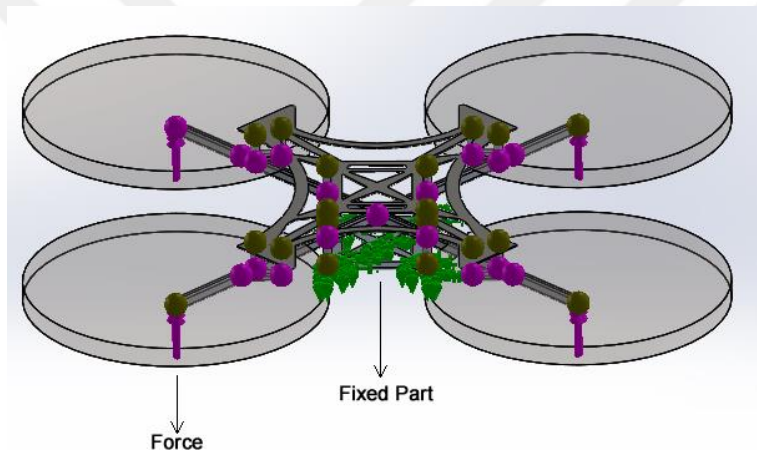


Fig. 3.49. Chassis FEA.

Recently, UAVs Carbon fiber frames with Al alloy connectors are frequently used because these frames and connectors are common in the market. On the other hand, these frames have limits for mass production, modifying and welding. However, Al is a lightweight material and that is commonly used in industry because of its high strength at low density. Al alloys average density is close to 270 kg/m^3 , 7000 series Al alloys have yield strength close to 540 MPa. but lack of weldability and 6000 series Al alloys are preferable as they can be welded and their yield strength is very close to low carbon steel.

The designed VTOL UAV arm is manufactured using Al 6063-T6 rectangle weldment profile tubes, Al 6068-T6 sheets, and gear reducer and connector parts are produced using Al 7075-T6. The VTOL UAV arm weight is 1.0 kg and close to carbon fiber arms' weight sold in the market. The arm is fixed and 250N force applied to the main shaft holder that provides thrust to the arm as indicated in Fig. 3.50.

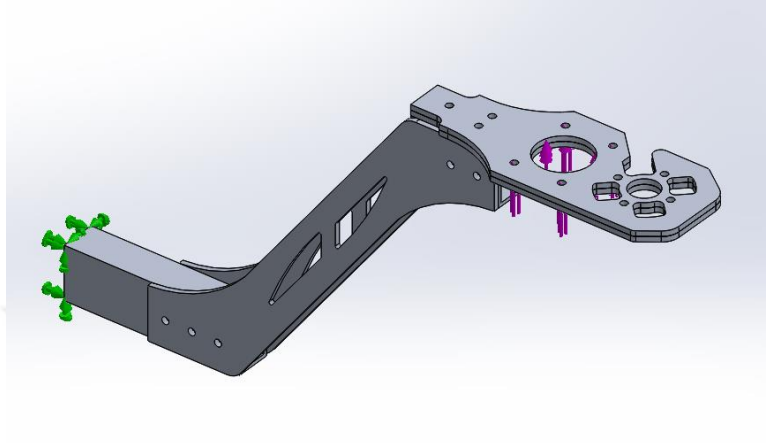


Fig. 3.50. VTOL UAV Arm design.

3.4.3 Modal Analysis

Modal Analysis is investigated due to vibration caused by propellers for aluminum UAV chassis (Fig. 3.51). The experimental Modal test is conducted using DEWESOFT Signal Analyzer with a 3 Axis accelerometer and a modal hammer. Modal hammer (Fig. 3.52(a)) is used as input and a 3-axis accelerometer (Fig. 3.52 (b)) is employed as an output generator for the Signal Analyzer. 24 nodes (Fig. 3.53) are defined and investigated with a roving hammer.



Fig. 3.51. Modal test setup.



Fig. 3.52. 3 Axis accelerometer and Modal Hammer.

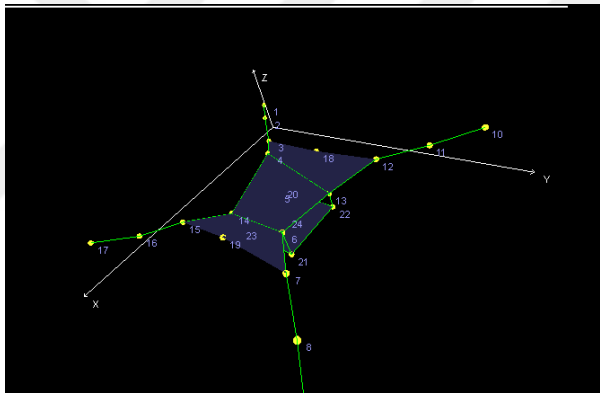


Fig. 3.53. The shape of the UAV with defined Nodes and Traces.

In modal tests for increasing the coherence for each node, three times repetition (Fig. 3.54) is chosen with a roving hammer.



Fig. 3.54. Three times repetition.

Theoretical results are obtained using Natural Frequency Analysis tool in SolidWorks Simulation. FEA modal analysis is conducted for the free-free body shown in Fig. 3.56 and results are investigated for the first five modes (Fig. 3.55) of free vibrations.

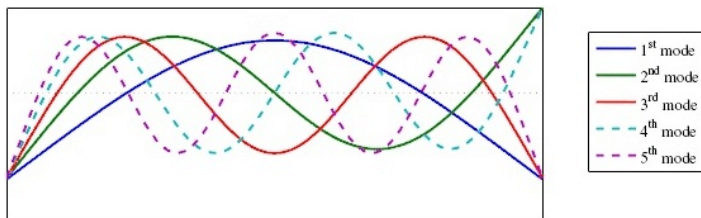


Fig. 3.55. First five mode shapes of a free-free beam (Chellapilla, 2016).

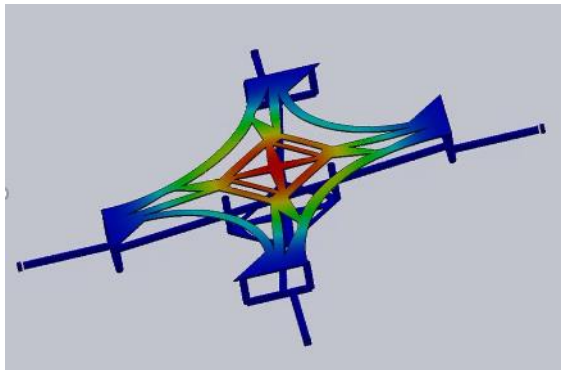


Fig. 3.56. Natural frequency analysis of the UAV chassis.

3.4.4 Performance of the Propellers

The thrust produced depends on the density of the air, the propeller's RPM, its diameter, the shape and area of the blades and its pitch. It is rather difficult to predict the thrust produced by a propeller with accuracy, since props with the same diameter and pitch often have different blade shapes and areas and may be more or less flexible depending on the brand and the type.

A propeller transforms rotational motion from a power source into the stream of the fluids that surrounds it for pushing the propeller to the forward direction by producing thrust at the bottom of the propeller. Performance of a propeller is directly related to blades, which is a rotating airfoil for producing lift and drag force. Typically, propellers have two or more blades less than 6 and blades usually twisted to increase efficiency. The lift is a parameter of the net force that is perpendicular to the direction of flow and drag is another parameter of the net force along the flow direction. The force generated on the surface of the blade by the rotation of the propeller is the sum of two parameters of the force those are lift and drag. A cross-section of the propeller blade that shows forces on a blade such as lift and drag is given in Fig. 3.57.

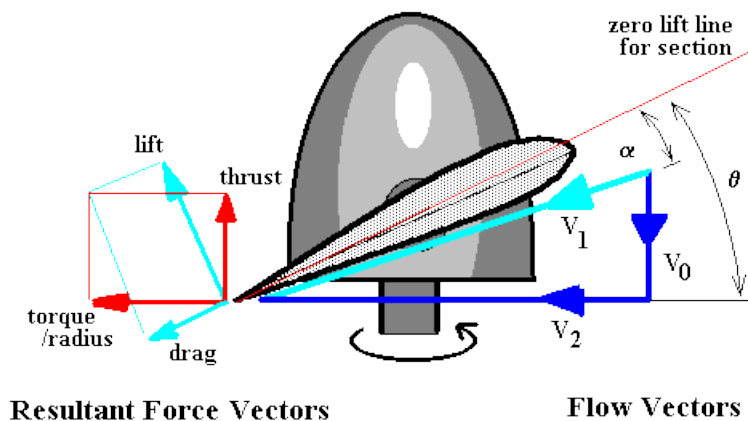


Fig. 3.57. Forces on a blade such as lift and drag (Propeller Theory, 2019).

If it is assumed that the spinning blades of a propeller is actuating like a disk through which the surrounding fluid passes (actuator disc in Fig 3.58). A propeller mounted on a rotor which turns the propeller and does work on the airflow. Therefore, there is a visible difference in pressure across the propeller disk and an actuator disc can be considered as a propeller plane in order to investigate pressure changes.

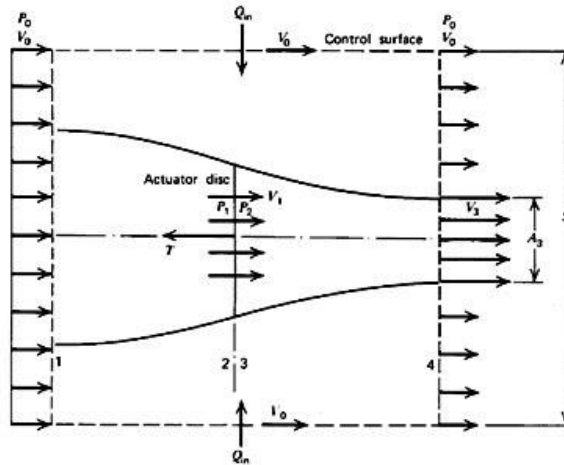


Fig. 3.58. Schematic of a propeller propulsion system (McCormick, 1979).

According to the Simple Momentum Theory, the thrust is perpendicular force generated by the actuator disk that is equal to the pressure jump times the propeller disk area. The equation of the thrust force (3.16) expressed explains how a propeller produces thrust by pressure changes.

$$\text{Thrust} = F = \Delta p \cdot A \quad (3.16)$$

where the pressure changes by "delta p" (Δp), propeller disk area A , the thrust generated by the propeller disk is F .

The mechanical forces by the effect of the pressure jump are conducted at every point on a propeller surface, which affects perpendicular to the surface. The net force calculation can be done by integrating the force variations around the whole surface of the propeller blades. The pressure will vary for every point for moving fluid, related to the velocity. The net force can be determined by calculating the pressure distribution when the velocity distribution examined by using Bernoulli's equation. When the velocity of the fluid is low, and without the effect of external energy is included in the flow regime, the correlation of pressure with velocity can be expressed by Bernoulli's equation. Without concerning boundary layers for an ideal fluid, the surface of a propeller is a streamline. In front of the disk indicated in Fig 3.58 the total pressure (p_{t0}) equals the static pressure (p_0) plus the dynamic pressure (p_d).

Pressure difference is

$$\Delta p = p_{t_e} - p_{t_o} \quad (3.17)$$

where Δp ; pressure difference, p_{t_e} ; inlet pressure, p_{t_o} ; outlet pressure

$$p_{t_e} = p_o + p_d \quad (3.18)$$

$$p_{t_o} = p_o + p_d \quad (3.19)$$

$$p_d = \frac{1}{2} \rho v^2 \quad (3.20)$$

From the equations indicated in (3.17)-(3.20) force-pressure relationship can be expressed as indicated in equations (3.21 and 3.22).

$$\Delta p = \frac{1}{2} \rho \cdot (V_e^2 - V_o^2) \quad (3.21)$$

$$F = \frac{1}{2} \rho \cdot A \cdot (V_e^2 - V_o^2) \quad (3.22)$$

where p_d : dynamic pressure (N/m^2), ρ : density of fluid (kg/m^3) and v : velocity (m/s)

Beyond these theoretical definitions, there is a net integrated force caused by the pressure differences through a propeller's body. The net mechanical force on the propeller's body can be calculated when the surface of the propeller split up into a large spectrum of small parts and integrate up the forces around the entire surface (3.23).

$$F = \sum_{\text{surface}} \vec{p} \cdot \Delta A = \oint \vec{p} \cdot dA \quad (3.23)$$

A propeller accelerates the density of air which flows through the area of the propeller disc. This attitude can be idealized as a stream tube passing through the disc. In fluid dynamics, the Momentum Theory or also well known as Disk Actuator Theory is a theory that describes a mathematical model of an ideal actuator disk. The theory is proper to apply for a propeller or rotor with blades. The Momentum Theory assumes that;

- the flow is inviscid and steady (ideal flow), therefore the propeller does not experience energy losses due to frictional drag
- also the rotor is thought of as an actuator disk with an infinite number of blades, each with an infinite aspect ratio
- the propeller can produce thrust without causing rotation in the slipstream.

From the thrust equation, it is known that the thrust depends on the mass flow rate through the propeller and the velocity change through the propulsion system.

$$T_{theory} = \rho \frac{\pi d^2}{4} \times \frac{p^2}{3600} \omega_{RPM}^2 \quad (3.24)$$

where: T: Theoretical Thrust (N), $\rho=1.225\text{kg/m}^3$, p: diameter (m), d: pitch (m), ω_{RPM}^2 : angular velocity (RPM) (Myunggon Yoon, 2015).

In general, the propeller's length provides more power but also increases heating of the motor, and its pitch provides higher revolutions per minute (RPM) nevertheless it causes more current drawing. Decreasing the prop's pitch or length is the easiest way to solve a heat problem but this limits the performance of the vehicle. To select the right pitch for a propeller, certain parameters need to be investigated such as power consumption, propeller speed limitations and ideal propeller speed, and gear reduction (Garner, W.B. 2009).

The performance data of two propellers are investigated using a propeller thrust test apparatus. Power consumption, thrust and angular velocity relations investigated using the test mechanism shown in Fig. 3.59 for the manufactured arm with two different size propellers. The results obtained from the test mechanism and compared with theoretical calculations.

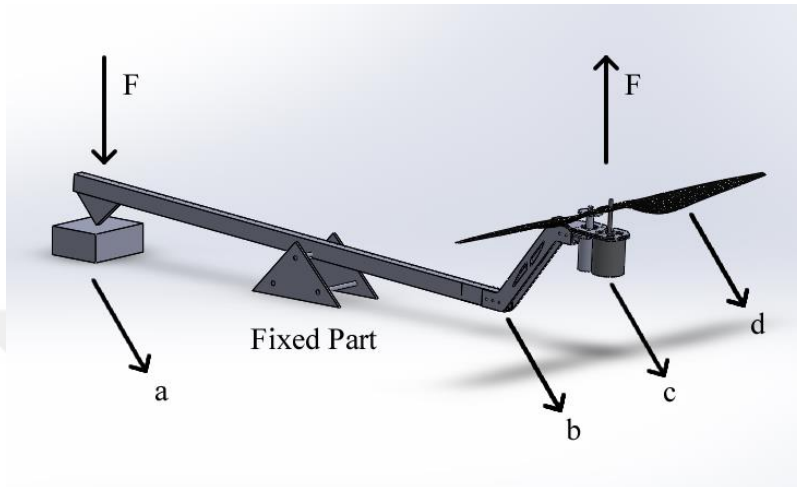


Fig. 3.59. 3D Model of the propeller test mechanism a) precision scale, b) Junction point of the chassis and arm c) motor and gear reducer parts mounted on the motor holder, d) 3010 carbon fiber propeller.

Initial conditions for the experimental setup:

- 6S two pack LiPo battery,
- 520kv, 6500W BLDC Motor,
- 160A ESC,
- 3095 and 3010 Carbon Fiber propeller,
- 20:68 Gear Reduction,
- Air Density (kg/m^3) is 1.225,
- propeller (for 3010 prop.) diameter is 0.762 (m),
- pitch (for 3010 prop.) of the propeller is 0.254 (m),
- propeller (for 3095 prop.) diameter is 0.762 (m),
- pitch (for 3095 prop.) of the propeller is 0,241 (m).

In this experiment, the aim is to investigate the effect of angle of attack for mid-size UAV carbon fiber propellers commonly used in agricultural applications. The attack angle difference investigated by comparing two propellers with the same length and different pitch. For this experiment, a thrust test apparatus developed to acquire thrust force generated by utilizing a scale. Propeller thrust tests implemented to obtain power consumption, angular velocity and thrust force performing for each geometry of propellers, and the graphical results investigated. Graphical evaluation for current and voltage versus angular speed along with power consumption versus generated thrust relations are obtained. The propellers used in this study are shown

in Fig. 3.60. 3010 and 3095 propellers comparison charts are included because of implemented measurement.



Fig. 3.60. 3010 (a) and 3095 (b) propellers.

In order to investigate the effect of the pitch on propeller performance a simple lever mechanism is used to simulate a VTOL UAV arm. The arm is assembled to the custom lever and is balanced out with a counterweight. Thus, thrust force measurements could resemble operational conditions closely as shown in Fig. 3.61. The arm consisted of an electronic speed controller (ESC), a brushless direct current (BLDC) motor, a gear reducer that has a ratio of 20/68 shown in Fig. 3.64 (a) and a carbon fiber propeller mounted on the main gear as shown in Fig. 3.64 (b).

For thrust measurement, the cantilever principle utilized through the test procedure and application method is shown in Fig. 3.61. At the start of every test run, arms of the lever balanced and the scale set to zero so that the measurements for new test runs would be accurate.

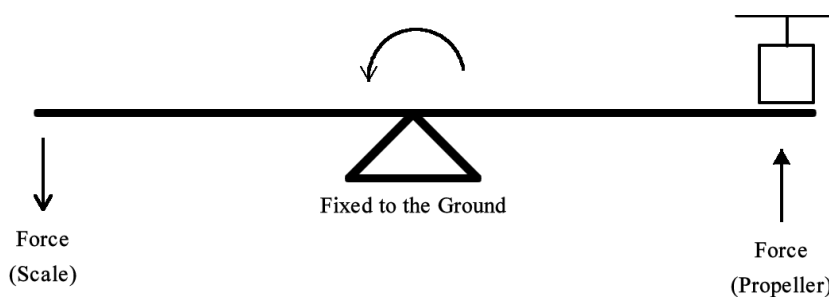


Fig. 3.61. Lever mechanism and VTOL UAV Arm lay-out.

For angular speed measurement, motor frequency from the ESC output measured by utilizing digital frequency meter. Power consumption measurement is carried out

by measuring current from the battery and potential difference of the battery. The connection scheme is given in Fig. 3.62.

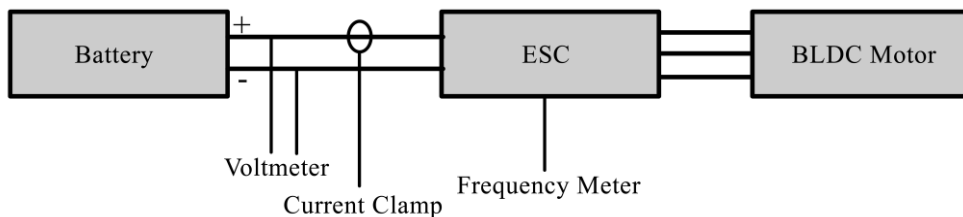


Fig. 3.62. Power and angular velocity measurement method.

Temperature data obtained by measuring all components separately with an IR thermometer. Its measurement range is between $-50\text{ }^{\circ}\text{C}$ and $+600\text{ }^{\circ}\text{C}$ with the accuracy $\pm 1.5\text{ }^{\circ}\text{C}$ above $0\text{ }^{\circ}\text{C}$ and the resolution of this sensor is $0.1\text{ }^{\circ}\text{C}$.

Experimental tests for measuring the performance of the VTOL UAV (Fig 3.63) are accomplished using different size carbon fiber propellers.

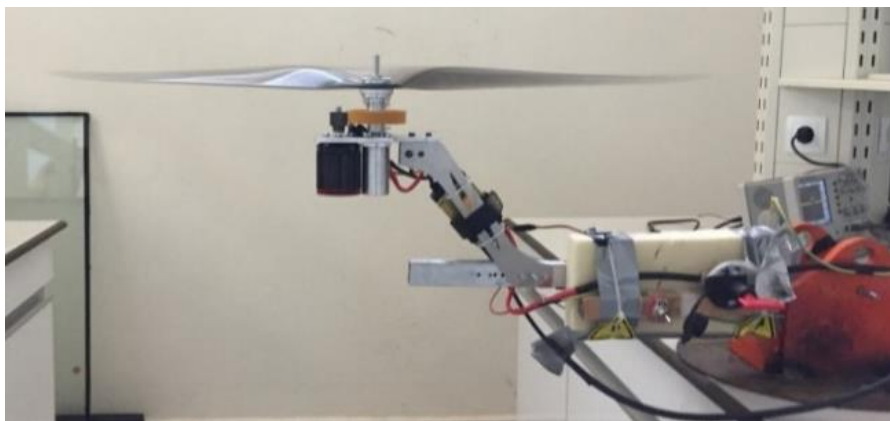


Fig. 3.63. VTOL UAV arm setup.



Fig. 3.64. Mounting of the gear reducer and the propeller.

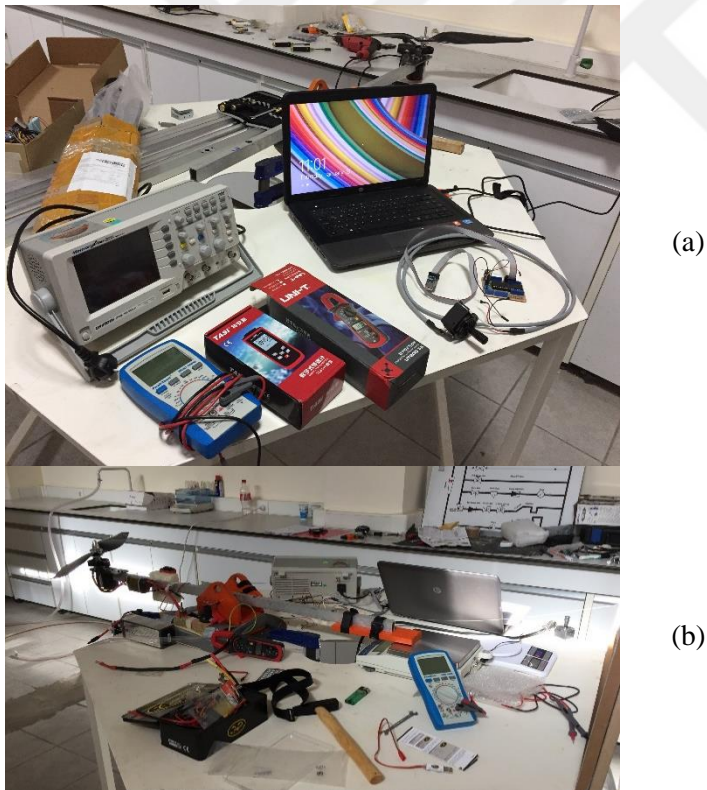


Fig. 3.65. Measuring equipment: Oscilloscope, Multimeter, Current Clamp, IR Tachometer, Joystick and PWM Generator Board (a), Thrust testing mechanism (b).

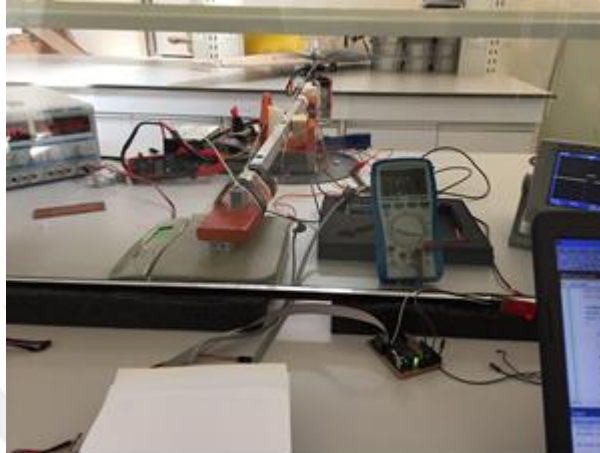


Fig. 3.66. Thrust testing apparatus and measuring equipment.

The arm of VTOL UAV consists of a motor, an ESC and a gear set mounted to one end of the lever, a precision scale is used at the other end of the lever. The spacing between the UAV arm and balance point (center) of the lever is set equal to the distance between the scale and balance point of the lever. The shaft located at the balance point of the lever is assembled to the housing by utilizing bearings (Fig. 3.64 (b)). The housing lets the shaft rotate freely around the horizontal axis, and is fixed to the ground. Weight of UAV arm assembled to the test setup is also balanced by placing an external weight (1.280 kg) to the other end of the lever.

Thrust generation, power consumption, angular speed, temperature, modulation signal and test duration values are obtained by experimental study. The experimental setup is shown in Fig. 3.65. The relationship between the variables, which could be measured with the experimental setup (Fig. 3.66) and the measurement devices are given in Fig. 3.64 (a), and relations are indicated in Fig 3.67.

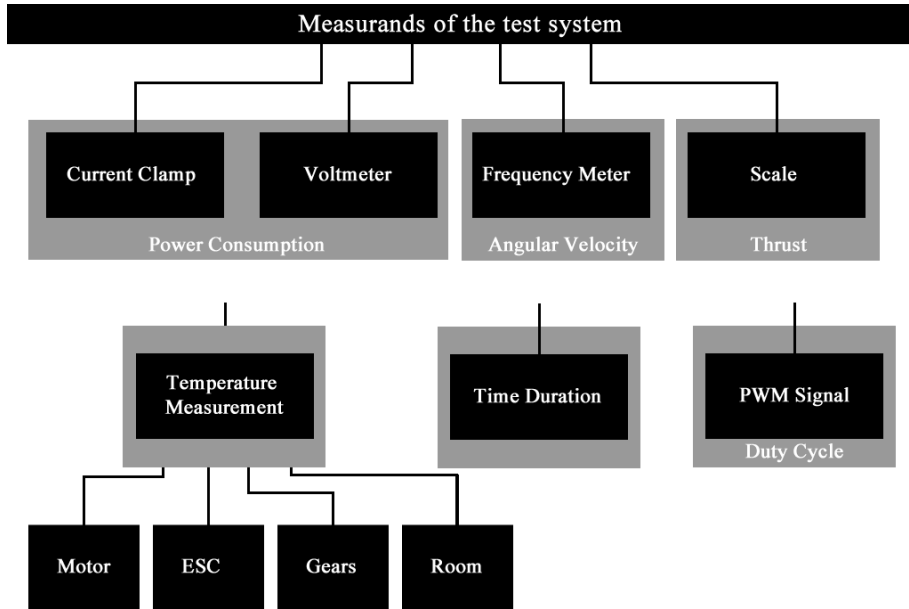


Fig. 3.67. Measurand of the test system.

3.4.5 Flight Duration and Maximum Conditions

In order to calculate the maximum speed of a UAV the physical principles (Meriam and Kraige, 2001) should be investigated. Thrust is the force, which acts on an object perpendicular to its surface. Thrust is a vector quantity because it has both direction and magnitude. For calculating the thrust gravitational force and air drag force should be considered (Fig. 3.68).

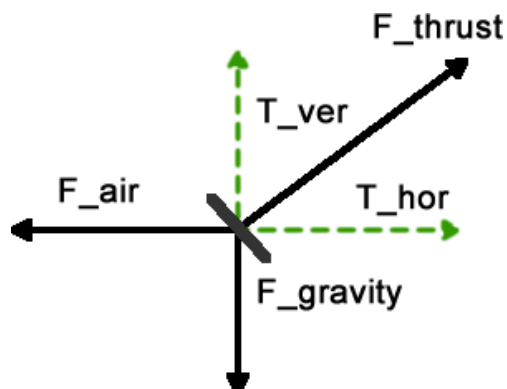


Fig. 3.68. Forces on a UAV.

From Newton's second law of motion (3.25):

$$F_T - F_g - F_{aD} = m \frac{dv}{dt} \quad (3.25)$$

where F_T : Thrust force (N), F_g : Gravitational force (N), F_{aD} : Air drag force (N), m : the mass of the vehicle (kg) and v : speed (m/s).

Respect to the Newton's second law of motion; For the case of a vertical climbing aerial vehicle (3.26):

$$T - mg - \frac{\rho}{2} C_D A_{eff} v^2 = m \frac{dv}{dt} \quad (3.26)$$

where T : total thrust (N), g : gravity of the earth (9.81 N), F_{aD} : air drag force (N), ρ : density of air (kg/m^3), m : mass (kg), v : speed (m/s), C_D : drag coefficient, A_{eff} : effective area of the vehicle (m^2).

For a constant altitude the case at forward flying of the vehicle (3.27 and 3.28):

$$\sqrt{T^2 - (mg)^2} + 2T mg \cos \alpha - \frac{\rho}{2} C_D A_{eff} v^2 = m \frac{dv}{dt} \quad (3.27)$$

$$\sqrt{T^2 - (mg)^2} - \frac{\rho}{2} C_D A_{eff} v^2 = m \frac{dv}{dt} \quad (3.28)$$

For calculating the maximum speed of a UAV, the limit speed should be considered. Using the limit speed, both maximum values of vertical climb speed and horizontal flight speed (3.29) can be calculated. For vertical flight T_{vertical} will be equal to the total thrust:

$$\frac{T}{m} g - \frac{\rho}{2m} C_D A_{eff} v^2 = 0 \quad (3.29)$$

For the maximum pitch angle of a UAV inverse sine function should be considered related to the weight and thrust of the vehicle (3.30):

$$\alpha = \arcsin\left(\frac{mg}{T}\right) \quad (3.30)$$

For horizontal flight, the resultant force of the total thrust force and gravitational force can be used because the vehicle's total thrust force must exceed both horizontal (gravity) and vertical (air drag) forces will be equal to total thrust (3.31):

$$\frac{\sqrt{T^2 - (mg)^2}}{m} - \frac{\rho}{2m} C_D A_{eff} v^2 = 0 \quad (3.31)$$

In order to approximate flight duration for a constant total weight, the relationship between battery weight and payload (Eqn. 3.32) an equation composed. It is assumed Voltage is constant for this situation with a fixed angular velocity of the propeller.

$$Df = \frac{Cp \times Cs}{DcH} \times 60 \quad (3.32)$$

where: Flight duration: Df (min), Cells in Parallel: Cp, Storage Capacity of the Battery: Cs (A), Discharge needed for Hovering: DcH (A).

3.4.6 Strain Measurement

In order to investigate maximum strain on VTOL UAV arm FEA results is correlated by using a force transducer. Maximum strain location is shown in Fig 3.69 according to the FEA results. For different force inputs strain output is recorded using FEA results.

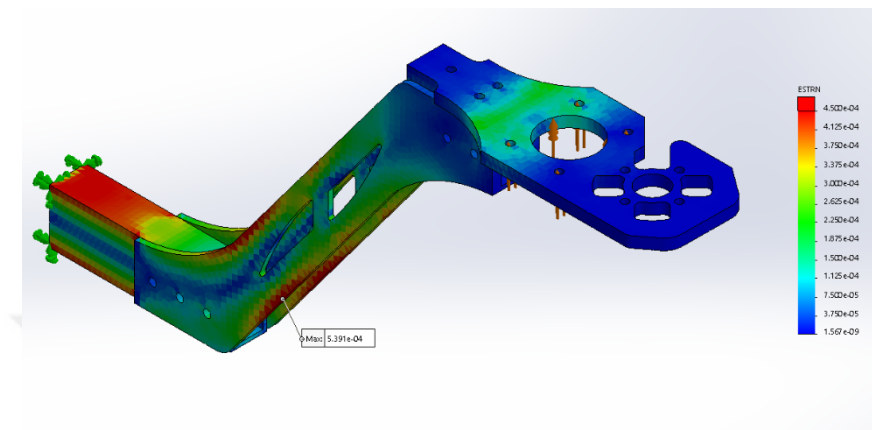


Fig. 3.69. Maximum Strain on the VTOL UAV arm (isometric view).

An averaged output (Fig. 3.70) result acquired from maximum strain location that recorded from every analysis.

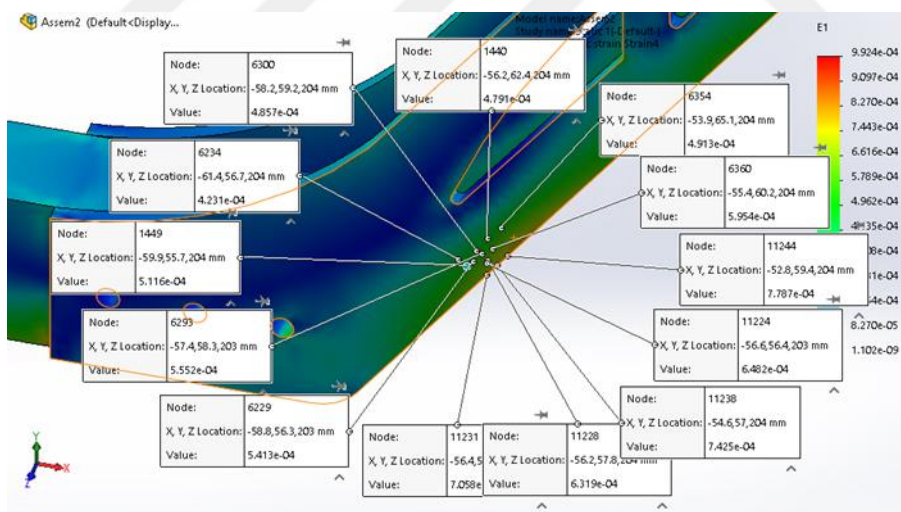


Fig. 3.70. Maximum Strain on the VTOL UAV arm.

In the experimental stage, for determining the force strain relationship a rosette type strain gage attached to the arm. A force transducer is used for this duty which is a type of transducer for converting force into an electrical signal. Force transducer usually consists of strain gauges in a Wheatstone bridge configuration. Those transducers are commonly used in industrial applications for sensing loads. In this step, a force transducer and a force measurement system have been used to measure

force variations on VTOL UAV Arm. Fig. 3.71 shows the layout of strain gauges on the arm of UAV.

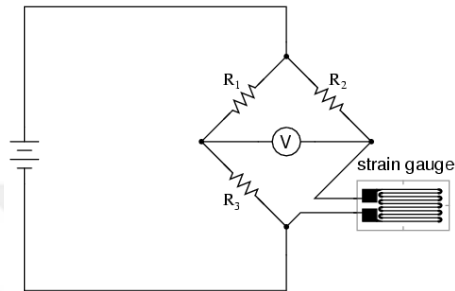


Fig. 3.71. Bridge on VTOL UAV Arm.

The developed system has a quarter bridge strain gauge layout on the VTOL UAV arm. In order to measure shear strain rosette type strain gauge (Fig. 3.72) is used. 5V excitation voltage used for supplying bridges and resistance of strain gauges is 360Ω.



Fig. 3.72. Rosette type strain gauge layout.

The resistance of a material is related to the type of material and its volume (Eqn. 3.33).

$$R = \frac{\rho \cdot L}{S} \quad (3.33)$$

where: R: Resistance (Ω), ρ: Resistivity, L: Length (m), S: Cross-sectional area.

Strain variances can be calculated by measuring the resistance difference (Eqn. 3.34).

$$\Delta R = GF \cdot \epsilon \cdot R \quad (3.34)$$

where: ΔR : Resistance difference (Ω), GF : Gage factor, ϵ : Strain, R : Resistance (Ω).

The output can be evaluated by using the Wheatstone bridge as a voltage difference (3.35).

$$V_o = V_{ex} \left[\frac{R_1}{R_1 + R_2} - \frac{R_3}{R_3 + R_G} \right] \quad (3.35)$$

The block diagram of the strain measurement system is shown in Fig. 3.73.

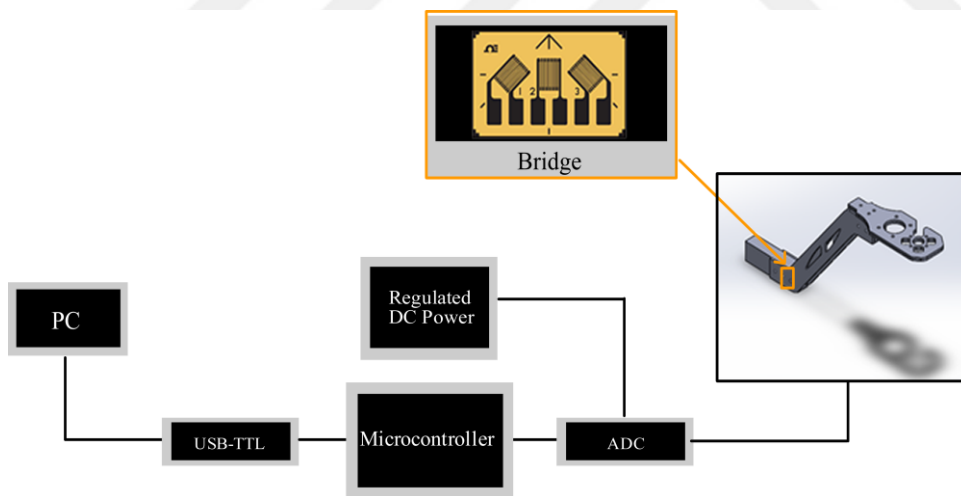
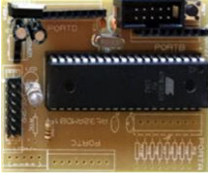


Fig. 3.73. Block diagram of the strain measurement system.

Table 3.7. Electronic components used for data acquisition and their descriptions.

Electronic Unit	Model	Figure	Description
Microprocessor	At32MDB01		Custom design development board used for data acquiring.
ADC	HX711 Module		24-Bit Analog-to-Digital Converter (ADC) for Weigh Scales
USB to serial UART interface	FT232RL FTDI		USB to serial UART interface

In order to get strain values from the VTOL UAV arm, regulated DC power sources used for supplying bridge on the arm. Analog signal generated on bridges is acquired with 24-bit ADCs. Signals are converted to digital by the ADC and output is transferred to a PC via serial communication by the microcontroller. In order to decrease noise on the bridge, a regulated DC power source is used to supply the Wheatstone bridge. Equipments are used in this stage is shown in Table 3.6. In addition, for this purpose cable shields is connected to the ground as shown in Fig. 3.74.

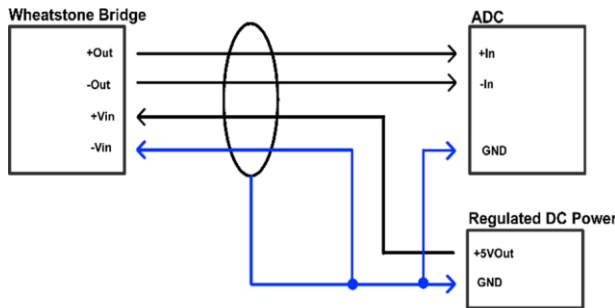


Fig. 3.74. Shield Grounding for Noise Reduction

The bridge on the VTOL UAV arm is shown in Fig. 3.75.

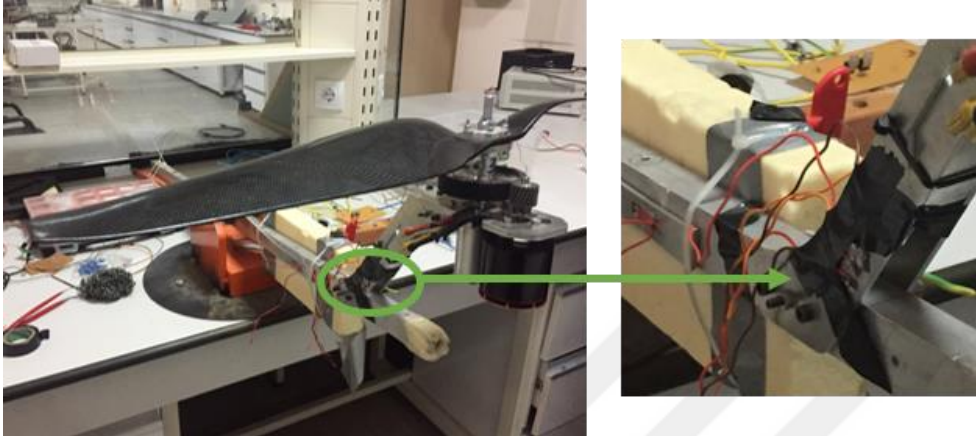


Fig. 3.75. The bridge on the VTOL UAV Arm.

In order to convert digital outputs of the ADC from digital value to voltage value formula 3.36, 3.37 and 3.38 are used.

$$V_{in} = \text{ADC Digital Output} \times \text{ADC Step Response} \quad (3.36)$$

where; V_{in} : ADC input voltage, LSB: Least Significant Bit

$$\text{ADC Step Response} \left(\frac{V}{\text{digital output}} \right) = \frac{FSR}{2^n} \quad (3.37)$$

$$FSR = \frac{V_{ex}}{\text{Gain}} \quad (3.38)$$

Voltage to strain relationship can be determined with the Wheatstone bridge formula as shown in Eqn. 3.39 and Eqn. 3.40.

$$\Delta R_4 = R + \left(R_3 - \left(\frac{R_3}{\frac{R_1}{R_1 + R_2} - \frac{V_o}{V_{in}}} \right) \right) \quad (3.39)$$

$$\varepsilon = \frac{\Delta R}{GFxR} \quad (3.40)$$

Acquired strain results from the experimental study are shown in Figure 3.76 (ε_a for X-axis), 3.77 (ε_b for Y-axis), 3.78 (ε_{ab} for XY axes).

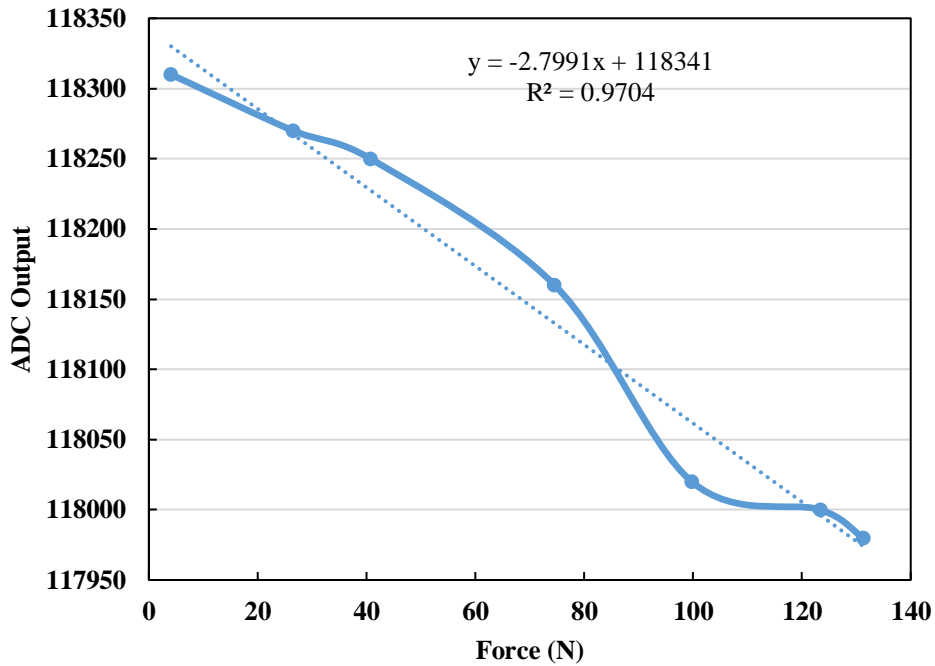


Fig. 3.76. Strain on the X axis.

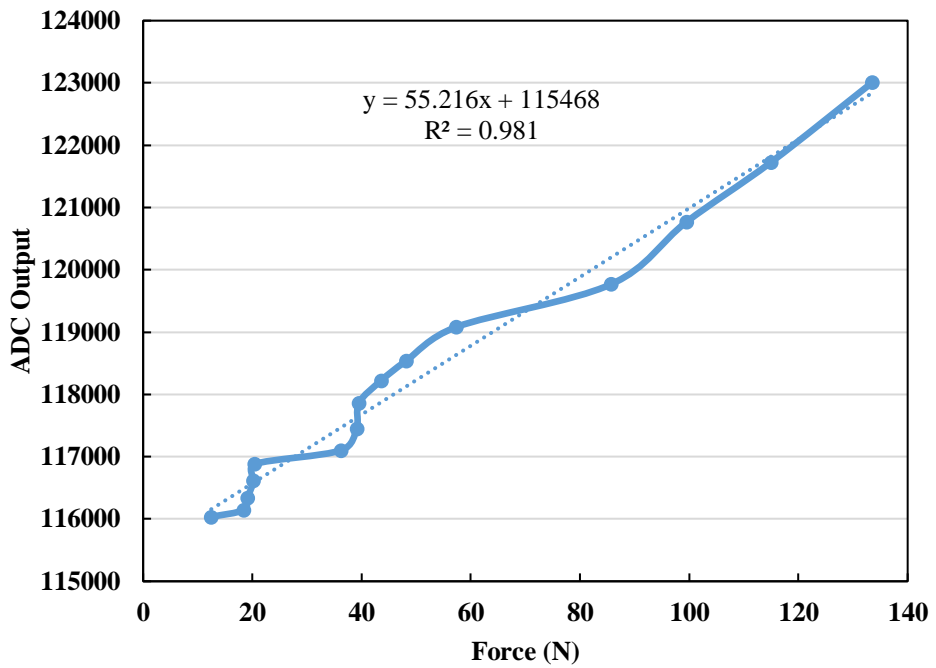


Fig. 3.77. Strain on the Y axis.

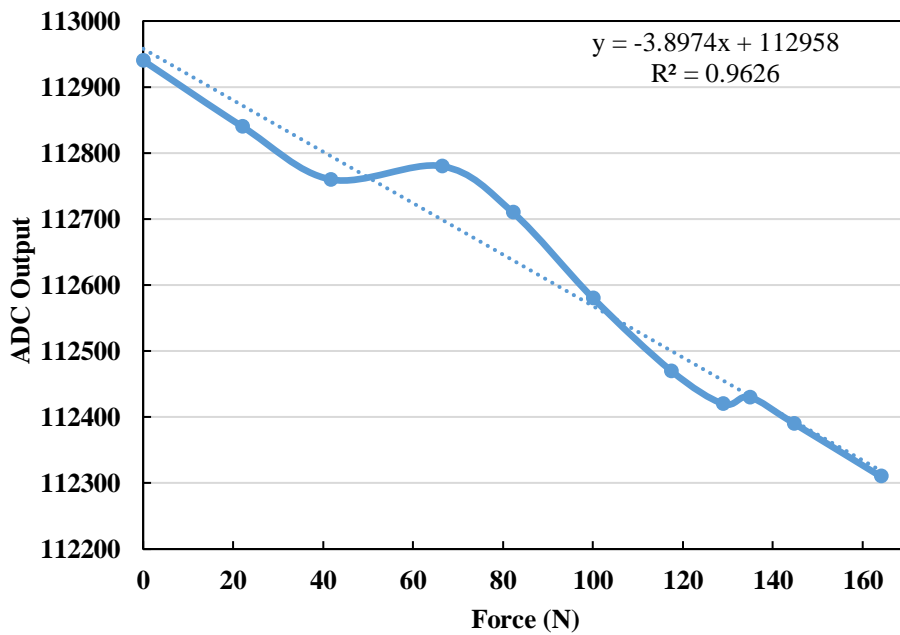


Fig. 3.78. Strain on the XY axis.

Average results calculated using slope formula from the strain results for Avg (ϵ_a) = -21.7111, Avg (ϵ_b) = -17.0539, Avg (ϵ_c) = 11.6556.

Coordinate transformation equation denoted in Eqn. (3.41-3.43).

$$\epsilon_a = \frac{\epsilon_x + \epsilon_y}{2} + \frac{\epsilon_x - \epsilon_y}{2} \cos 2a + \epsilon_{xy} \sin 2a \quad (3.41)$$

$$\epsilon_b = \frac{\epsilon_x + \epsilon_y}{2} + \frac{\epsilon_x - \epsilon_y}{2} \cos 2(a + \beta) + \epsilon_{xy} \sin 2(a + \beta) \quad (3.42)$$

$$\epsilon_c = \frac{\epsilon_x + \epsilon_y}{2} + \frac{\epsilon_x - \epsilon_y}{2} \cos 2(a + \beta + \gamma) + \epsilon_{xy} \sin 2(a + \beta + \gamma) \quad (3.43)$$

3.4.7 Other Parts

In the field, aerial sprayers flying time and lifting capability are key elements that affect the size of the spraying area. It is directly related to weight of an aerial vehicle and battery power. To obtain a long flying time from a UAV, Lithium Polymer (Li-Po) battery with BLDC motors are used because of their size and effectiveness.

Main Gear Analysis conducted in order to produce the main gear (Fig. 3.79) by using 3D printer for decreasing the costs (Fig 3.80). The UAV motor has a gear reducer that combined from a steel pinion gear with 20 teeth and a carbon-reinforced nylon main gear with 68 teeth. For FEA the center of the gear is fixed and the torque applied to a tooth of the gear in CCW direction. The reduction ratio is 20/68 and the maximum stress conditions are investigated using SolidWorks Simulation software. 3D drawing of the gear is shown in Fig 3.81.



Fig. 3.79. Main Gear



Fig. 3.80. Main gear tensile tests.

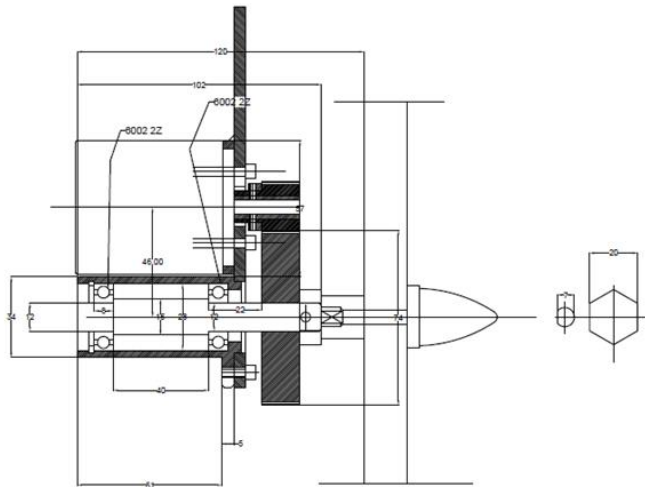


Fig. 3.81. Cross-section view of the designed gear reducer (draft for manufacturing).

3.4.7.1 Power Distribution Board

Typically, copper material used in PDBs for providing high current flow with low resistance. For ground vehicles or stationary devices, this is ideal but for aerial vehicles, weight is a very important parameter because of flying limitations with high loads. When masses are the same with aluminum and copper, the resistance of copper is low so current flow is better but when the weights are the same for these two materials, aluminum provides more than 2 times the current flow. Aluminum is a good option for aerial vehicles because of its lightweight structure indicated in Table 3.7 and it is a low-cost solution as shown in Table 3.8.

Table 3.8. Material properties of pure Copper and Aluminum (Meulenbroeks, 2014).

Material property	Unit	Copper	Aluminum
Density (@20°C)	g·cm ⁻³	8.94	2.70
Electrical resistivity (@20°C)	nΩ·m	16.78	28.2
Thermal expansion (@25°C)	μm·m ⁻¹ ·K ⁻¹	16.5	23.1
Ultimate tensile strength	MPa	380	200

Table 3.9. Market price properties of pure Copper and Aluminum (Meulenbroeks, 2014).

Material property	Copper	Aluminum
Market price raw materials (2014)	3	1
Weight	3	1
Resistivity per volume	3	5
Cost per Ampere	6	1

The electrical resistivity of a material is defined in terms of the magnitude of the electric field across it that gives a certain current density (Eqn. 3.44).

$$\rho = \frac{E}{J} \quad (3.44)$$

where:

- ρ is the resistivity of the material in ohm meters, Ω·m
- E is the magnitude of the electric field in volts per meter, V·m⁻¹
- J is the magnitude of the current density in amperes per square meter, A·m²

In general, manufactured resistors and conductors have a cross-sectional uniformity and permits uniform flow of electric current. For this reason, it is possible to compose the more specific in Eqn. (3.45):

$$\rho = R \times \frac{A}{l} \quad (3.45)$$

where:

- R is the electrical resistance of a uniform specimen of the material measured in ohms
- l is the length of the piece of material measured in meters, m
- A is the cross-sectional area of the specimen measured in square meters, m²
(Anonymous , 2018).

The Electrical resistivity ratio per volume of copper compared to aluminum is 3 to 5. Consequently, an aluminum conductor volume is to be increased by 68% in order to obtain equal resistivity to copper. Therefore, aluminum conductors have larger cross-sections for equal current carrying capacity (Meulenbroeks, 2014).

Copper and aluminum's density relate to 3:1, implying that copper is about three times heavier than the equal volume of aluminum. However, when the weight ratio is related to the electrical resistivity, the balance tips in favor of aluminum: the resistivity ratio per mass of copper compared to aluminum is 2 to 1. This implies that per kg, aluminum is two times better conductor than copper (Meulenbroeks, 2014).

In order to decrease the weight of the UAV an aluminum PDB is designed and developed. The schematic of the PDB is shown in Fig. 3.82.

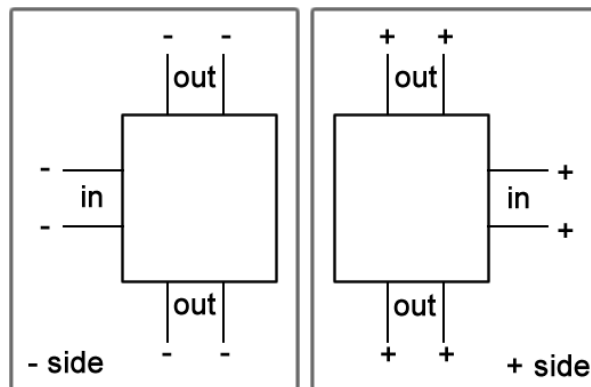


Fig. 3.82. Schematic of the PDB.

3.4.8 Specifications of the UAV

The most important specifications of the UAV is listed in Table 3.9.

Table 3.10. Specifications of the UAV.

Specification	Description
The VTOL UAV	
Total Weight (without battery) (kg)	11.96
Max Takeoff Weight (kg)	64
Payload(kg)	20
Operating Speed (km/h)	12
Dimensions (Length, Width, Height (mm))	1326x900x750
Hover time (min)	46.34 (@ with 10 kg takeoff weight)
Max Cont. Power (KW)	18.40
Power source	Electric
Practical range	400 m
Cost (\$)	3,000.00

3.4.9 Flight Tests

Positioning accuracy plays an important role for spraying target plants in spraying applications. For testing the positioning accuracy of UAVs, a small-scale UAV is developed. Positioning accuracy tests are implemented autonomously using predetermined target coordinates. (Fig. 3.83).

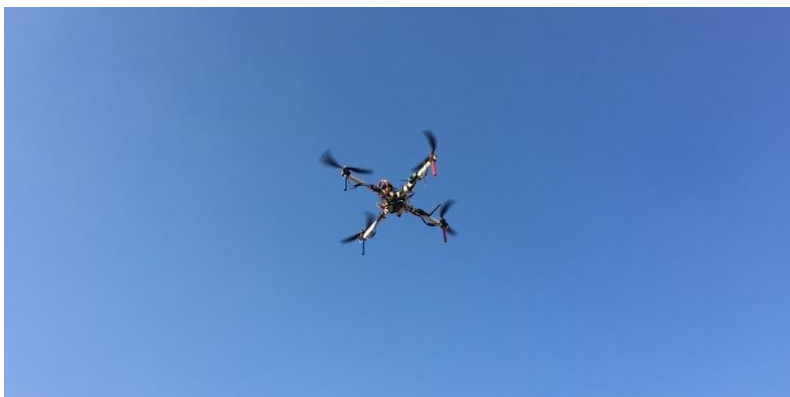


Fig. 3.83. The small UAV.

A square path (Fig .3.84) including four waypoints, an S-line path (Fig. 3.85) with 17 waypoints and a Z-line, which includes a 4-waypoint path, are investigated. Flight logs are used to measure the deviation of the small UAV. Fig 3.84 (a) shows a determined target path with yellow lines and Fig 3.84 (b) shows the UAV flight path using purple lines. Green bubbles indicate the target coordinates in Flight log figures.

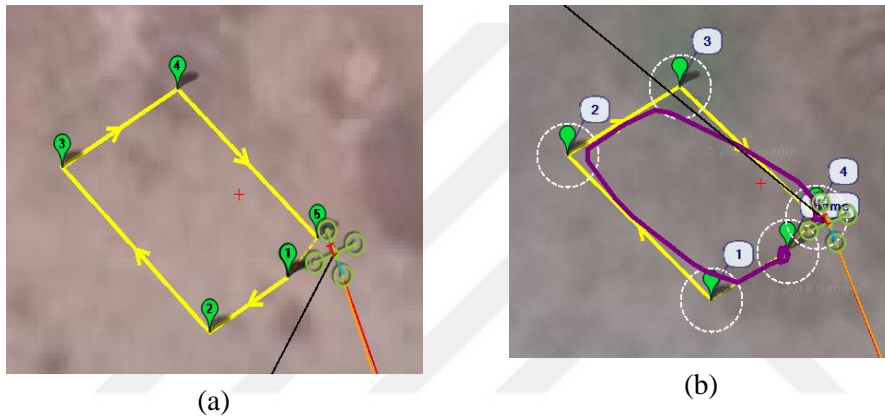


Fig. 3.84. Flight logs for Square path.

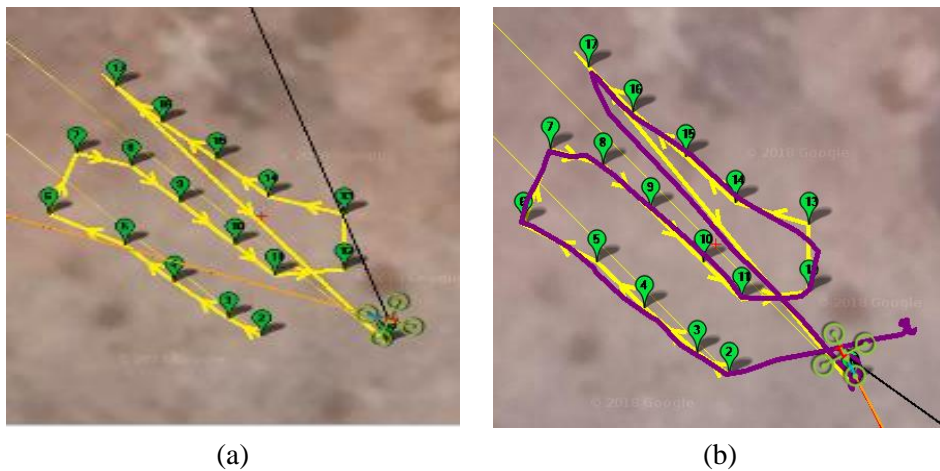


Fig. 3.85. Flight logs for S-line path.

The haversine formula is used to convert flight coordinates to meters. This equation is significant for navigation applications in order to provide circular distances between two coordinates on the earth by using longitudes and latitudes of them.

$$A = \frac{Lat_1 - Lat_2}{2} \quad (3.45)$$

$$B = \frac{Long_1 - Long_2}{2} \quad (3.46)$$

$$d = 2 \cdot R \cdot \arcsin \left\{ \sqrt{\sin^2(A) + \cos(Lat_1) \cdot \cos(Lat_2) \cdot \sin^2(B)} \right\} \quad (3.47)$$

where: Lat: latitude, Long: longitude, R is radius of earth (radius = 6,371km).

Each flight repeated for three times and 25 different target points are analysed. In total 75 points are investigated in order to obtain RMSE values for autonomous GPS guided flight accuracy. An image of the small UAV in the test field is shown in Fig. 3.86.



Fig. 3.86. The small UAV in the test field.

The target coordinates used in field tests are shown in Table 3.10 for S-line path and Table 3.11 for square path and Table 3.12 for Z-line path.

Table 3.11. S-line path target coordinates.

Target Coordinate Latitude	Target Coordinate Longitude
37.8580859	27.8570551
37.8580980	27.8570342

37.8581184	27.8569993
37.8581447	27.8569708
37.8581639	27.8569226
37.8582003	27.8569405
37.8581912	27.8569747
37.8581683	27.8570049
37.8581447	27.8570391
37.8581239	27.8570634
37.8581283	27.8571067
37.8581600	27.8571062
37.8581743	27.8570594
37.8581986	27.8570276
37.8582200	27.8569929
37.8582412	27.8569641

Table 3.12. Square path target coordinates.

Target Coordinate Latitude	Target Coordinate Longitude
37.858117	27.8570720
37.858195	27.8569670
37.858234	27.8570470
37.858162	27.8571470

Table 3.13. Z-line path target coordinates.

Target Coordinate Latitude	Target Coordinate Longitude
37.8581361	27.8571251
37.8581859	27.8571063
37.8581679	27.8570420
37.8582272	27.8570151

3.5 Spraying Unit –Sprayer and Tank

The spraying unit is consisting of a tank, a boom and four nozzles mounted on it as shown in Fig. 3.87. The tank has 7.3-liter pesticide storage capacity. A thermoset material used in the tank for decreasing the free-surface effect.

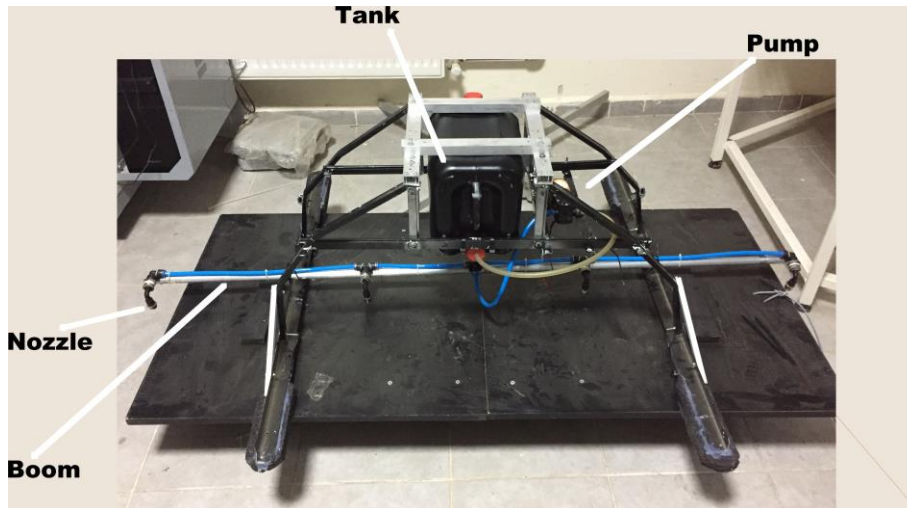


Fig. 3.87. The spraying unit.

The layout of the spraying mechanism is shown in Fig. 3.88 and properties are listed for the sprayer in Table 3.13.

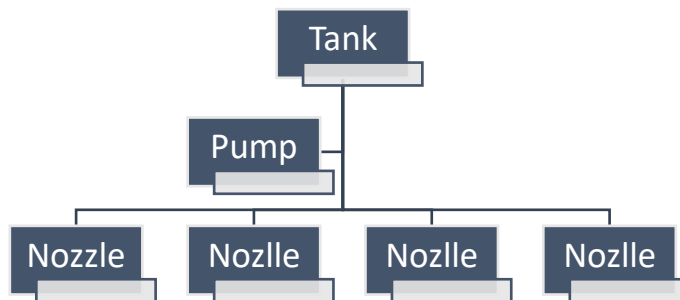


Fig. 3.88. Sprayer units and layout.

Table 3.14. Sprayer properties.

Specification	Description / Value
Material	Aluminum alloy
Weight (g)	1650
Tank Capacity (mL)	7350
Spraying Speed (L/min)	2.17
Voltage (V)	12
Nozzle Count	4 pieces
Spraying Rod Width (mm)	1500

For aerial applications, Center of Gravity (CG) is very important for stabilized flight. The free surfaces of a tank mounted under UAV effects the CG. In order to decrease the disturbance effect a sponge of thermoset material used in the tank. This material is a kind of sponges and it decreases above 95% percent free space in the tank. It influences the suction of pump (pressure) and increases weight about 26%. The inner structure of a sponge shown in Fig. 3.89.

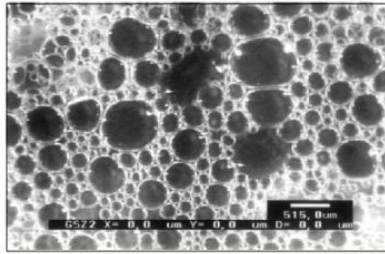


Fig. 3.89. SEM image of a sponge (Wu et al., 2015).

In order to reduce the effect of Center of Gravity from the spraying tank a sponge filled in it. A tank with sponge and without sponge compared (Fig. 3.90) by considering volume flow rate and pressure difference.



Fig. 3.90. Image of the tank with and without the foam.

Nozzle is not an expensive part of a spraying system but its tip is one of the most important parts. A nozzle in a spraying system performs four basic functions: atomizing liquid into droplets, dispersing the droplets in a specific pattern, metering the liquid at a certain flow rate and providing hydraulic momentum. For pesticide spraying, selecting a proper spray nozzle is very important part of these applications.

For this study, a full-cone (Fig. 3.91) nozzle was chosen and the distance was determined according to governmental pesticide spraying suggestions. The space between nozzles is set to 50 cm. These nozzles are used primarily where plant foliage penetration is essential for effective insect and disease control, and where drift is not a major consideration. It is adequate for pressures close to 4-40 PSI and provides a good spray pattern.



Fig. 3.91. Full-cone nozzle.

Spraying area and UAV positioning relationship is calculated using basic trigonometric functions (Fig. 3.92).

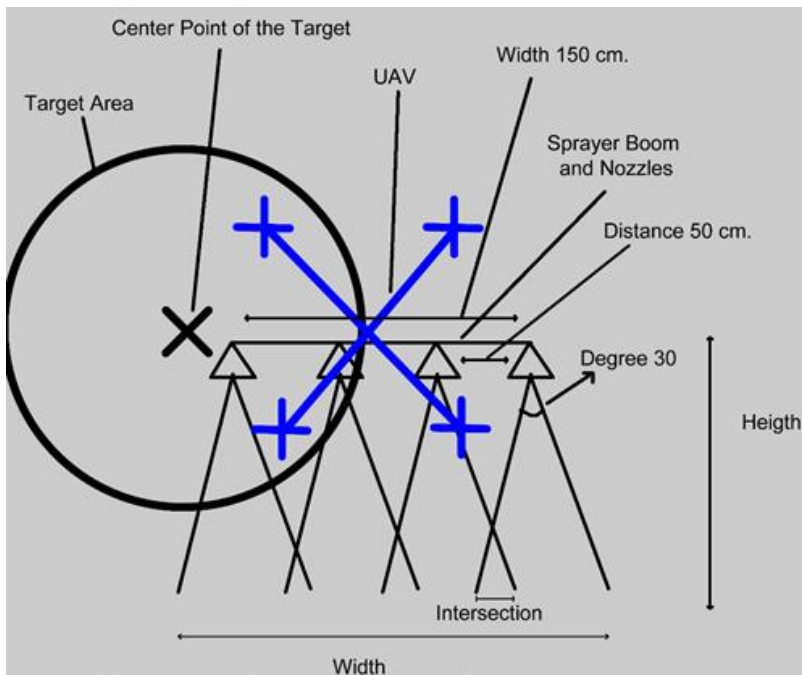


Fig. 3.92. Spraying area calculation.

4. RESULTS AND DISCUSSION

It is a known fact that plant diseases are one of the main problems of crop yields. Mostly conventional spraying methods are used to solve this difficult problem by spraying pesticides on plants, which includes harmful chemicals for the environment. It is obvious from years of experience, using a conventional method for agricultural pest control reduces the efficiency of crops by spraying applications. Mostly, these methods are not proper for precision farming applications because it affects soil, plants and their roots.

Considering the lack of conventional methods, in this thesis, it is aimed to develop a selective aerial pesticide sprayer vehicle that uses less chemicals with more efficiency for spraying plants than commonly used traditional methods. In this study, a ground assisted aerial sprayer system is developed in order to reduce the harmful effects of spraying applications on plants. For this purpose, a selective spraying method are composed which includes the development of a sprayer unit with a UAV and a UGV with a multispectral camera. The sprayer UAV is developed for accomplishing spraying duty. The UGV and the multispectral camera was developed for determining the locations of diseased plants in a target crop field. A GCS is used for coordination between these units in order to reduce spraying time and chemical usage.

4.1 The UGV

In order to develop a vehicle that adequates for difficult terrains, a four-wheel powered UGV is implemented using the skid steer driving method. For this purpose, UGV chassis, motor holders and hubs are analyzed using FEM. The developed UGV is shown in Fig. 4.1.



Fig. 4.1. The UGV.

Structural analysis results for the chassis of the UGV under 400N force indicates that FoS value is above 12 and the detailed result shown in Fig 4.2.

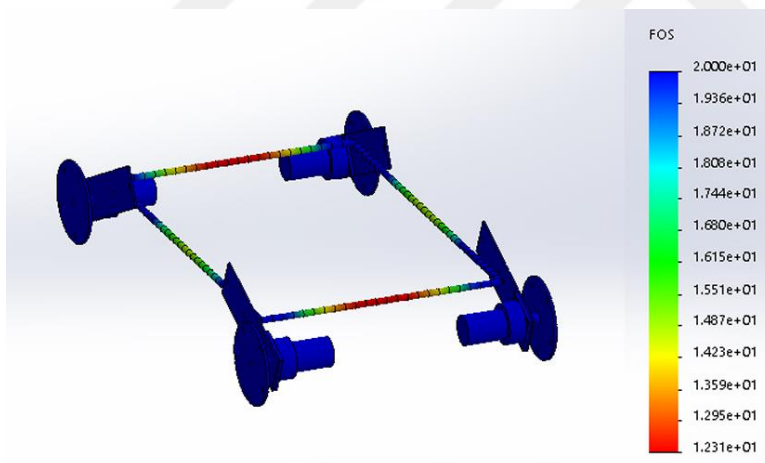


Fig. 4.2. FEA result of the UGV.

Flanged coupler structural analysis indicates that FoS is over 4.5 for calculated maximum torque value (Fig. 4.3).

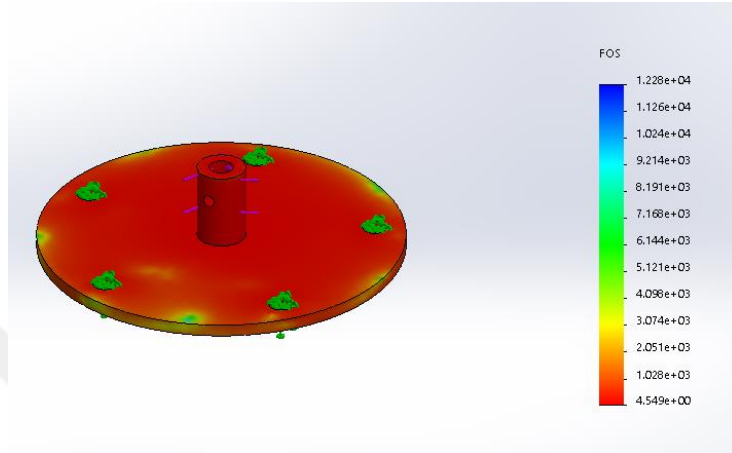


Fig. 4.3. Structural static analysis for the flanged coupler of the UGV.

According to the results of the theoretical calculations, with 5 kg payload for 10° maximum slope cruising distance is 6.4 km for an hour.

4.2 The Multispectral Camera

In the plant disease detecting and locating step, a custom-designed multispectral camera is developed and a GPS module is integrated into it for achieving disease locating goal. For this purpose, the disease detecting unit alternately scans lines in the targeted field for acquiring NDVI value and transfers each data to the base station that includes coordinate information of the scanned line. This unit is mounted on the arm of the UGV by using a gimbal for reducing vibration on it. This locomotion UGV provides mobility and it has the ability to scan a field row by row.



Fig. 4.4. The multispectral camera (Spekra TSL128-RN).

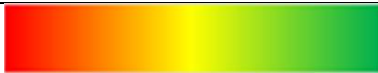
The plant disease detecting tests implemented using planter plants for indoor and outdoor using the multispectral camera that shown in Fig 4.4. NDVI measurement results for the Spektra TSL128-RN and the PlantPen NDVI 300- NDVI is investigated. Table 4.1 shows average results for four different plant species using PlantPen NDVI device.

Table 4.1. PlantPen 300 NDVI device test results.

Plant Status	NDVI Output	Scalded to 0-1
Healthy	70	0.7
Semi healthy	25-40	0.25-0.4
Older	Under 10 close to 0	<0.1
Diseased	Between 10-20	0.1-0.2

Field tests using the Multispectral Camera are implemented for both indoor and outdoor and results are shown by gradient colors as indicated in Table 4.2. NDVI results were recorded for healthy grass and fig tree leaves. Results show that it is possible to differentiate grass from leaf and healthy fig leaf from older fig leaf by using the multispectral camera in the field test.

Table 4.2. Color gradient for spectral bands.

Gradient Color Scale	Format	Applies to
0 to 1023		NIR Band Data
0 to 1023		Red Band Data
-1 to +1		NDVI Output

For each test, Red and NIR bands are recorded and NDVI values are calculated. The test results for grass (Fig. 4.4) shown in Fig 4.5 (a) for the Red band, Fig. 4.5 (b) for the NIR band and Fig. 4.6 for NDVI output in gradient color scale.

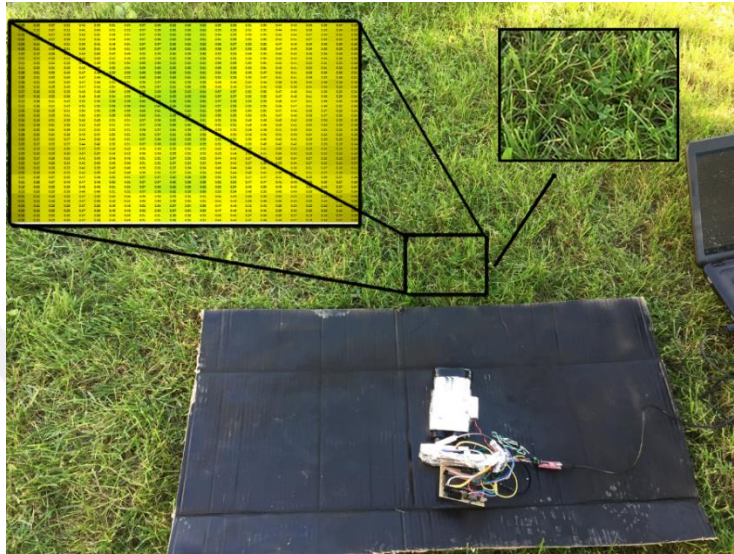


Fig. 4.5. Image from the NDVI measurement for grass.

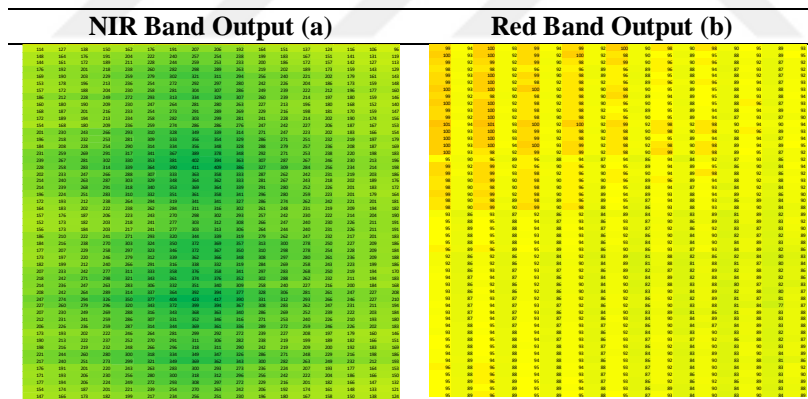


Fig. 4.6. NIR and Red band outputs of the grass from the Spektra TSL128-RN.

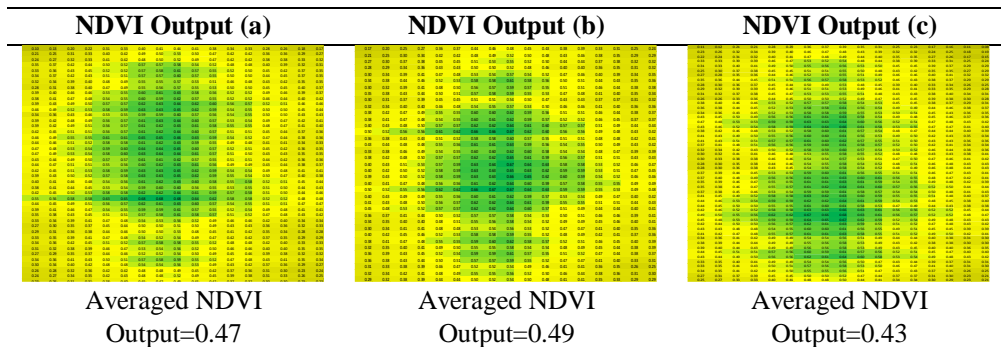


Fig. 4.7. NDVI outputs of the grass from the Multispectral camera.

For fig tree leaves, test steps are implemented by using rows as listed in Table 4.3. and the results are shown in Fig. 4.7.

Table 4.3. Scanning sequence of the Spektra TSL128-RN.

Steps	Steps in the image	Image of the test field
1	Black	
2	Grass	
3	Healthy leaf	
4	Grass	
5	Dead leaf	
6	Grass	
7	Healthy leaf	
8	Grass	
9	Dead leaf	
10	Grass	

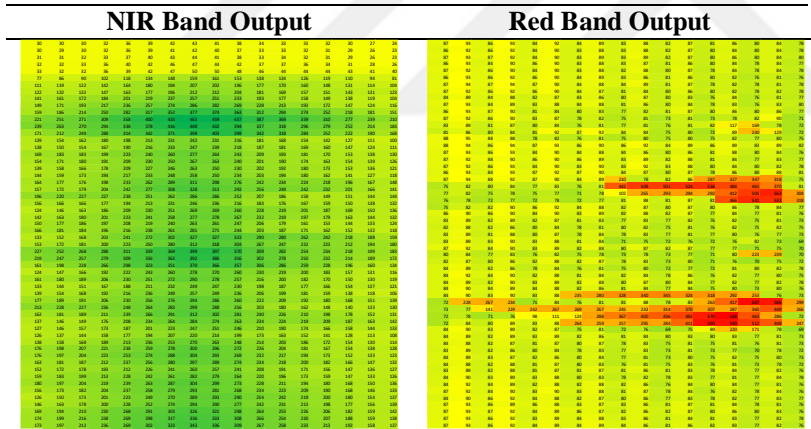


Fig. 4.8. NIR and Red band outputs of fig tree leaves from the Spektra TSL128-RN.

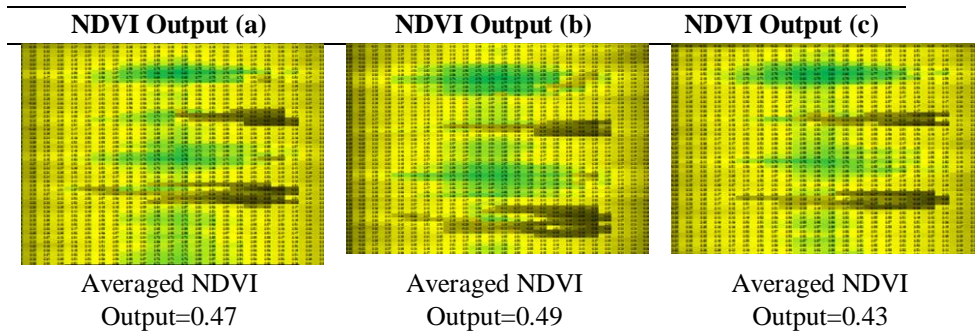


Fig. 4.9. NDVI outputs of fig tree leaves from the Spektra TSL128-RN.

Table 4.4. Multispectral Camera outdoor field test results.

Leaf Id	Averaged NDVI Results		
	(a)	(b)	(c)
1 (Healthy)	0.61	0.63	0.65
2 (Older)	0.26	0.37	0.36
3 (Healthy)	0.61	0.64	0.61
4 (Older)	0.07	0.18	0.22

Indoor tests are implemented using Planetree leaves a semi-healthy and healthy leaf (Fig. 4.9) are investigated under a multispectral camera using daylight illumination.



Fig. 4.10. Planetree leaves for NDVI measurement.

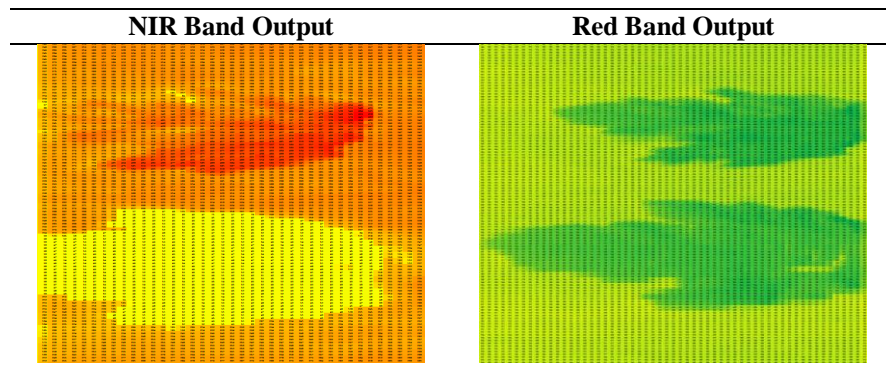


Fig. 4.11. NIR and Red band output of Planetree leaves from the Multispectral Camera.

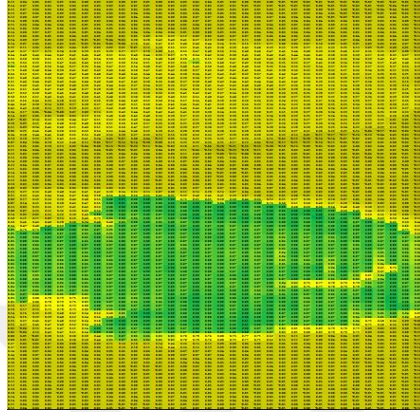


Fig. 4.12. NDVI output of Planetree leaves from the Multispectral Camera.

The measurement results for the healthy and diseased plane tree leaves are shown in Table 4.5.

Table 4.5. Spektra TSL128-RN indoor test results.

Plant Status	NDVI Output (Avg.)
Healthy Leaf	0.77-0.83
Diseased Leaf	0.36-0.47

Test results show that it is possible to use NDVI output of leaves and grasses for differentiating from each other by a multispectral camera that uses NIR and Red band in the electromagnetic spectrum.



Fig. 4.13. Plant disease detection test.

Using this custom-designed multispectral camera, plant disease detection tests are implemented (Fig. 4.13). In plant disease detecting tests, fig tree leaves are used and three different statuses are investigated. Mainly these it is aimed to classify the leaves by their healthy, semi-healthy and disease statuses. The leaves used in this test is shown in Fig. 4.14 (a), Fig. 4.14 (b) and Fig. 4.14 (c).

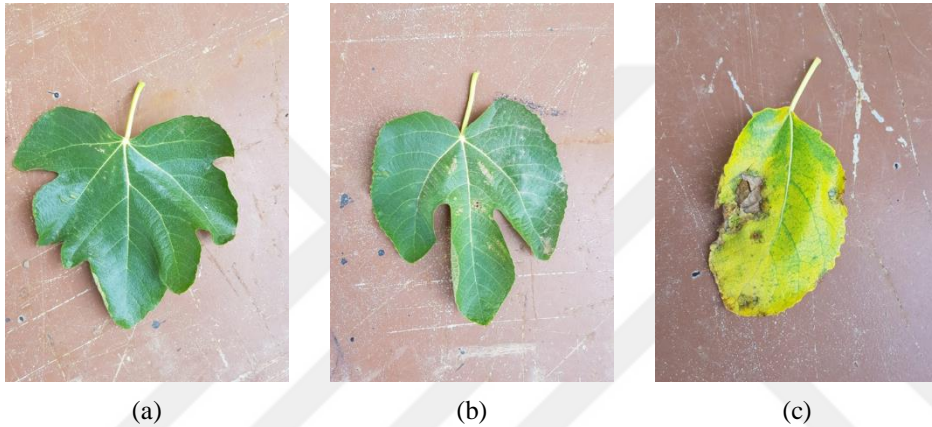


Fig. 4.14. Test leaves for plant disease detection.

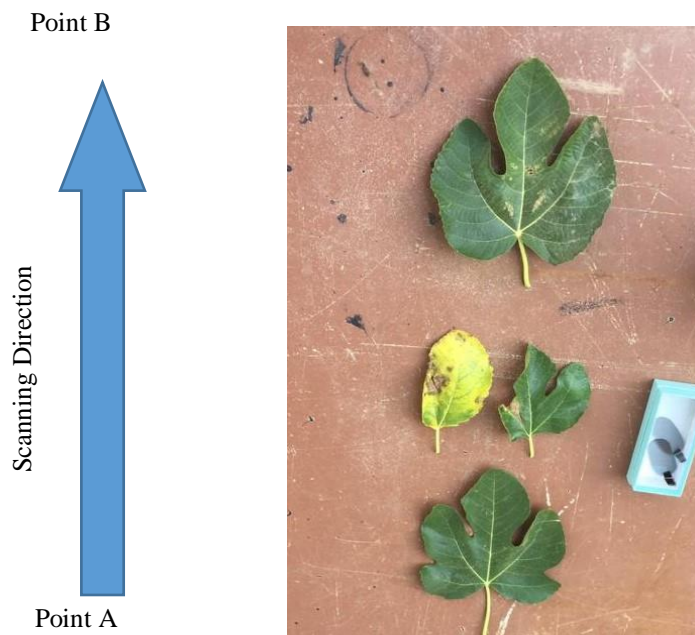


Fig. 4.15. Scanning process and direction.

Scanning height is 1 meter above from the leaves (Fig. 4.15) and the line scanner is moved at 0.3 m/s for throughout the plants and it is repeated 10 times. Spectral imaging results of the test leaves shown in Fig. 4.16.



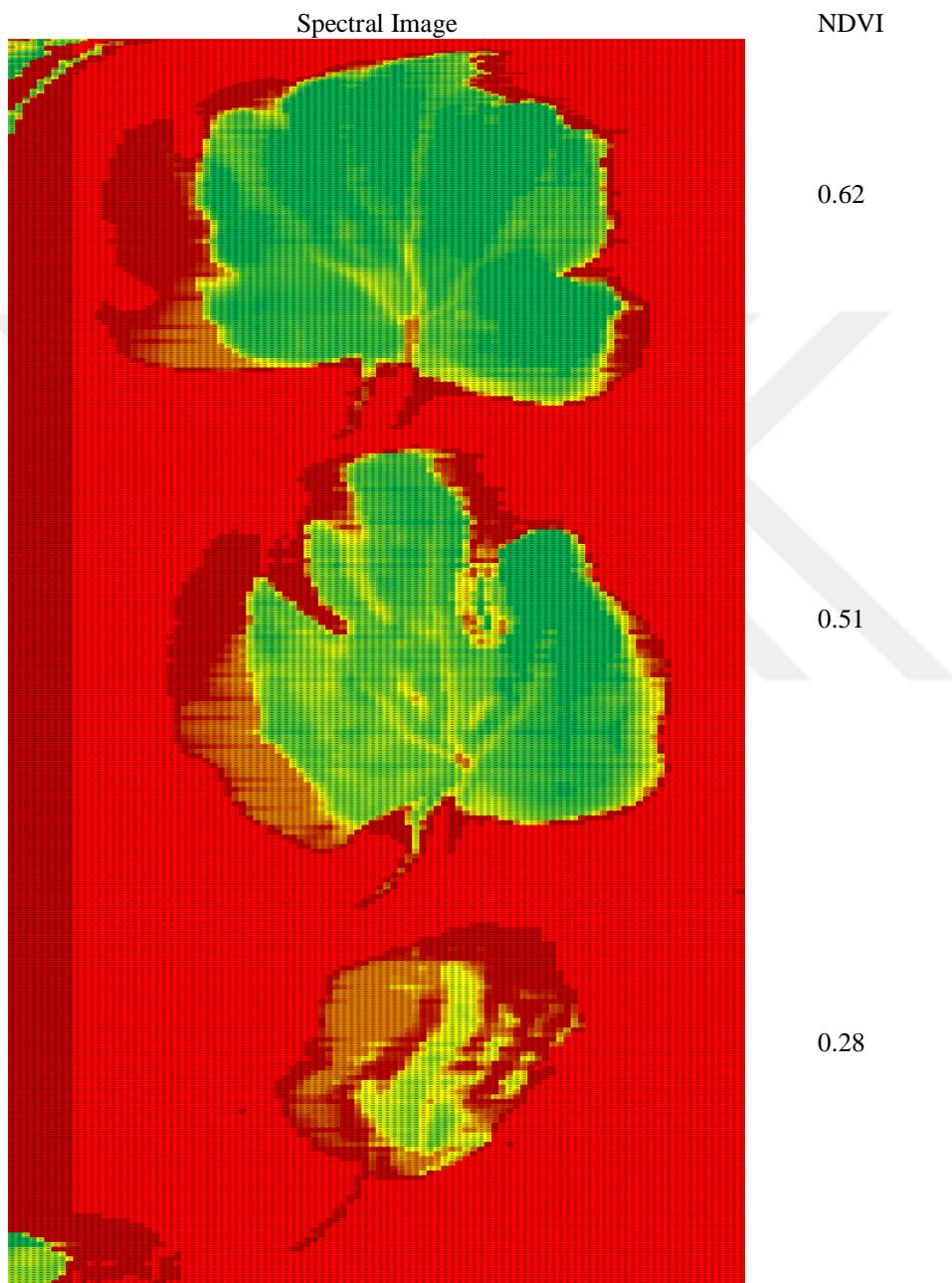


Fig. 4.16. NDVI results for three scanned leaves.

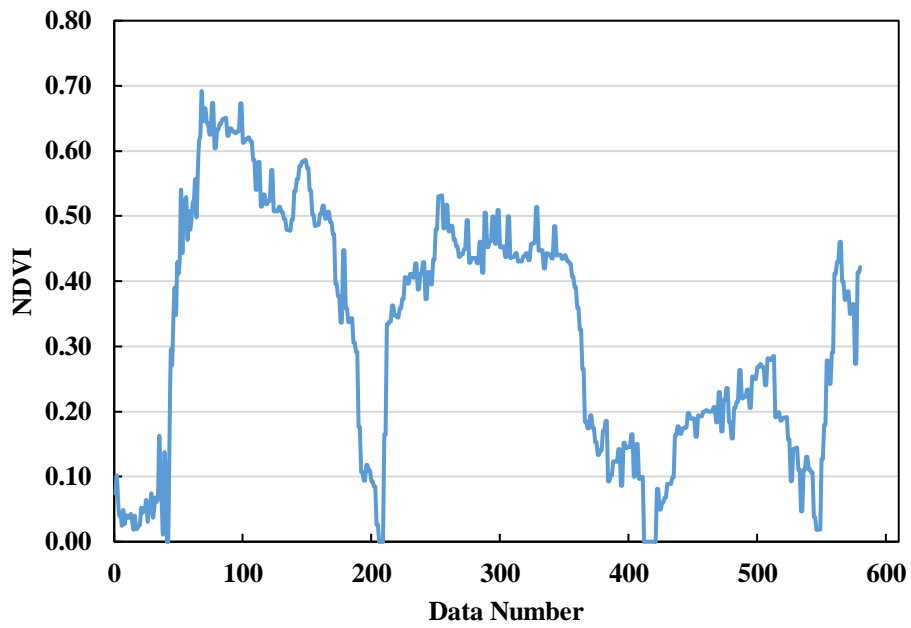


Fig. 4.17. NDVI result chart for three scanned leaves.

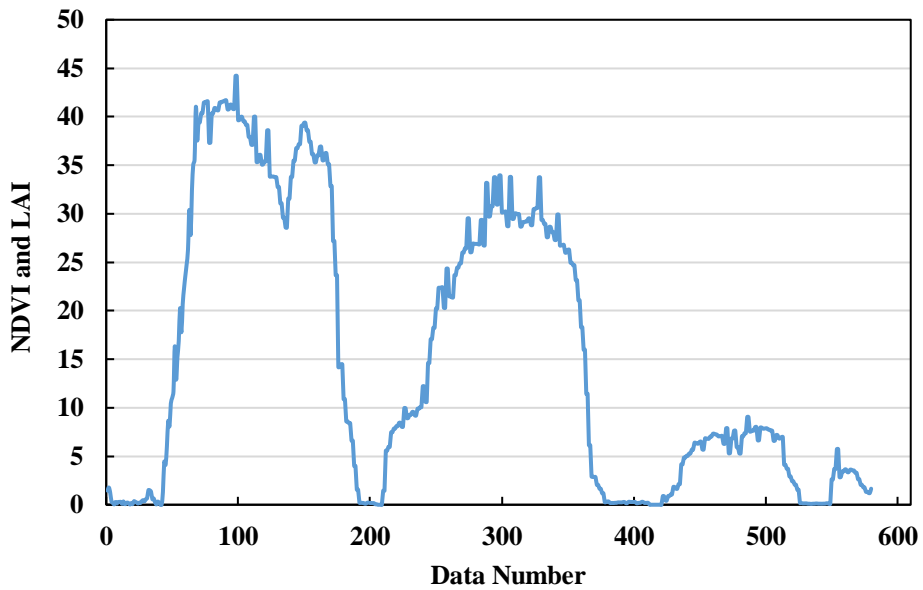


Fig. 4.18. NDVI and LAI composed result chart for three scanned leaves.

As it understood from the NDVI result shown in Fig. 4.17, it is possible to detect diseased part on a leaf. In addition, for spraying processes the size of a leaf should be considered by focusing the Leaf Area Index (LAI) as indicated in Fig. 4.18 in order to determine the coverage of a diseased area.

4.3 The UAV

In order to achieve the lack of low cost Mid-Size agricultural spraying UAV production, in this thesis a VTOL (Vertical Take-off and Landing) UAV designed, analyzed, developed and experimented using a testing mechanism. A well-structured, lightweight and high strength aluminum chassis developed to use for Mid-Size UAVs and it is suitable for mass production. The manufactured VTOL UAV's image is shown in Fig. 4.19.



Fig. 4.19. Manufactured VTOL UAV.

It is suitable to lift up to 40 kg payload with 4.3 Factor of Safety (FoS) and other parameters obtained from the analysis are shown in Table 4.6. It is a low-cost solution and modifiable when compared to common carbon fiber frames in markets.

Table 4.6. FEA analysis result of the VTOL UAV chassis.

FEA Analysis Results	Value
Maximum value for Von-Misses Stress	$1.826 \times 10^7 \text{ N/mm}^2$
Maximum Strain	1.792×10^{-4}
Factor of Safety	4.350
Maximum Displacement	2.379 mm

Stress analysis shows stress concentration and distribution on Top Sheet as expected and max value for Von Mises Stress (Fig. 4.20) is 18.26 MPa Max value for Strain (Fig. 4.22) is 1.792×10^{-4} . Factor of Safety (FoS) (Fig. 4.23) value is 4.350. The maximum value for displacement (Fig. 4.24) is 2.379 mm.

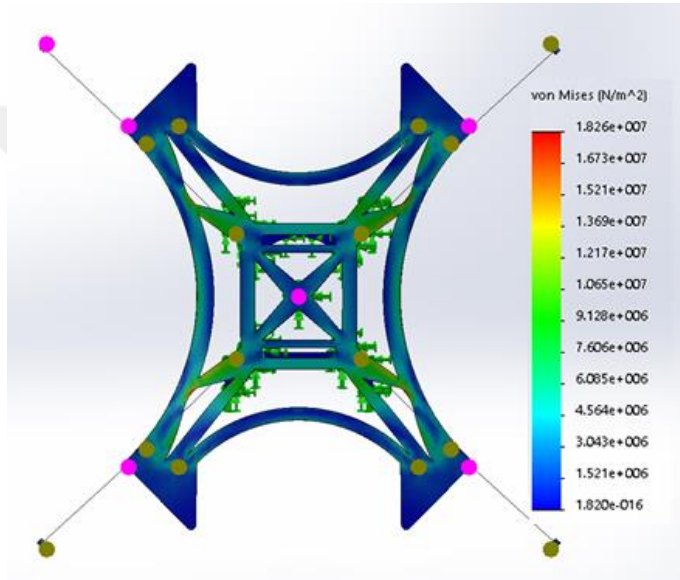


Fig. 4.20. Stress concentration on chassis.

The result for Von-Mises stresses of UAV Chassis is shown in Fig. 4.20 The stresses concentrated on vertical pipes for connecting UAV arm to the top and the bottom plate of the chassis. The maximum stress is 18.26 MPa at concentrated on the second joint and indicated as j2 in Fig. 4.21.

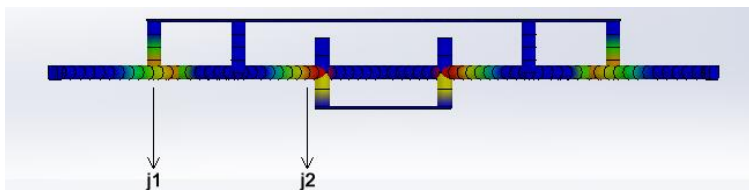


Fig. 4.21. Stresses on joints.

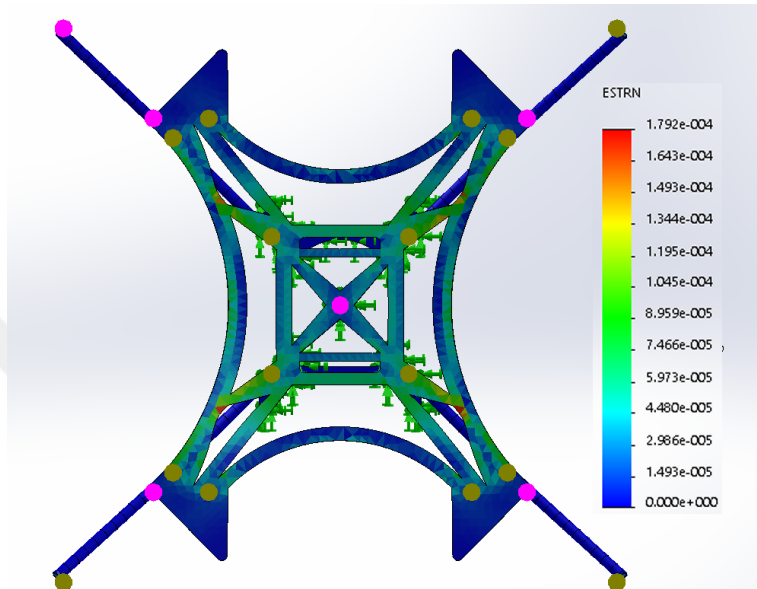


Fig. 4.22. Strain result.

The strain result is shown in Fig. 4.22 and minimum FoS value is above 4 as shown in Fig. 4.23.

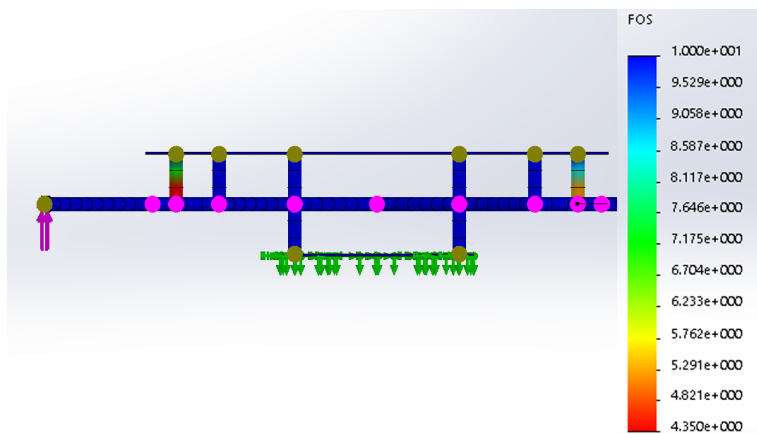


Fig. 4.23. FoS result

The FEA result for the maximum displacement of the chassis is 2.38 mm as indicated in 4.24.

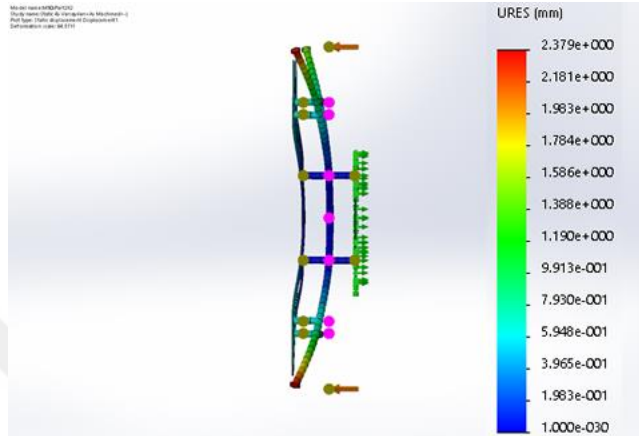
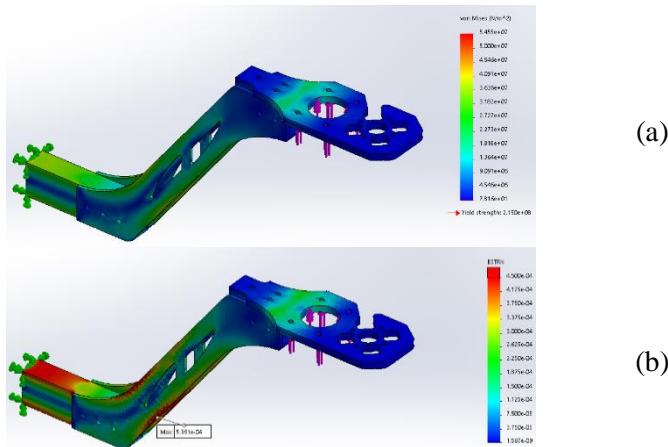


Fig. 4.24. Displacement result.

The designed VTOL UAV arm is manufactured using Al 6063-T6 rectangle weldment profile tubes, Al 6068-T6 sheets, and gear reducer and connector parts are produced using Al 7075-T6. The VTOL UAV arm weight is 1.0 kg and close to carbon fiber arms' weight sold in the market. It is suitable for mass production, weldable, cheaper and modifiable when compared to carbon fiber arms.

The result of the Von-Mises stresses for the UAV Arm is shown in Fig. 4.25. The maximum stress (Fig. 4.25 (a)) observed on the arm is 54.55 MPa and maximum value for Strain (Fig. 4.25 (b)) is 4.500×10^{-4} . Factor of Safety (FoS) (Fig. 4.25 (c)) value is 4.94. Maximum value for displacement (Fig. 4.25 (d)) is 2.246 mm.



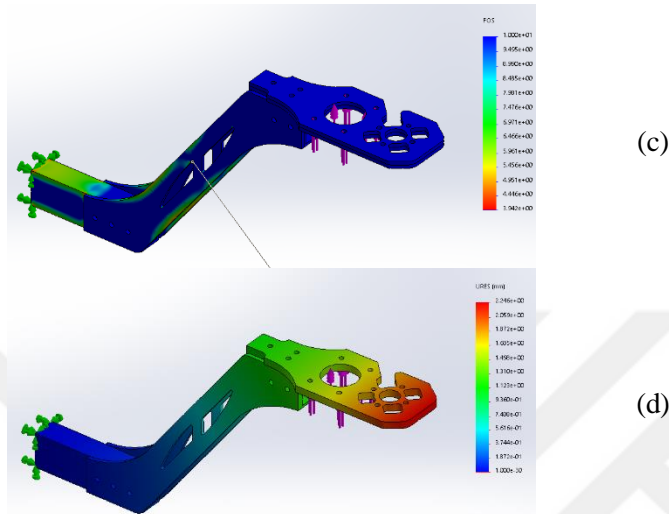


Fig. 4.25. VTOL UAV Arm Stress (a), Strain (b), FoS (c) and displacement (d) analysis results.

For the UAV both experimental and simulation modal test are implemented. The experimental Modal test gathered from the Signal Analyzer and results for the UAV chassis shown in Table 4.7 for five mode shapes. It is observed that coherences of the responses for different nodes is close to 1.

Table 4.7. Experimental Modal Test result.

Mode No	Natural Frequency (Hz)	RPM	Thrust (N)	Quad Thrust (N)
1	14.6	876	6.9	27.6
2	29.3	1758	27.9	111.6
3	43.9	2634	62.7	250.8
4	58.6	3516	111.6	446.4
5	73.1	4386	173.8	695.2

Modal tests are conducted for chassis of the UAV shows vibration caused by resonance frequencies for different modes affecting the chassis from inner to outer as seen in Table 4.7. It is important to consider first three frequencies in order to avoid oscillations on flight controller. The first five mode shapes calculated from the analysis are indicated in Table 4.8.

Table 4.8. Mode Shapes.

Result

Mode Shape

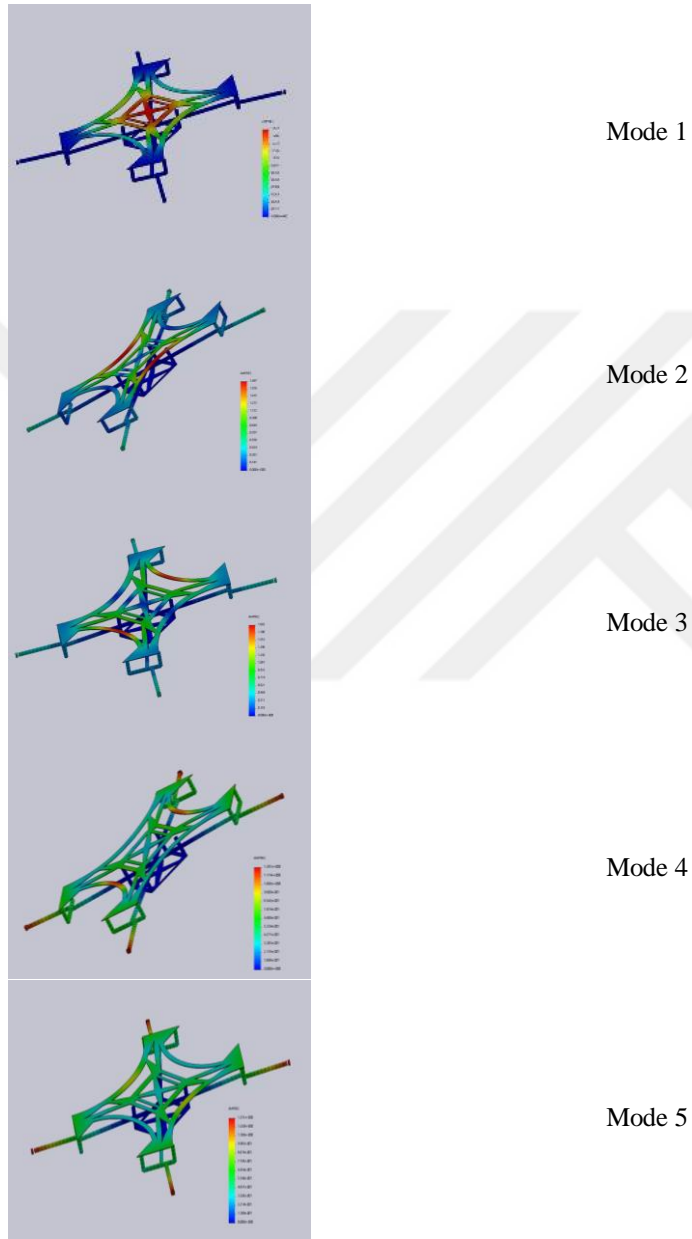


Table 4.9. Modal analysis result.

Mode No	Natural Frequency (Hz)	RPM	Thrust (N)	Quad Thrust (N)
1	13.09	785.40	-	-
2	35.62	2137.20	48.20	192.60
3	36.64	2198.58	51.00	204.10
4	41.77	2506.50	65.40	261.60
5	42.14	2528.76	66.40	265.80

Comparison chart for the experimental and simulation results are shown in Table 4.10.

Table 4.10. Modal analysis result comparison.

Mode No	Experimental Natural Frequency (Hz)	Theoretical (Natural Frequency (Hz))
1	14.6	13.09
2	29.3	35.62
3	43.9	36.64
4	58.6	41.77
5	73.1	42.14

When the operational properties of UAV considered, ideal-flying weights are over the first three critical frequencies (Table 4.10). In order to prevent flying in resonance frequency the weight and payload parameters are considered for safe flying.

Table 4.11 and 4.12 show theoretical thrust results for both propellers but the angular velocity limited due to manufacturing and material limitations. The maximum angular velocity is 5000 rpm for each propellers.

Table 4.11. 3095 propeller theoretical results.

Angular Velocity ω (RPM)	Static Thrust, F (N)	Static Thrust, F (g)	Static Thrust, F (kg)
1000	9,03	921,04	0,92
1500	20,32	2072,34	2,07
2000	36,16	3684,16	3,68
2500	56,47	5756,51	5,76
3000	81,31	8289,37	8,29
3500	110,68	11282,75	11,28
4000	144,56	14736,66	14,74
4500	182,96	18651,08	18,65
5000	225,88	23026,03	23,03
5500	273,32	27861,50	27,86
6000	325,27	33157,48	33,16
6500	381,74	38913,99	38,91
7000	442,73	45131,02	45,13
7500	508,24	51808,57	51,81

Table 4.12. 3010 propeller theoretical results.

Angular Velocity ω (RPM)	Static Thrust, F (N)	Static Thrust, F (g)	Static Thrust, F (kg)
1000	10,01	1020,54	1,02
1500	22,53	2296,22	2,30
2000	40,05	4082,18	4,08
2500	62,57	6378,40	6,38
3000	90,10	9184,90	9,18
3500	122,64	12501,67	12,50
4000	160,18	16328,71	16,33
4500	202,73	20666,02	20,67
5000	250,29	25513,61	25,51
5500	302,85	30871,46	30,87
6000	360,42	36739,59	36,74
6500	422,99	43117,99	43,12
7000	490,57	50006,67	50,01
7500	563,15	57405,61	57,41

The 3010 propeller and 3095 propeller performance results obtained from measured values are represented in Table 4.13 and 4.15 The temperature effect of the different pitch on the motor, ESC, and gear set is investigated which listed in Table 4.14 and 4.16, respectively.

Table 4.13. 3010 propeller experimental test results.

Elapsed Time (min.)	Power (W)	Prop. Angular Velocity (Rad/s)	Mod. Duty Cycle (%)	Signal Thrust (N)
0	0.00	0.00	5.30	-
0	164.80	133.01	6.68	16
-	327.76	167.75	6.88	26
-	569.94	196.53	7.08	35
-	849.45	226.36	7.28	47
5	1085.13	246.01	7.48	57
-	1397.55	266.36	7.72	67
-	1705.81	281.10	7.92	75
-	1970.50	295.84	8.12	82
10	2323.42	312.34	8.30	91

Table 4.14. 3010 propeller temperature test results.

Elapsed Time (min.)	Temperature			
	Motor	ESC	Pinion Gear	Room
0	22.4	22.4	22.4	22
0	24.5	22.5	23.5	22
5	58.0	36.8	36.0	22

10	65.0	37.0	35.0	22
----	------	------	------	----

Table 4.15. 3010 propeller performance test results.

Elapsed Time (min.)	Power (W)	Prop. Angular Velocity (Rad/s)	Mod. Signal Duty Cycle (%)	Thrust (N)
0	0	0	5.56	-
0	124.78	134.41	6.06	15
	247.12	167.05	6.18	24
	611.70	233.38	6.54	42
	847.84	263.21	6.74	54
	1159.03	294.44	7.00	68
5	1384.60	312.34	7.22	77
	1605.29	328.13	7.34	86
	1821.09	341.47	7.56	93
10	2415.42	369.89	8.00	110

Table 4.16. 3095 propeller temperature test results.

Elapsed Time (min.)	Temperature			
	Motor	ESC	Pinion Gear	Room
0	22.0	22.0	22.0	22
0	24.0	22.5	23.5	22
5	54.0	35.0	32.0	22
10	58.0	40.0	34.0	22

It is understood from tables that the angle of attack and power consumption are proportional to each other. For equal power consumption, a propeller produces more thrust when the angle of attack is lower. Motor, ESC and gear set temperatures are clearly increasing when the angle of attack is higher as it is seen in Table 4.14 and 4.16.

The data obtained from the performance tests implemented in this study is shown in Fig. 4.26-4.28. According to the charts showing the relation among power consumption, thrust force and angular speed, when the angular speed is the same, propellers with lower attack angle consumed less power and produced more thrust. For the same amount of power consumption, propellers with lower attack angle produced more thrust force.

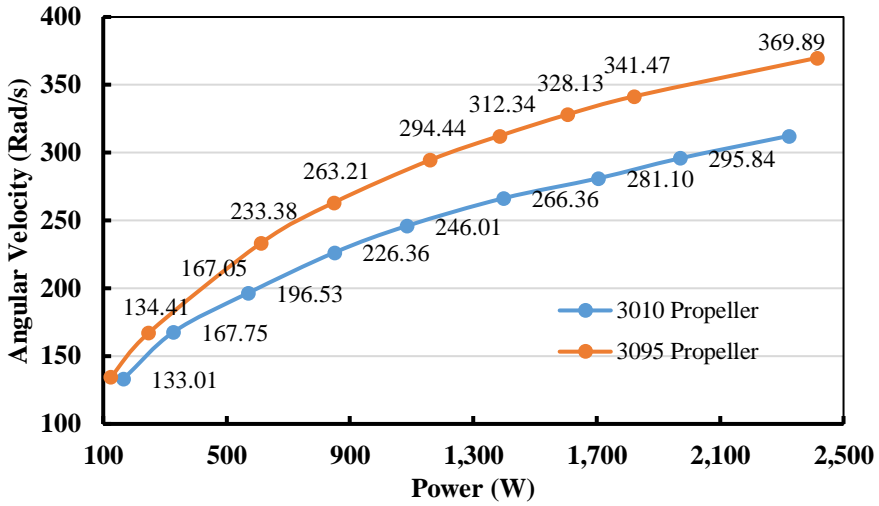


Fig. 4.26. Power - angular velocity relationship.

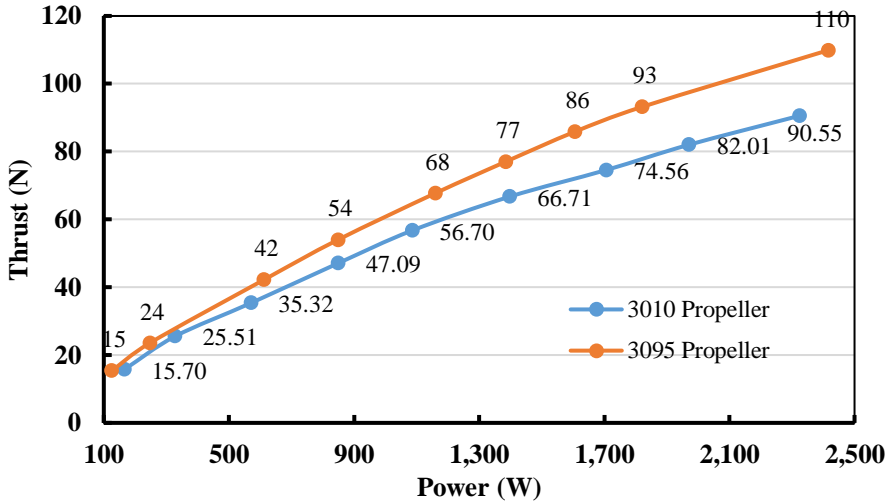


Fig. 4.27. Power - thrust relationship.

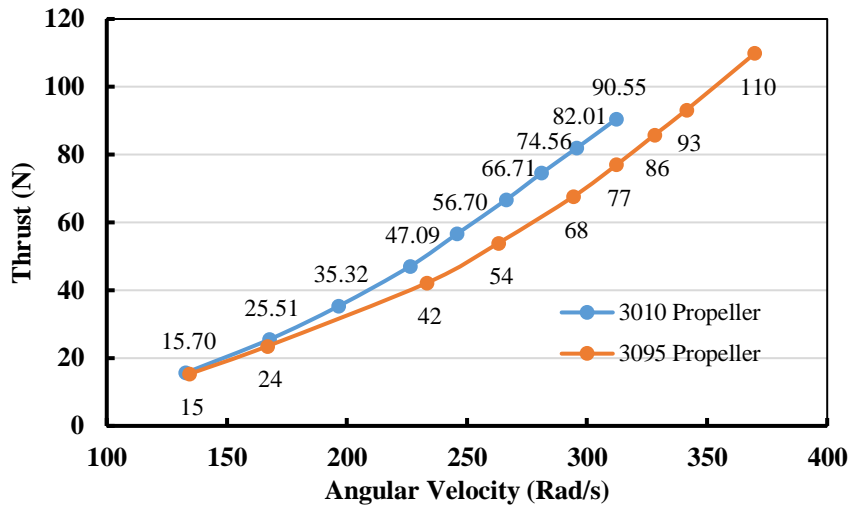


Fig. 4.28. Thrust - angular velocity relationship.

In order to determine the optimum attack angle of a propeller, the power consumption, which effects flight duration directly, should be considered. The reduction of attack angle enables smoother flight but provides less thrust force. Considering the same power consumption, a propeller with a lower attack angle could reach higher RPMs generating more thrust force. On the other hand, the lower attack angle propeller reaches the angular speed limit rapidly thus limiting lifting force.

According to the results of the study, a propeller with a lower attack angle is found to be more efficient for power consumption but the reduction of attack angle increased angular speed, and increment of angular speed brought limitations for maximum lifting capacity. As a result, for better payload capacity, choosing the propeller with a higher attack angle would be more convenient considering the same propeller length. However, for smoother and longer flights, lower attack angle could be the better choice. Results are compared using experimental data and theoretical calculations for 3010 and 3095 propellers shown in Fig 4.29 and 4.30 and RMSE percentages indicated in Table 4.17.

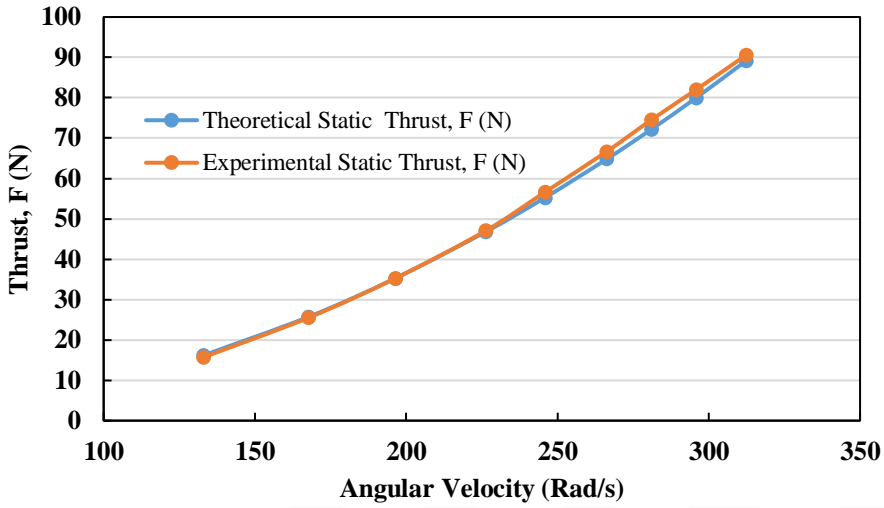


Fig. 4.29. Theoretical vs experimental result comparison for propeller 3010.

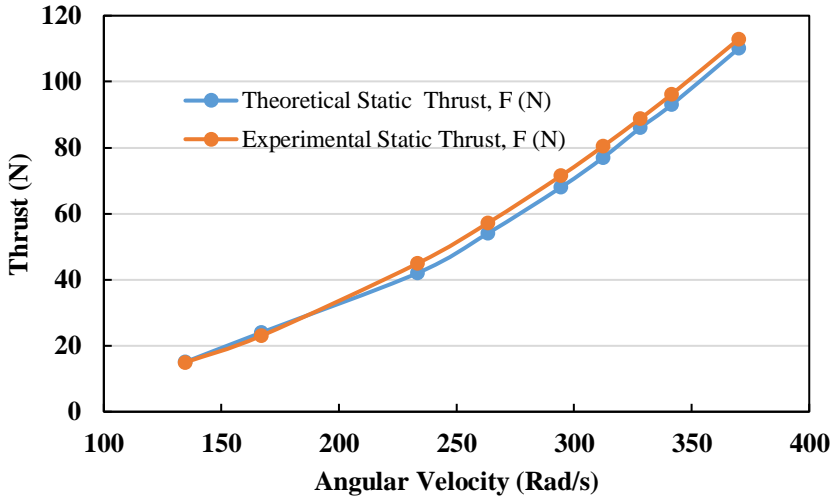


Fig. 4.30. Theoretical vs experimental thrust of the 3095 Propeller

Table 4.17. RMSE values for the 3010 and 3095 Propeller

Propeller	RMSE	Min Thrust Value (N)	Max Thrust Value (N)	RMSE Percentage
3010	1.39	0	250	0.56
3095	2.79	0	225,88	1.24

Table 4.18. Maximum flight conditions for the UAV.

	Climbing (m/s)	Forward Flight (m/s)
Max cond.	40	31
Max Pitch Angle	-	36.06°

Flight duration can be maximized by increasing the number of batteries but it also increases the total weight of the vehicle. For maximum conditions (Table 4.18), the VTOL UAV has a flight duration is close to 46.34 min (Fig. 4.31) for under 10 kg payload. Ideal flight duration of VTOL UAV according to its battery weight and flight duration relationship for 18.12 kg payload 19.27 min. is calculated.

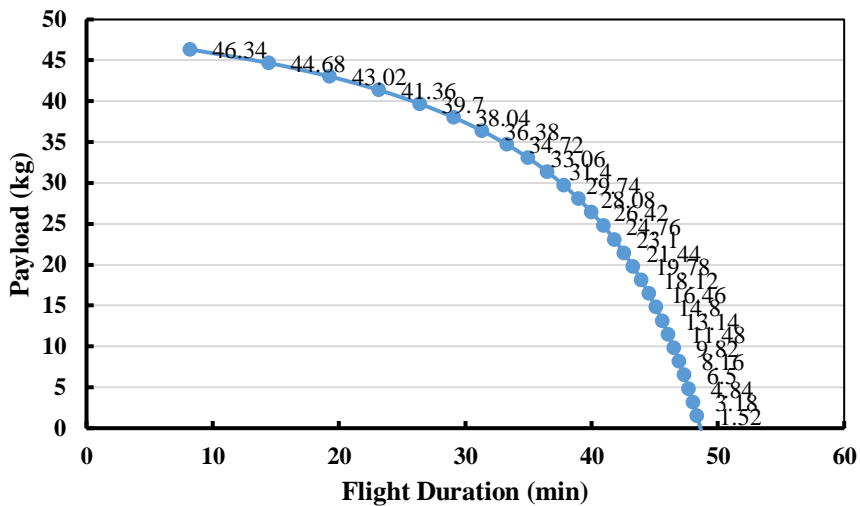


Fig. 4.31. Flight duration of the UAV.

The centrifugal force on the 3010 propeller is simulated for maximum conditions. Observed FoS is 4.3 for 524 rad/s that determined as the angular speed limit of the propeller. Simulation results are indicated in Fig 4.32 and Fig. 4.33 for strain and safety factor parameters.

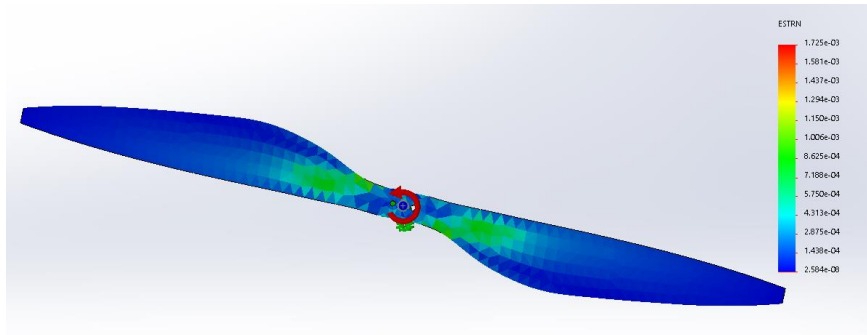


Fig. 4.32. The strain on the 3010 propeller for 524 Rad/s.

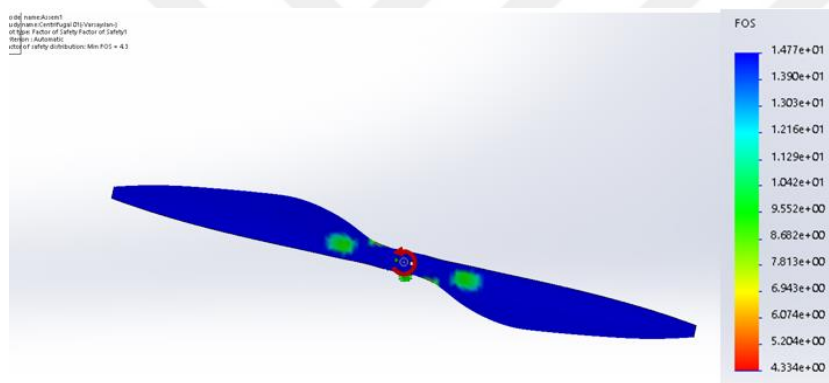


Fig. 4.33. The effect of the centrifugal force on the 3010 propeller for 524 Rad/s.

Weight and payload relationship of the UAV is indicated in Table 4.20.

Table 4.19. Weight and Payload Relationship for the UAV.

Parts	Weight (kg)	Pieces	Total Weight (kg)	
Main Frame, Landing Part and Arms and Avionics.	6.84	1	6.84	No Take-Off
Motor, Gear Reducer and Propeller	1.28	4	11.96	No Take-Off
Battery Set	0.84	2	13.64	Min Take-Off
Payload	47.19	1	60.00	Max Take-Off

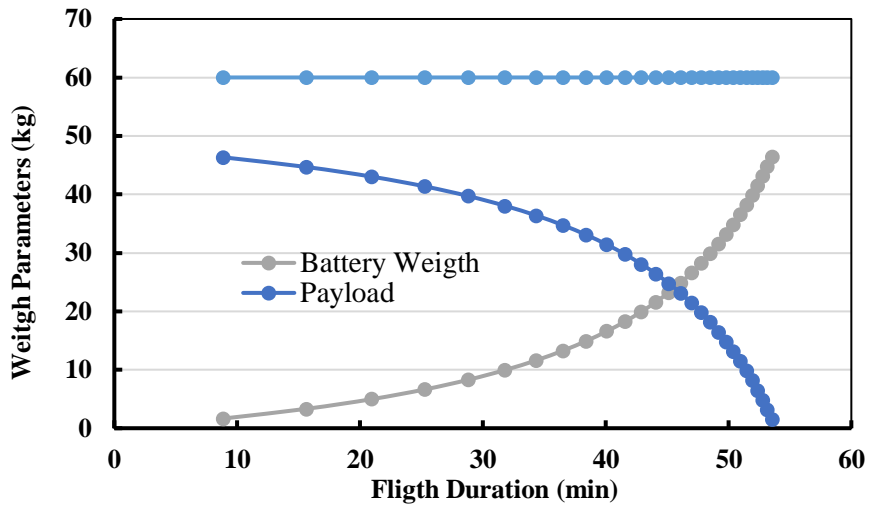


Fig. 4.34. The measured relationship among battery weight, payload and flight duration.

In order to investigate the strain on the arms by the propeller thrust force of the VTOL UAV strain measurement setup is used with a rosette type strain gage. The strain-voltage relationship is theoretically calculated. For VTOL UAV arm FEA strain results are investigated and compared with experimental strain results. The observed maximum strain is indicated in Fig. 4.35.

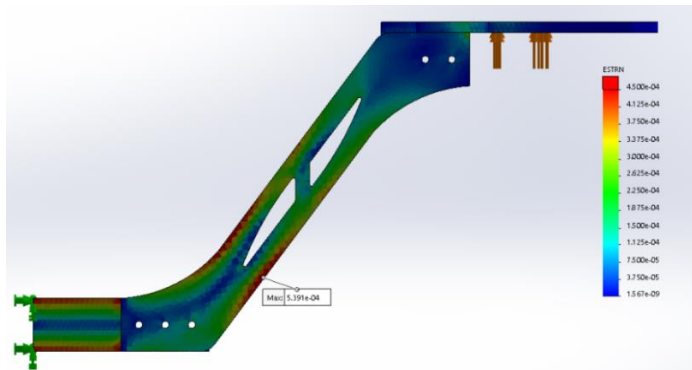


Fig. 4.35. Maximum Strain on the VTOL UAV arm (side view).

Force and voltage relationship indicated in Table 4.21 calculated by using theoretical formula.

Table 4.20. Force vs voltage relationship in theory.

Force (N)	€	GF	SgR	▲R	R1 (Act.)	R2 (Pas.)	R3 (Pas.)	R4 (Pas.)	Vout K x128
500	1.52E-03	2	360	1.09	361.09	360	360	360	4.86E-01
400	1.22E-03	2	360	0.88	360.88	360	360	360	3.89E-01
350	1.06E-03	2	360	0.77	360.77	360	360	360	3.40E-01
250	7.60E-04	2	360	0.55	360.55	360	360	360	2.43E-01
200	6.08E-04	2	360	0.44	360.44	360	360	360	1.94E-01
100	3.04E-04	2	360	0.22	360.22	360	360	360	9.72E-02
50	1.52E-04	2	360	0.11	360.11	360	360	360	4.86E-02
10	3.04E-05	2	360	0.02	360.02	360	360	360	9.73E-03

Experimental strain results for X, Y, XY axes shown in Table 4.22.

Table 4.21. Experimental strain results.

Force (N)	€a	€b	€c	€x (Normal Strain)	€y (Normal Strain)	€xy (Shear Strain)
500	1.07E-03	1.36E-03	-2.00E-03	1.07E-03	-2.00E-03	1.83E-03
400	8.57E-04	1.09E-03	-1.60E-03	8.57E-04	-1.60E-03	1.46E-03
350	7.50E-04	9.55E-04	-1.40E-03	7.50E-04	-1.40E-03	1.28E-03
250	5.36E-04	6.82E-04	-1.00E-03	5.36E-04	-1.00E-03	9.14E-04
200	4.29E-04	5.46E-04	-8.00E-04	4.29E-04	-8.00E-04	7.31E-04
100	2.14E-04	2.73E-04	-4.00E-04	2.14E-04	-4.00E-04	3.66E-04
50	1.07E-04	1.37E-04	-2.00E-04	1.07E-04	-2.00E-04	1.83E-04
10	2.14E-05	2.73E-05	-4.00E-05	2.14E-05	-4.00E-05	3.66E-05

SolidWorks simulation results for X, Y, XY axis strain shown in Table 4.23.

Table 4.22. SolidWorks simulation results.

Force (N)	Principal Strain	XY Shear Strain	XZ Shear Strain	YZ Shear Strain	Y Normal	X Normal
500	1.44E-03	1.84E-03	6.43E-07	2.11E-06	7.54E-04	2.10E-04
400	1.15E-03	1.47E-03	5.15E-07	1.69E-06	6.03E-04	1.68E-04
350	1.01E-03	1.29E-03	4.50E-07	1.48E-06	5.28E-04	1.47E-04
250	7.21E-04	9.21E-04	3.22E-07	1.06E-06	3.77E-04	1.05E-04
200	5.77E-04	7.37E-04	2.57E-07	8.46E-07	3.02E-04	8.38E-05
100	2.88E-04	3.68E-04	1.29E-07	4.23E-07	1.51E-04	4.19E-05
50	1.44E-04	1.84E-04	6.43E-08	2.11E-07	7.54E-05	2.10E-05
10	2.88E-05	3.68E-05	1.29E-08	4.23E-08	1.51E-05	4.19E-06

Experimental acquired principal strain (SN1) and SolidWorks analysis result (Principal Strain) comparison indicated in Fig 4.27.

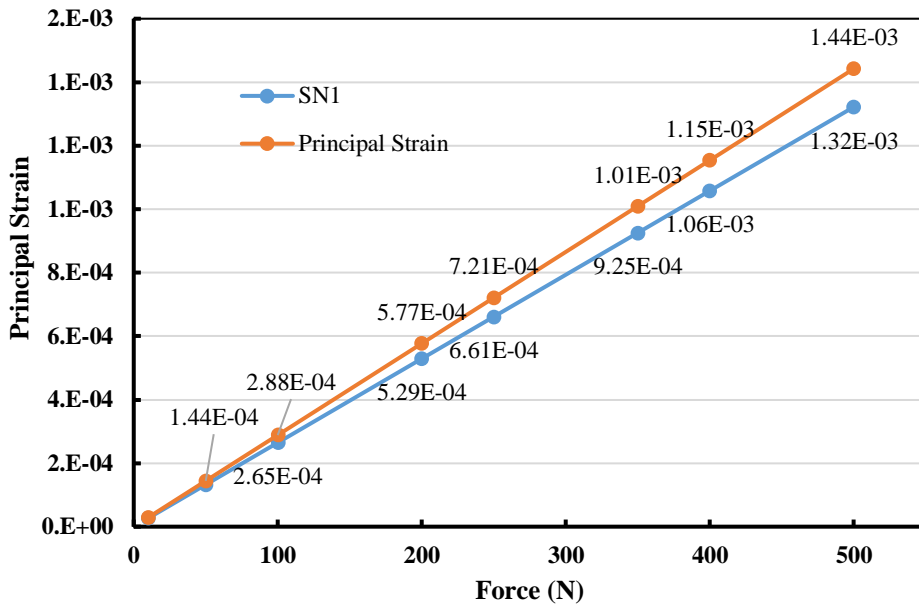


Fig. 4.36. Principal Strain comparison.

Experimental acquired shear strain (ϵ_{xy}) and SOLIDWORKS analysis result (XY Shear Strain) comparison indicated in Fig 4.36.

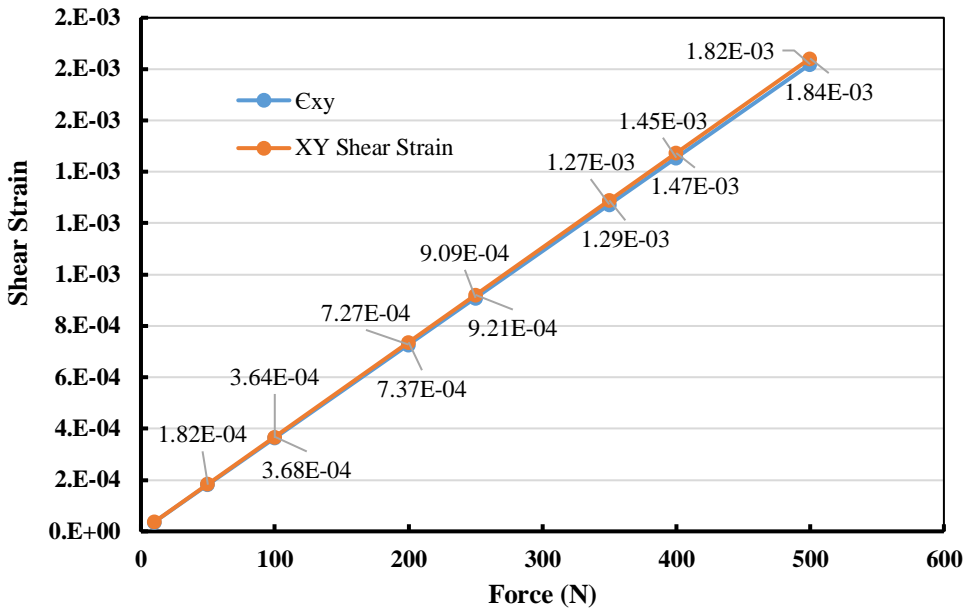


Fig. 4.37. Shear Strain comparison.

In order to reduce the costs the main gear is manufactured by using a 3D printer. FEA result (Fig. 4.38) for the desired torque is investigated and in line with this direction a few types of filaments are printed. Tensile tests are implemented for these filaments using a tensile test machine. Result is shown in Table 4.39 for comparison.

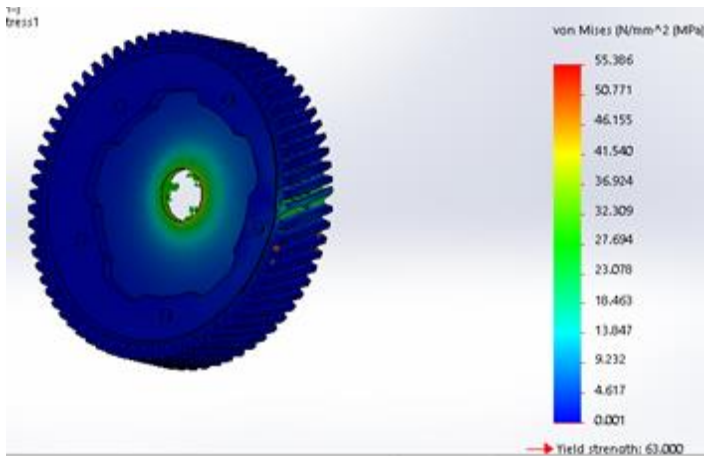


Fig. 4.38. Main Gear Analysis.

Table 4.23. Main gear tensile tests results.

Material	Yield Strength(~MPa)	Tensile Strength (MPa) (Catalog)
Delrin	68	68
PLA+ ESUN	41	60
ElitePLA Oo-Kuma	45	102
CF Reinforced Nylon Filament	60	118
ePa CF ESUN		



Fig. 4.39. 3D Printed Main Gear.

Assembling of the main gear with gear reducer and the motor holder is shown in Fig 4.40.



Fig. 4.40. Manufactured gear reducer assemble.

In order to decrease the total weight of the aerial vehicle aluminum material is a good alternative. In this study, an aluminum PDB (Fig. 4.41) used for distributing the power for VTOL UAV arm.



Fig. 4.41. Aluminum Power Distribution Board.

Specifications of the aluminum board are indicated in Table 4.24.

Table 4.24. Specifications of the Aluminum PDB.

Specification	Description
Input	2 Parallel Power Input
Output	4 Parallel Power Output
Grounding	External Grounding Connection
Current Limitation:	Up to 600A
Connector Type:	Bullet 6mm

4.4 The Sprayer

The sprayer part includes a diaphragm pump, fluid tank, boom, and nozzles. It is mounted on the VTOL UAV in order to compose the Aerial Sprayer as shown in Fig 4.42.



Fig. 4.42. Sprayer UAV.

For aerial applications, the Center of Gravity (CG) plays an important role in stabilized flight. The free surfaces of a tank mounted on a UAV mainly affect the CG. In order to decrease the disturbance effect of the CG a sponge filled in the tank of the developed VTOL UAV. The filled material that is a kind of thermoset decreases above 95% percent free space in the tank. It affects the suction of the pump (Pressure) and increases the weight of about 26%. The image of the sprayer is shown if Fig. 4.33.



Fig. 4.43. The sprayer.

A tank with the sponge and without sponge compared by considering volume flow rate and pressure difference result shown in Table 4.26 and 4.27 respectively.

Table 4.25. Tank with sponge.

Time Duration (sec)	V(ml)	Q (Volume Flow Rate)(m ³ /s)	l/min	Error (It)
80.08	2940	3.67E-05	2.20	3.18E-02
78.43	2820	3.60E-05	2.16	-1.36E-02
78.73	2820	3.58E-05	2.15	-2.19E-02
78.32	2840	3.63E-05	2.18	4.71E-03
78.25	2830	3.62E-05	2.17	-1.01E-03

The tests for the sponge-filled tank shows that the sponge absorbs about 26% of the fluid for a 10-liter sponge filled the tank. Its flow rate of 2.16 l/min with an RMSE percentage of 0.85%. Pump efficiency is 80.87% for spraying with this tank.

Table 4.26. Tank without sponge.

Time Duration (sec)	V(ml)	Q (Volume Flow Rate)(m ³ /s)	l/min	Error (It)
129.29	4.72E+03	3.65E-05	2.19	1.05E-02
128.75	4.72E+03	3.67E-05	2.20	2.20E-02
133.22	4.76E+03	3.57E-05	2.14	-3.38E-02
131.34	4.76E+03	3.62E-05	2.17	-3.11E-03
131.71	4.79E+03	3.64E-05	2.18	4.44E-03

The tests for the non-sponged tank shows that above 73% of the fluid can be sprayed for a 10-liter tank. Its flow rate 2.17 l/min with an RMSE percentage of 0.86%. Pump efficiency is 81.93% for spraying with this tank.

The sprayer mechanism has four nozzles on the boom with gaps. The gaps between nozzles are set to 50 cm and nozzles adequate for pressures close to 4-40 psi by providing a good spray pattern. The spraying pattern is shown in Fig. 4.44 and calculated spraying coverage area is 2.5461 m² with spraying width 2.60 m (Fig. 4.45).

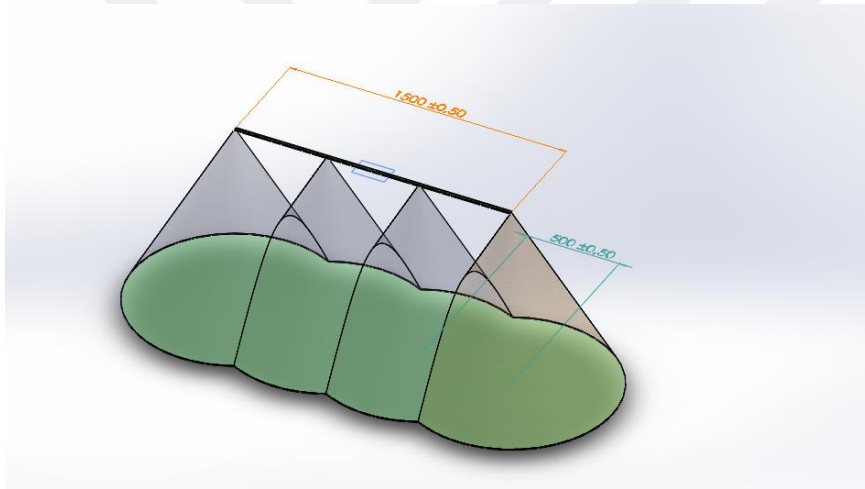


Fig. 4.44. Spraying area for the 1.5 m boom with four nozzles.

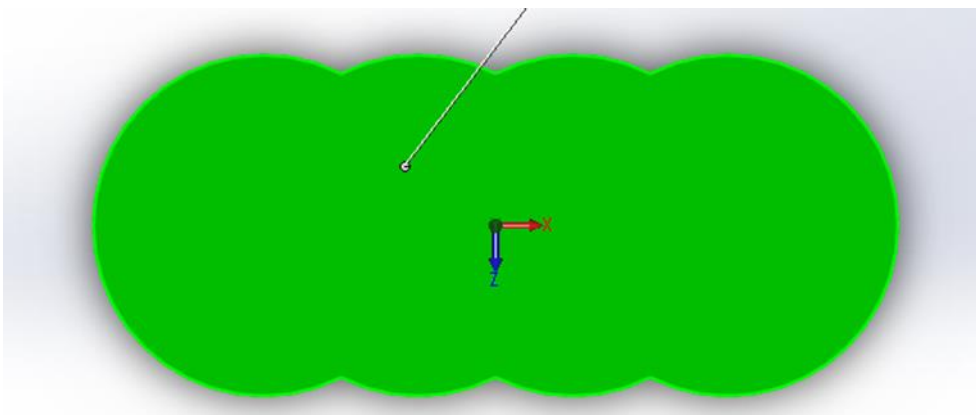


Fig. 4.45. Spraying pattern for the 1.5 m boom with four nozzles.

4.5 UGV and Multispectral Camera

For remote sensing tests in the field, the UGV is used with the multispectral camera. Cucumber plants are planted (Fig. 4.46) in planters as target plant samples. The multispectral camera mounted on the UGV using a gimbal (Fig. 4.47) for increasing the stabilization of the camera and decreasing the vibrations. The height of the camera lenses from the cucumber plants in the planters is close to 1 m. The parallel distance between planter and UGV is observed at 10 cm. The UGV is driven alongside the planter at a constant speed with the help of the PWM signal that is receiving from a remote controller.

Tests are accomplished for two different speeds for 0.33 m/s and 1.02 m/s. In the field tests, cucumber leaves are investigated for NDVI data, NDVI and LAI and only vegetation averaged NDVI data.

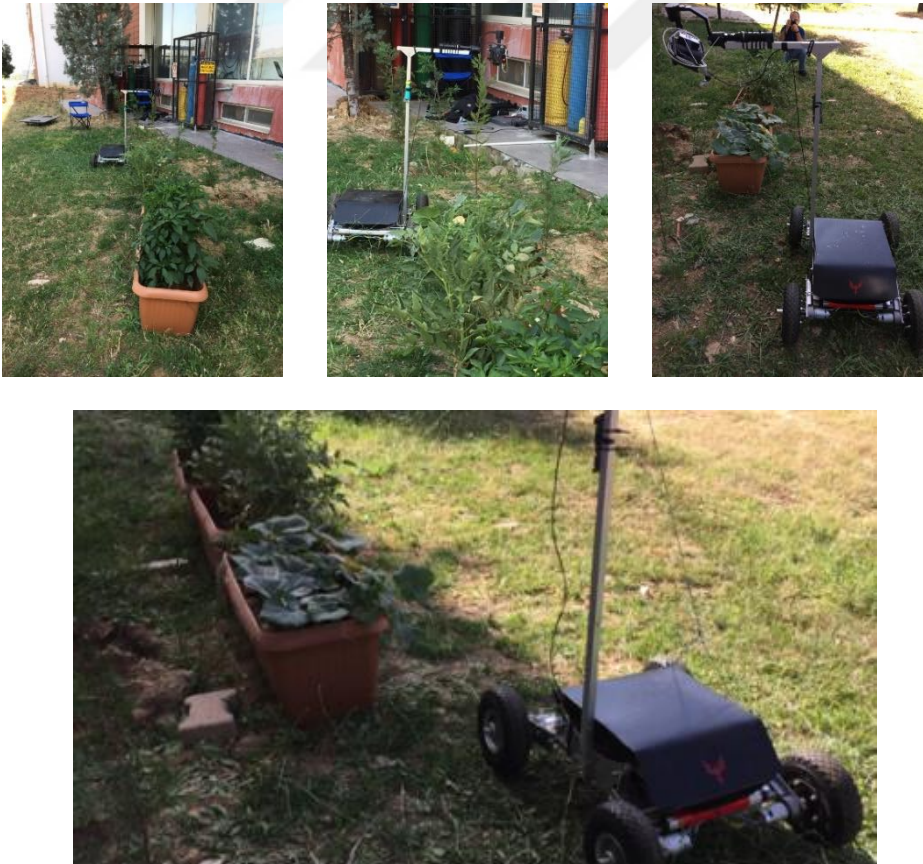


Fig. 4.46. Images from field tests.



Fig. 4.47. The mounted gimbal and the multispectral camera on the UGV.

For the test with the speed is 0.33 m/s, acquired NDVI data, NDVI and LAI and only vegetation averaged NDVI data are shown in Figs. 4.47, 4.48, 4.49 and 4.50.



Fig. 4.48. Planted cucumbers in the planter.

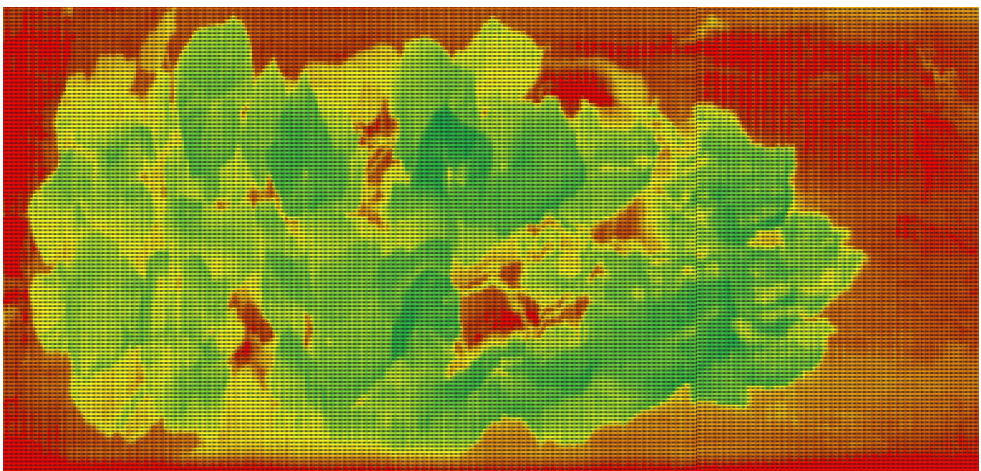


Fig. 4.49. NDVI result of the cucumber plant.

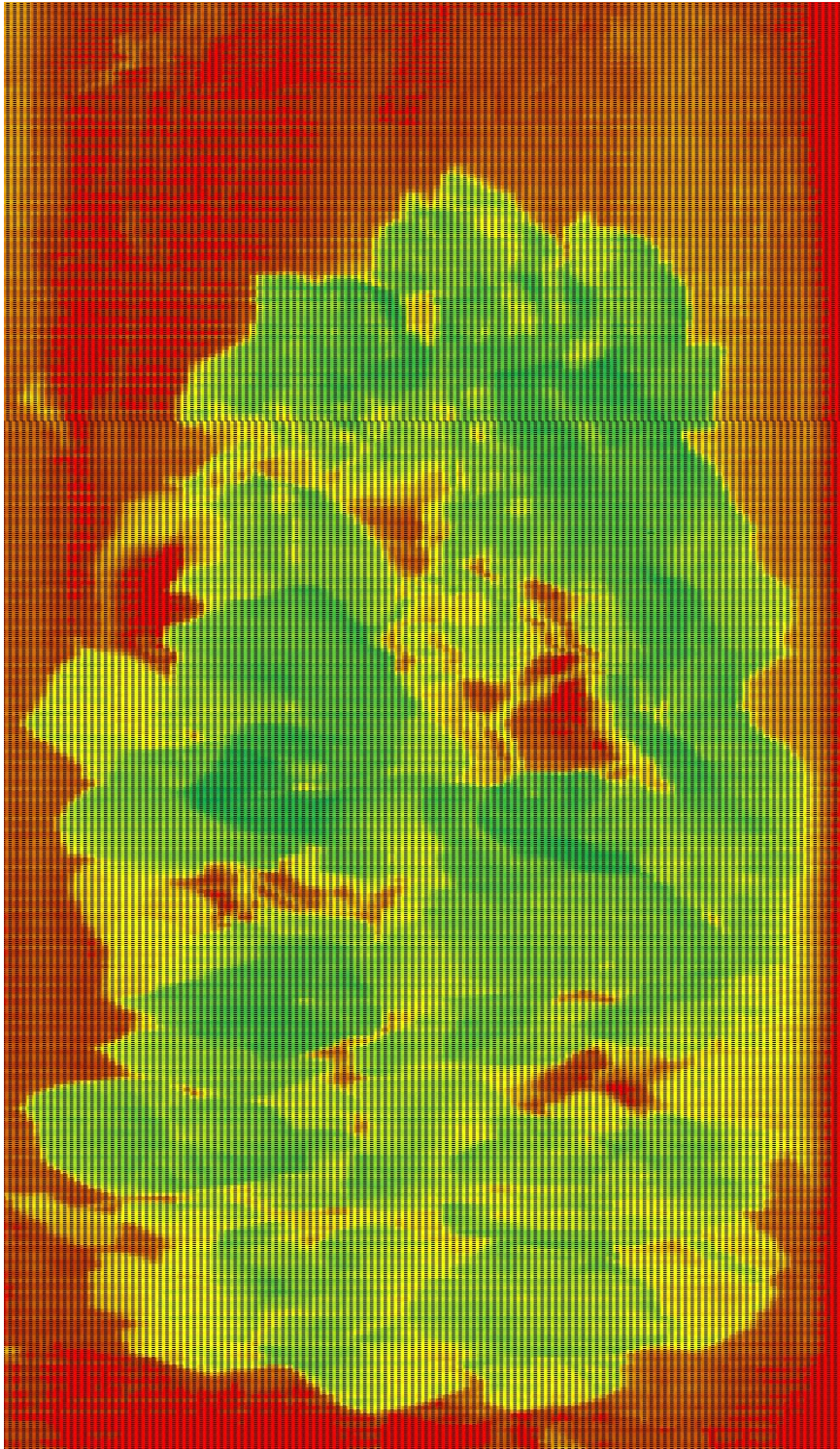


Fig. 4.50. Extended image for NDVI result of the cucumber plant.

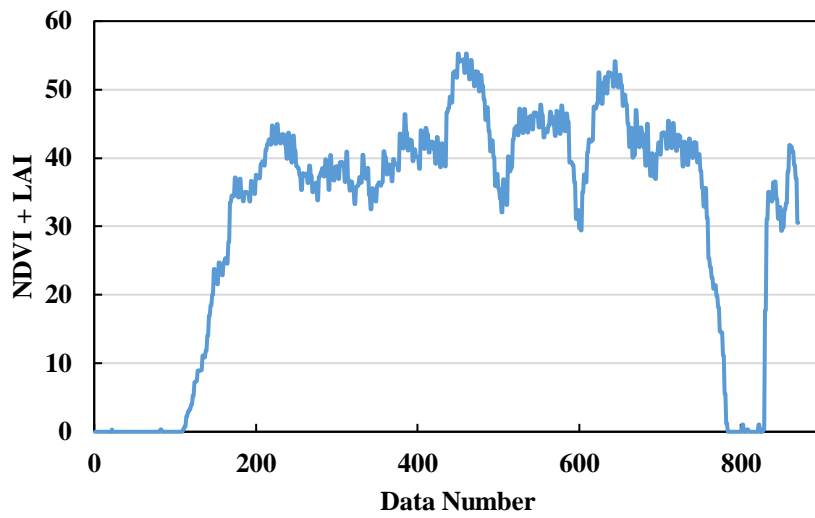


Fig. 4.51. Healthy Percentage using NDVI with LAI.

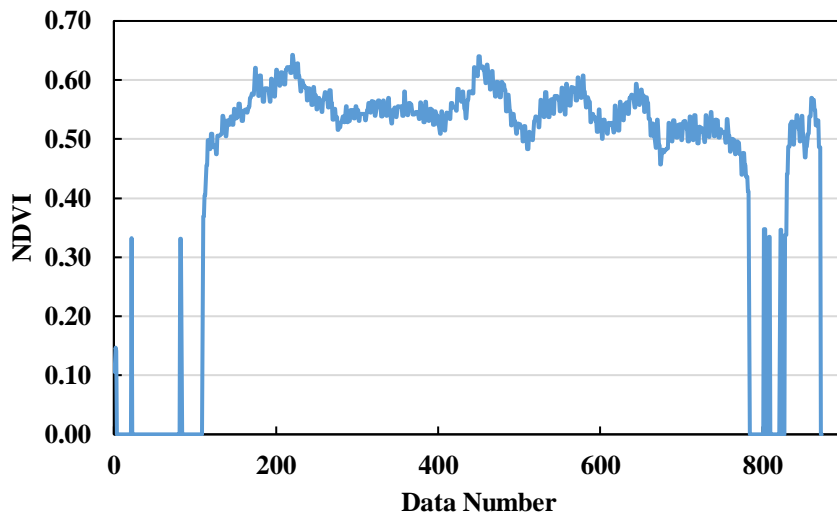


Fig. 4.52. NDVI Data including only Vegetation.

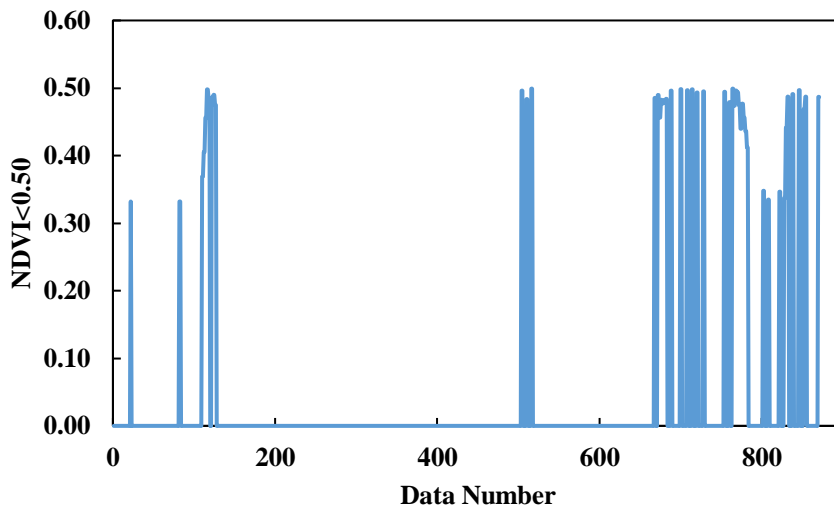


Fig. 4.53. NDVI Data for under 0.5.

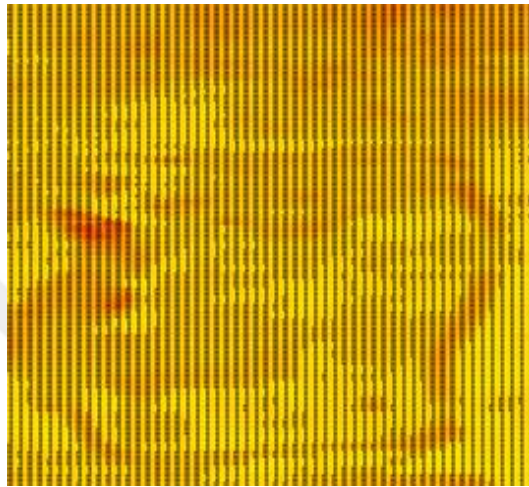
The second test is accomplished with the speed is 1.02 m/s, acquired NDVI data, NDVI and LAI and only vegetation averaged NDVI data are shown in Fig. 4.54, 4.55, 4.56 and 4.57.



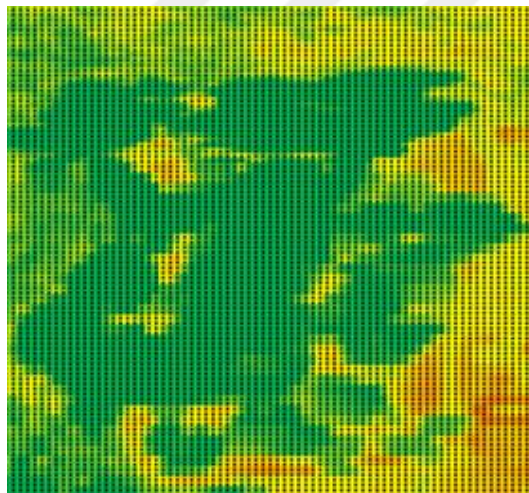
Fig. 4.54. Planted cucumbers in the planter.

Output

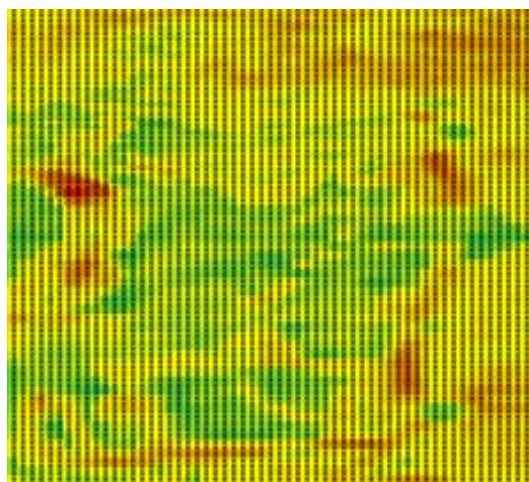
Spectral Band



Red (660nm)



NIR (850nm)



NDVI (660 and
850nm)

Fig. 4.55. Spectral band results for planted cucumbers in the planter.

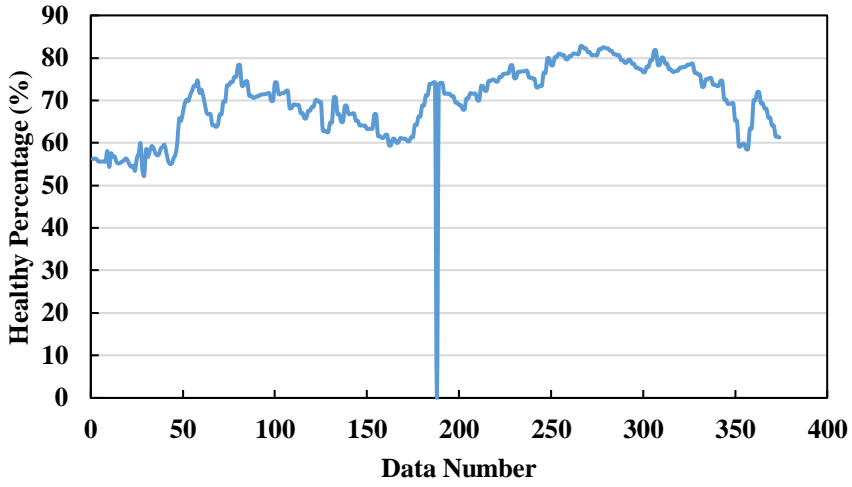


Fig. 4.56. Healthy Percentage using NDVI with LAI.

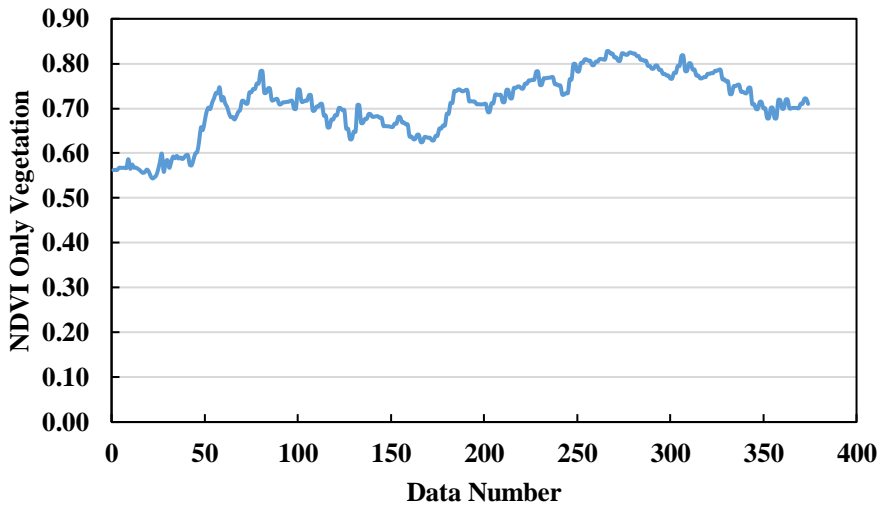


Fig. 4.57. NDVI Data including only Vegetation.

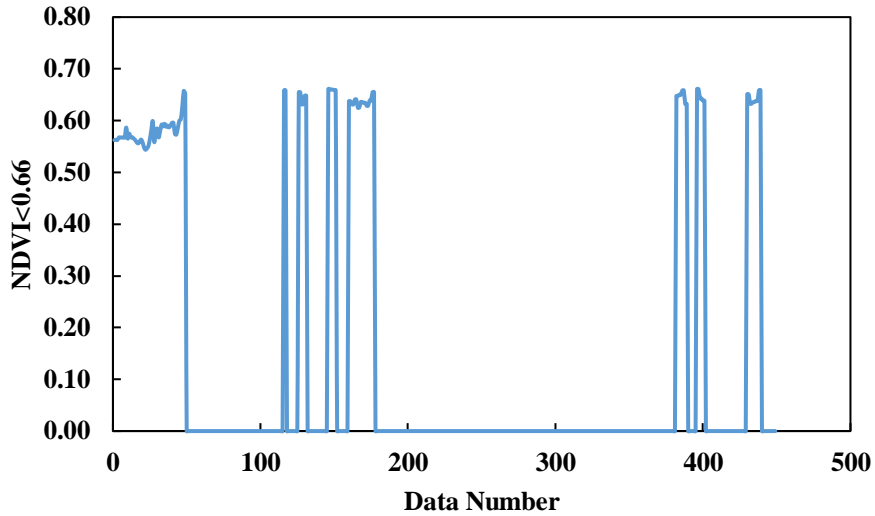


Fig. 4.58. NDVI Data for under 0.66.

4.6 Aerial Spraying UAV

Field test for aerial sprayer UAV is investigated in two stages for positioning accuracy and spraying coverage. In the first stage, the spraying pattern is determined for the hovering position of the UAV. Different heights are examined experimentally in steady-state conditions while propellers are on and off.

In the first stage, for investigating positioning accuracy autonomous flight test results are obtained using the small UAV. An image of the small UAV in the test field and flight log for the autonomous flight is shown in Fig. 4.59



Fig. 4.59. The small UAV in the test field and flight log.

The deviation between each destination waypoint and small UAV positioning for that point is analyzed using the Haversine formula. The result obtained in meters for each point as shown in Table 4.28 and the average error is found 0.71 with RMSE value 0.82.

Table 4.27. Positioning deviation in meters.

Fligth-1_Diff (m)	Fligth-2_Diff (m)	Fligth-3_Diff(m)
0.71	0.69	0.38
0.67	0.95	0.5
1.05	0.98	1.09
0.79	1.08	1.38
1.15	0.4	1.26
0.38	0.6	0.13
0.77	0.35	0.13
0.28	0.4	0.4
0.3	0.52	0.67
0.13	0.28	0.63
0.63	0.44	0.23
1.82	1.78	1.8
0.83	1.17	0.8
0.23	0.92	0.81
0.19	0.85	0.44
0.6	0.54	0.76

In the second stage, the spraying pattern is investigated for the aerial sprayer UAV that shown in Fig 4.60.

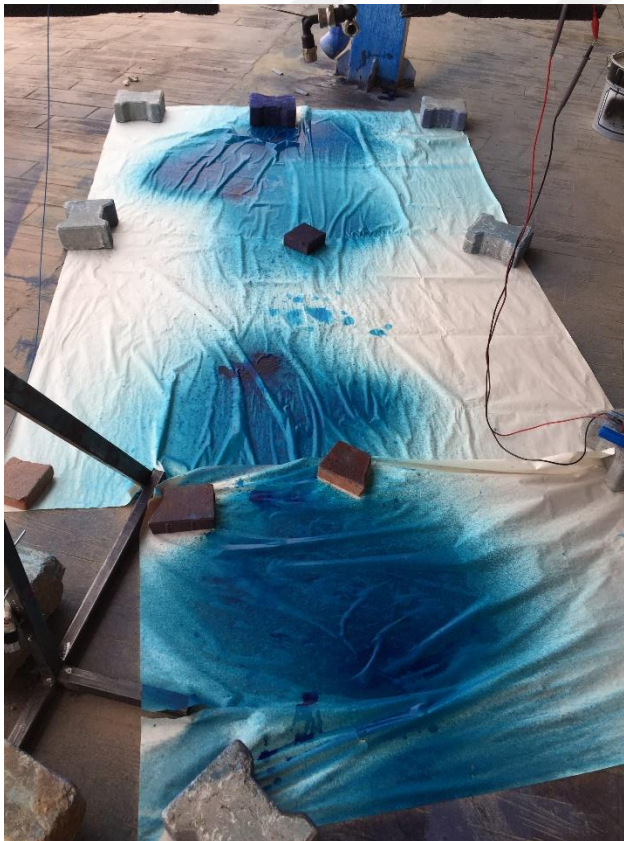


Fig. 4.60. Spraying pattern testing setup.

For a sprayer UAV, the propeller effects spraying pattern directly. In order to minimize the distribution effect of the propellers on the spraying pattern, it is possible to use a telescopic or a foldable spraying boom instead of a fixed one. On the other hand, without increasing the weight and complexity, there is also another solution to addressing this issue by increasing the spraying height with regard to the ground. In line with this direction, spraying tests are investigated (Fig. 4.60) under different heights for spraying UAV in hovering position. The obtained spraying pattern is shown in Fig. 4.61 (a) and Fig. 4.61 (b) for 1-meter distance.



(a)



(b)

Fig. 4.61. Spraying pattern for 1-meter height while UAV is hovering, front view (a), side view (b).

Obtained spraying pattern is shown in Fig. 4.62 (a) and Fig. 4.62 (b) for 2 meter distance.



(a)

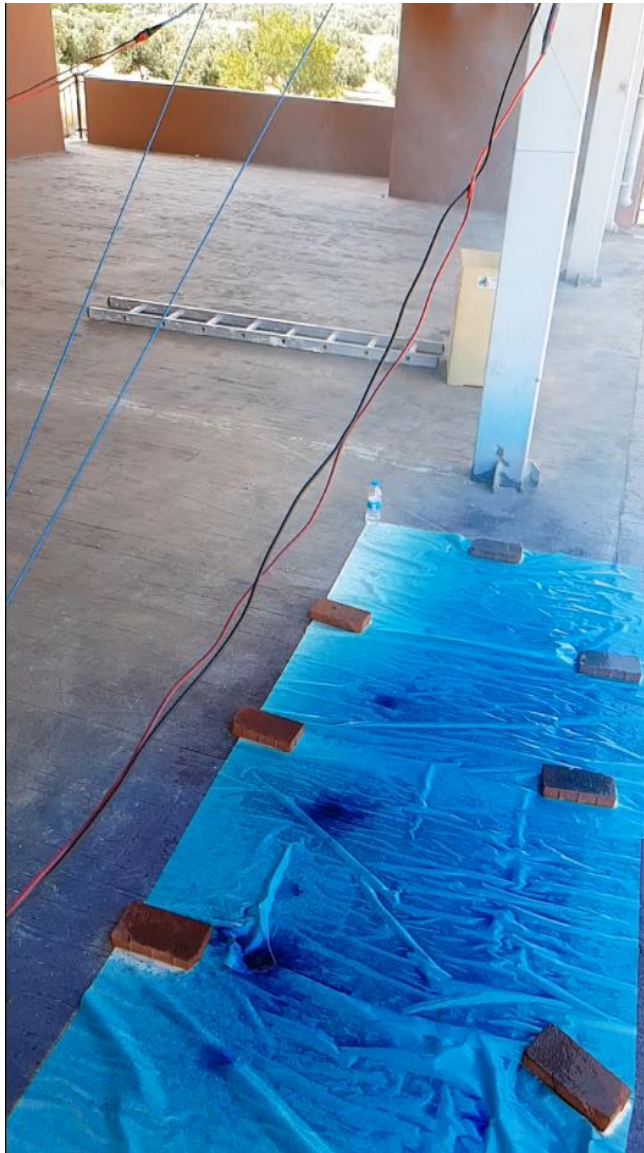


Fig. 4.62. Spraying pattern for 2-meter height while UAV is hovering, front view (a), side view (b).

Spraying results for 1 and 2 meters are observed experimentally and the resulting patterns are indicated in Fig. 4.45 and Fig. 4.46 respectively.

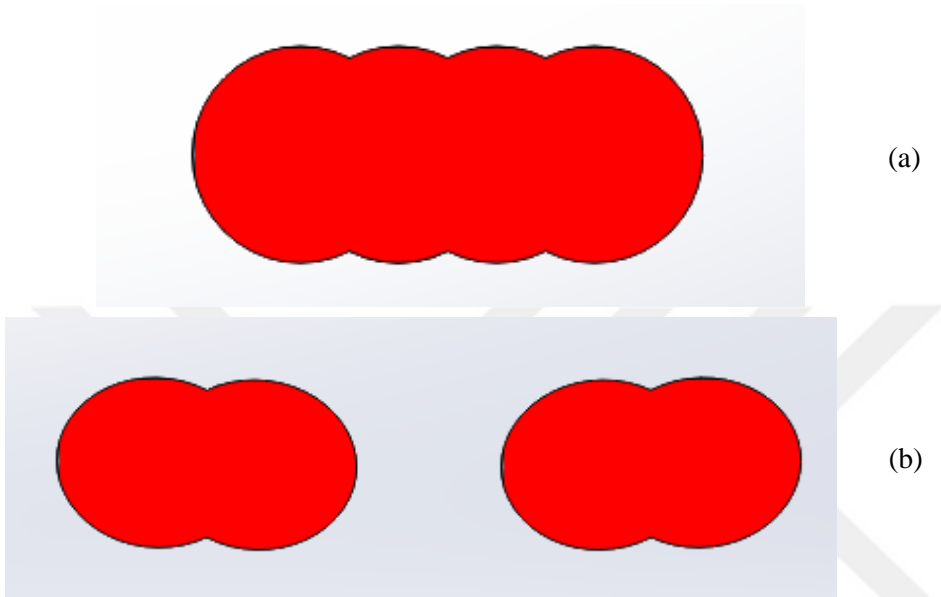


Fig. 4.63. Spraying pattern for 1-meter height with (b) and without (a) propeller effect.

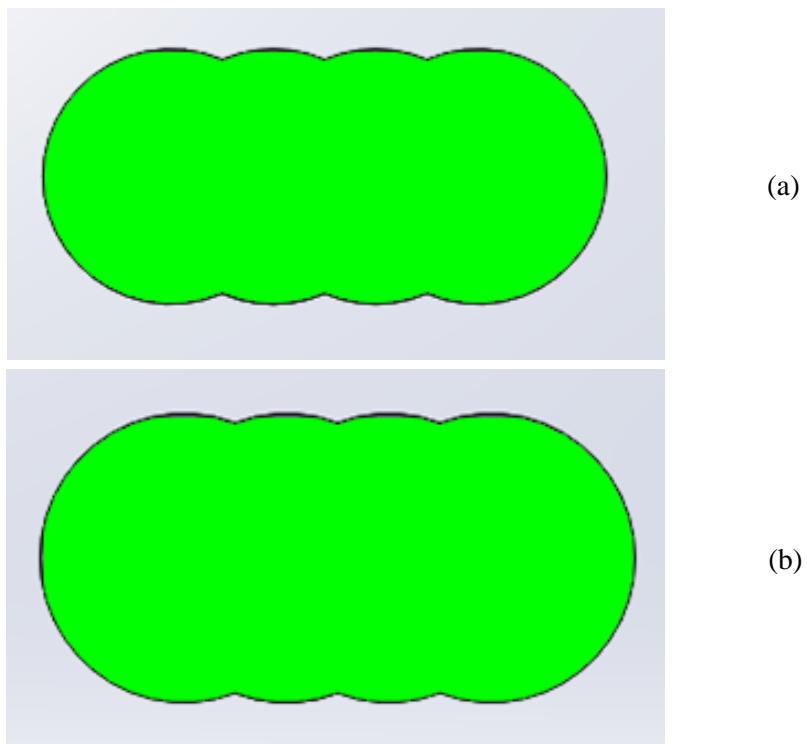


Fig. 4.64. Spraying pattern for 2-meter height with (b) and without (a) propeller effect.

Table 4.28. Spraying distance and spraying pattern comparison.

Spraying Duration (sec)	Volume (ml)	Distance (m)	Width (cm)	Length (cm)	Spraying Coverage (m²)
5	4.72E+03	1 (prop. off)	110	260	2.54
5	4.72E+03	1 (prop. on)	90	300	2.70
5	4.76E+03	2 (prop. off)	125	275	3.43
5	4.76E+03	2 (prop. on)	140	290	4.06

The results indicate that using spectral imaging techniques for plant disease detection is providing accurate information about plant health status. Also using the NIR band as an addition to the visible Red band helps to improve the accuracy of the sensor with the help of normalizing the NIR and Red band ratio. Using a spectral imaging device on a UGV gives the ability to collect data from close distance in comparison to satellite or aircraft imagery. In the field tests, it is observed that using a gimbal is a necessity in order to decrease the vibration of the arm which offers better imaging capability with low noise for the sensing device.

In spectral imaging applications, a line scanner's FoV and scanning frequency are playing an important role in order to acquire more accurate and detailed data. The scanning frequency of the imaging sensor and the cruising speed of the UGV should be correlated properly. If the speed of the UGV is too high compared to the scanning frequency of the imaging sensor, the obtained data becomes under sampled. In spite of the excessive low speed, the sensor acquires oversampled data. The indoor and outdoor tests conducted for spectral imaging demonstrate ND filters are a useable option in order to avoid from saturation region of the sensor. Providing correct wavelength bands to the testing environment with proper illumination is important for both indoor and outdoor applications. When using multiple sensor and lens solutions for optical measurement, the alignment of the sensors is dominant importance for getting a good overlap among spectral bands.

The tests conducted on aerial sprayer demonstrates payload of the vehicle is directly related to the batteries and weight of the UAV. Using aviation aluminum AL 7075 increasing initial costs but gives 3-dimensional endurance. PID plays an important role in order to provide a stabilized flight for the UAVs. It is better to use a Flight Controller that has the ability to perform auto-balancing PID coefficients for roll, pitch and yaw motions of the aerial vehicle. For aerial vehicles, CoG is an important

parameter for ensuring the stability of the vehicle. In this study, the sprayer unit of the UAV consists of a tank filled with a liquid that contains pesticides. The liquid in a tank affects the CoG of locomotion systems by the result of the free surfaces in the tank. In order to reduce the free surface effect on CoG of the aerial vehicle, the tank of the sprayer unit was filled with a sponge which nearly eliminated the effect of the free surface. The analysis of the propeller confirms that the thrust generated by the propellers of the UAV is providing adequate lifting capability for aerial spot spraying applications. Close distance spot spraying applications cause improper spraying patterns. For all that increasing spraying distance from the ground provides a better spraying pattern for these applications. Accuracy test for the UAV which using D-GPS is providing close to 1-meter deviation for horizontal positioning. For vertical positioning D-GPS is supported with IMU that measures the pressure of the air gives approximately 0.5 meters deviation. In order to decrease vertical deviation, adding an ultrasound distance sensor or vision-based sensor will provide better vertical accuracy ranges up to 2 cm.

5. CONCLUSIONS

This thesis study was aimed to reduce the usage of chemicals in plant protection applications by spotting, locating and spraying the target diseased plants. In order to detect disease in a farming field, the target plants were monitored using a multispectral camera which was mounted on a UGV and an aerial spraying UAV was used for positioning and spraying stage.

In line with this purpose in this thesis, a spraying UAV was designed, developed and tested for spot spraying mission. Conducted tests show that spraying UAV has the ability to spray pesticides above 2 meters from the ground with 4.36 m² coverage when it was hovering position in the air. It was understood from the spraying tests that it was possible to provide spraying 2.15 l/min amount of pesticide to the target using 4 nozzles with 0.45 MPa pressure. In order to spot a target in a farming field a multispectral camera was designed, developed and tested for both in laboratory conditions and in the farming field. NDVI method was used to determine the status of target plants by focusing on the photosynthesis status of the vegetation. The developed multispectral camera has the ability to capture 97 lines per sec and provides output by acquiring dark red and near-infrared bands simultaneously. For locating the diseased target a D-GPS module was integrated with the multispectral camera. And RF-transceivers was used to communicate with the base station that provides 5 km of communications distance. A UGV was also developed for carrying the plant disease detection unit while it is moving near the plants. The vehicle has the ability to carry up to 5 kg payload for a 10-degree slope in loose sand conditions. Using this developed multispectral camera that mounted on the UGV provides detection of a disease on a plant that covers about 1 cm² area from the distance 1 m height while it is scanning field line by line for horizontal FoV is 120 cm wide and the vehicle speed is around 0.33 m/s.

For aerial spraying, according to the spraying tests, while UAV is in hovering position, the ground penetration affects spraying pattern distinctively. In order to prevent this ground effect, it is possible to increase the spraying height of the UAV or it is possible to use a foldable boom or a telescopic boom holder for increasing the distance between rotors and nozzles. Positioning results show that using a D-GPS and with the help of IMUs on a UAV could provide below 1 m positioning accuracy. Big scale UAVs have a wider spraying pattern that covers the target but for mid and small scale UAV applications in order to increase their accuracy, it is a better choice to use RTK-GPS and vision sensor.

For ground monitoring, according to the field test results, the speed of the UGV is directly related to sensor output rate which mounted on it. NDVI method provides accurate results for detecting green plants and determining the diseased part in laboratory conditions. Infield study for spotting the target, resolution is a key factor for the NDVI sensor but there are also many distribution effects such as sun illumination, the vibration of the vehicle, wind speed, temperature, and humidity. For communicating with the base station, RF communication provides low-cost solutions but it limits the data transfer rate hence using an internal computer for pre-evaluating the sensor data that requires low bandwidth to overcome this problem.

After all, using an NDVI device and a GPS module on a locomotion robot could help to detect and locate the diseased area in a farming field. And spraying a predetermined location using an aerial UAV could reduce the usage of chemicals, preventing a farming field from soil compaction and saving time. When selective spraying robots used instead of the conventional methods spraying drifts will be reduced compared to the aircraft spraying, soil compaction will be decreased compared to the ground vehicles and risking human health will be eliminated when compared to the hand spraying methods.

For further studies, focusing on foldable spraying booms with lighter UAVs will be investigated for reaching better spraying patterns in aerial spraying applications. For the multispectral camera, it is possible to combine NDVI results with an RGB camera for increasing the detecting accuracy and providing more user-friendly applications.

REFERENCES

- Abdou, KH. 2018. Epidemiology of Pesticides in Developing Countries. **Advances in Clinical Toxicology** 3:1, 1–8.
- Abdulrahman, A. 2010. Remote Sensing Republic of Iraq Ministry of Higher Education and Scientific Research University of Technology, 2010.
- Ahamed, T.; Tian, L.; Zhang, Y.; Ting, K. C. 2011, A review of remote sensing methods for biomass feedstock production. **Biomass and Bioenergy**, 35:7, 2455-2469.
- Aldaz, J. (2019). Soil Compaction Robs Yields and Profits | TractorExport.com. (Online) TractorExport.com. Available at: <https://tractorexport.com/soil-compaction-robs-yields-profits/> (Accessed 2019).
- Anonymous, 2018. Resistivity-basics-formula-equation-units. Retrieved from <https://www.radio-electronics.com/info/formulae/resistance/resistivity-basics-formula-equation-units.php>
- Aparicio, N.; Villegas, D.; Royo, C.; Casadesus, J.; Araus, J. L. 2004, Effect of sensor view angle on the assessment of agronomic traits by ground level hyper-spectral reflectance measurements in durum wheat under contrasting Mediterranean conditions, **International Journal of Remote Sensing**, 25:6, 1131-1152.
- Arya, A, and A E Perelló. 2010. Management of Fungal Plant Pathogens. CABI publishing.
- Askraha, 2011. Design of laser multi-beam generator for plant discrimination. **8th International Conference on High-capacity Optical Networks and Emerging Technologies**, pp. 26-29. IEEE, Riyadh.
- Askraha, S., Paap, A., Alameh, K., Rowe, J., & Miller, C. 2016. Laser-Stabilized Real-Time Plant Discrimination Sensor for Precision Agriculture. **IEEE Sensors Journal** 16(17): 6680–86.
- AUVSI. 2013, The Economic Impact of Unmanned Aircraft Systems Integration in the United States, <https://www.auvsi.org/our-impact/economic-report>, Online.

- Azfar, A. Z., Hazry, D. 2011 Simple GUI Design for Monitoring of a Remotely Operated Quadrotor Unmanned Aerial Vehicle (UAV): **IEEE 7th International Colloquium on Signal Processing and its Applications**, Penang, 2011, pp. 23-27.
- Beyond Pesticides Daily News Blog. (2019). Court Strikes Down Aerial Pesticide Spray Ban in Lincoln County, Oregon — Challenging Local Rights to Protect Communities - Beyond Pesticides Daily News Blog. (Online) Available at: <https://beyondpesticides.org/dailynewsblog/2019/10/court-strikes-down-aerial-pesticide-spray-ban-in-lincoln-county-oregon-challenging-local-rights-to-protect-communities/> (Accessed 2019).
- Bontempo, R., Cardone, M., Manna, M. And Vorraro, G. 2014, Ducted propeller flow analysis by means of a generalized actuator disk model, **Energy Procedia**, 45, 1107-1115.
- Bradski, Gary, Kaehler, A. (2008). Learning OpenCV, Computer Vision with OpenCV Library.
- Cakıcı, F. Leblebicioglu, M. K. 2016. Control System Design of a Vertical Take-off and Landing Fixed-Wing UAV. **IFAC – PapersOnLine**, 49-3, 267-272.
- Camhi, Jonathan. 2016. The Drones Report, Online.
- Chellapilla, Kameswara R. 2016, Finite Element Analysis of Free Flexural Vibrations of a Rotor-Bearing System with Permanent Magnetic Bearings. 3. 221-230.
- Chiu, C. Lo, C. 2011. Vision-Only Automatic Flight Control for Small UAVs: Transactions On Vehicular Technology IEEE, **Transactions on Vehicular Technology**, 60:6, 2425-2437.
- Christensson, P. 2007. C/C++ Definition. <https://techterms.com>.
- Chiu, C. C., Lo, T., Tsai C. H., Chiu S. Y., 2011. Vision-Based Automatic Flight Control for Small UAVs. **Conference on Machine Vision Applications**: 348–51.
- DEOS AG, (2016), The Advantages of the CAN-Bus, https://www.deos-ag.com/en/control_technology/control-systems/can-bus, Online.

- DMCii, (2011), A multispectral image from the DMCii satellite, DMC International Imaging, Online.
- Dobberstein (2016), Emerging Use Of Drones May Change Face Of No-Tilling <https://www.no-tillfarmer.com/articles/50-emerging-use-of-drones-may-change-face-of-no-tilling>, Online.
- Eichenholz, J. 2010. Real Time Megapixel Multispectral Bioimaging, **Proc. SPIE BIOS** Vol. 7568 (2010).
- Eichenholz, J. 2010, Sequential Filter Wheel Multispectral Imaging Systems, **Proc. OSA/AIO** .
- Eisenbeis, H., 2009. UAV photogrammetry. Zurich, Switzerland:: ETH
- Fletcher (2014), You Are “Energy”, Be Energized, by Charles Fletcher. Online.
- Forelectronics, (2017), IR-Photo Diode Sensor, Retrieved from: <https://forelectronics.wordpress.com/2013/05/17/ir-photo-diode-sensor/>. Online.
- Frenzel, L. E. 2008. Principles of Electronic Communication Systems, 3rd Edition, McGraw Hill.
- Garner, w. B. 2009. Model Airplane Propellers. **DCRC Club Newsletter**, 55: 4/5.
- Glenn, E. P.; Nagler, P. L.; Huete, A. R. 2010. Vegetation Index Methods for Estimating Evapotranspiration by Remote Sensing.
- Huang, Y. Hoffmann W. C. 2009. Development Of A Spray System For An Auvsi Aerial Vehicle Platform, **Applied Engineering in Agriculture**, American Society of Agricultural and Biological Engineers, ISSN 0883-8542.
- IEEE. 2012. Remote Sensing, http://www.ieee.org/about/technologies/emerging/remote_sensing.pdf, IEEE, Online, 2012.
- ISO. 1996. Robot definition, ISO Standard Definition.
- Jenkins, D. Bijan V. 2013. The Economic Impact of Unmanned Aircraft Systems

Integration in the United States. **Association for Unmanned Vehicle Systems International** 3: 1–40. <http://www.auvsi.org/econreport>.

Jeyaratnam, J. 1990, Acute Pesticide Poisoning: A Major Global Health Problem. 43: 139–44.

JIRA. 1971. Robot definition, Japanese Industrial Robot Association (JIRA).

Katalin, S. 2011, Soil Management, Chapter 14: Precision Farming, https://www.tankonyvtar.hu/en/tartalom/tamop425/0010_1A_Book_angol_03_Foldmuveles/ch14.html

Kijewski, L. (2019). Pesticides pose risk to workers, research finds | Phnom Penh Post. (Online) Phnompenhpost.com. Available at: <https://www.phnompenhpost.com/national/pesticides-pose-risk-workers-research-finds> (Accessed 2019).

Kooistra, L. Leuven, R.S.E.W. Wehrens, R. Nienhuis, P.H. Buydens, L.M.C. 2003, A comparison of methods to relate grass reflectance to soil metal contamination. **International Journal of Remote Sensing**, 24(24):4995-5010.

Kyllo, K. P. 2003. NASA funded research on agricultural remote sensing, Department of Space Studies, University of North Dakota. <https://articles.extension.org/pages/9693/agricultural-remote-sensing-basics>

Laliberte, A. S. 2011. Multispectral Remote Sensing from Unmanned Aircraft: Image Processing Workflows and Applications for Rangel and Environments.

Ma, L. Li, M. Tong, L. Wang Y. and Cheng, L. 2013. Using unmanned aerial vehicle for remote sensing application, 2013 **21st International Conference on Geoinformatics**, Kaifeng, 2013, pp. 1-5.

Limnaios (2012), Sense and Avoid in UAS: Research and Applications.

Ma, L., Li, M., Tong, L., Wang, Y., & Cheng, L., 2013. Using Unmanned Aerial Vehicle for Remote Sensing Application. **International Conference on Geoinformatics**.

MarketsandMarkets, 2016. Crop Protection Chemicals Market by Type (Herbicides, Insecticides, and Fungicides), Origin (Synthetic, and Biopesticides), Crop Type (Cereals & Oilseeds, Fruits & Vegetables), Mode of Application, Form, and by Region - Global Forecasts to 2021.

Meriam JL, and Kraige LG., 2001. 54 Applied Mechanics Reviews **Engineering Mechanics: Dynamics**.

Meulenbroeks (2014), Aluminum versus Copper. Retrieved from <https://w3.siemens.com/powerdistribution/global/EN/tip/focus-markets/Documents/Siemens-Data-Center-Whitepaper-Aluminium-versus-Copper.pdf>

Miller, 2012. Hyperspectral and Multispectral Sensors for Remote Sensing, DALSA Teledyne white paper.

Nagler, E.P. Glenn, H. Kim, W. Emmerich, R.L. Scott, T.E. Huxman, A.R. Huete., 2007. Relationship between evapotranspiration and precipitation pulses in a semiarid rangeland estimated by moisture flux towers and MODIS vegetation indices, **A.R. Huete United States Geological Survey**, University of Arizona, USA.

NASA, 2016. Robots In Space, Nasa Facts, NF-165/7-91, https://er.jsc.nasa.gov/seh/robots_in_space.htm, Online.

NAT-GEO, 2013). National Geographic., Unmanned Flight, <http://ngm.nationalgeographic.com/2013/03/unmanned-flight/horgan-text>, Online, 2013.

Nathan L., 2009. The Bmp File Format, Retrieved from: http://www.ece.ualberta.ca/~elliott/ee552/studentAppNotes/2003_w/misc/bmp_file_format/bmp_file_format.htm.

NILabWindows, 2016. Controller Area Network (CAN) Overview, <http://www.ni.com/white-paper/2732/en/#toc3>, Online.

Niethammer, U., Rothmund S., James M. R. Travelletti, J. Joswig, M. 2010. Uav-Based Remote Sensing of Landslides. **International Archives of Photogrammetry, Remote Sensing and Spatial Information Sciences**, 38: 496–501.

- NOAA, 2013. <http://oceanservice.noaa.gov/facts/remotesensing.html>, Online, 2013.
- Paap, A., Askraha, S., Kamal, A., Rowe, J. 2008. Photonic-Based Spectral Reflectance Sensor for Ground-Based Plant Detection and Weed Discrimination. **Optics Express** 16(2): 1051.
- Piyasinghe, I., Gunatilake, J. Madawala, S., 2018, Mapping the distribution of invasive shrub *Austro eupatorium inulifolium* (Kunth) R. M. King & H. Rob: a case study from Sri Lanka. **Ceylon Journal of Science (Biological Sciences)**. 47. 95. 10.4038/cjs.v47i1.7492.
- PlantPen 300. 2018. PlantPen PRI 200 & NDVI 300.
- Propeller Theory., 2019. Retrieved from <http://www.aerodynamics4students.com/propulsion/blade-element-propeller-theory.php>.
- Rabatel, G. Gorretta, N. Labb, S., 2011. Getting NDVI Spectral Bands from a Single Standard RGB Digital Camera: A Methodological Approach. **14th Conference of the Spanish Association for Artificial Intelligence**. 10 p., La Laguna, Spain.
- Reichhardt, 2006. First Photo from Space, Retrieved from: <https://www.airspacemag.com/space/the-first-photo-from-space-13721411/>
- RIA, 1979. Robot definition, Robot Institute of America.
- Ruggiero, F., Cacace, J., Sadeghian, H. And Lippiello, V., 2015. Passivity-based control of VTOL UAVs with a momentum-based estimator of external wrench and unmodeled dynamics. **Robotics and Autonomous Systems**, 72, 139-151.
- SAHAM-METU, 2013. İnsansız Hava Aracı : <http://www.saham.metu.edu.tr/en/library.php?docid=90>, Online.
- Muhammad, S. 2015. “The Killer Chemicals as Controller of Agriculture Insect Pests: The Conventional Insecticides.” **International Journal of Chemical and Biomolecular Science**, 1(3): 141–47.

- Schowengerdt, R. A. 2007. Remote sensing: Models and methods for image processing, Academic Press, 3rd ed.
- SEOS, (2017), What is Remote Sensing, Retrieved from: <http://www.seos-project.eu/modules/remotesensing/remotesensing-c00-p02.html>
- Shinde, S. N., Chorage, S. S. 2016. Unmanned Ground Vehicle, **International Journal of Advanced Engineering, Management and Science (IJAEMS)**, 2(10): 1659-1662.
- SIPRI, (2016), SIPRI Military Expenditure Database, Retrieved from <https://www.sipri.org/databases/milex>.
- Soil Works LLC. 2019. Compaction. Available at: <https://soilworksllc.com/compaction/> (Online).
- Soto M.G., Emmi L., 2016. Autonomous systems for precise spraying e Evaluation of a robotised patch sprayer, **Robotic Agriculture**, IAgRE, 47: 148-156.
- Sprayers101, 2016. How to Use a Nozzle Flow Chart, With a Surprising Twist, <http://sprayers101.com/how-to-use-a-nozzle-flow-chart-with-a-surprising-twist/>, Online.
- SRAeuRobotics, .014. Strategic Research Agenda 2014-2020, euRobotics, AISBL
- Brandon, S., Smith, B., Chen, Y. Q., 2013. A Guide for Selecting Small Unmanned Aerial Systems for Research-Centric Applications. 2 IFAC Papers Online 46 (30): 38-45.
- Stroustrup, B. 1989. Mol Plant Microbe Interact The C++ Programming Language 3rd Edition.
- TCTOB. 2017. 2018 yılı Bitki Sağlığı Uygulama Programı, https://www.tarimorman.gov.tr/GKGM/Belgeler/BitkiSağlığı/Hizmetleri/bitki_sagligi/Bitki-sagligi-uygulamakitaplari/2018_Bitki_Sagligi_Uygulama_Programi.pdf, Online.
- Teal Group, (2017), World Military Unmanned Aerial Vehicle Systems, Market Profile and Forecast 2017, <https://www.tealgroup.com/index.php/pages/press-releases/47-teal-group-predicts-worldwide-military-uav->

production-of-80-billion-over-the-next-decade-in-its-2017-uav-market-profile-and-forecast, Online.

Tirgul, C., S., Naik M., R., 2016. Artificial Intelligence and Robotics, **International Journal of Advanced Research in Computer Engineering & Technology (IJARCET)**, 5: (6).

Toscano, 2016. CEO of AUVSI: Association for Unmanned Vehicle Systems International, AUVSI Interview: Michael Toscano, <http://dronecenter.bard.edu/interview-michael-toscano/>, Online.

Turner, M. 2009. Where Australian Robotics Are At **Educational Technology Solutions**, Retrieved from <https://tribotix.com/why-robotics-article/>

U.S. Department of Defense, 2013. U.S. Department of Defense, UAV Evolution - Where are we? : <Http://www.defense.gov/specials/uav2002/>, Online.

Udelhoven, T., 2012. The use of an UAV as a remote sensing platform in agricultural applications: BMR 2012 Forum Luxinnovation.

Unmanned Vehicle University, 2016. The Sky's the Limit if You Have What it Takes, <http://www.uxvuniversity.com/>, Online.

US-ARM, 2010. Army UAS CoE Staff "Eyes of the Army" US Army Road Map for UAS 2010-2035.

Wang, Fu-min; Huang, Jing-feng; Tang, Yan-lin; Wang, Xiu-zhen., 2007. New Vegetation Index and Its Application in Estimating Leaf Area Index of Rice, **Rice Science**, 14: 195-203.

Watts, A.C.; Ambrosia, V.G., Hinkley, E.A., 2012. Unmanned Aircraft Systems in Remote Sensing and Scientific Research: Classification and Considerations of Use, **Remote Sens.** 4: 1671-1692.

Way, M. J. The Natural Environment and Integrated Methods of Pest Control. **Journal of Applied Ecology**, 3, 29-32. doi:10.2307/2401441

Wetzel, S, L C Duchesne, and M F Laporte. 2006. Bioproducts From Canada's Forests: New Partnerships in the Bioeconomy. **Springer**, Netherlands.

- Wu, L., Li, L., Li, B., Zhang, J., & Wang, A. (2015). Magnetic, durable, and superhydrophobic polyurethane@Fe₃O₄@SiO₂@fluoropolymer sponges for selective oil absorption and oil/water separation. **ACS applied materials & interfaces**, 7 8, 4936-46 .
- Xie, H.; Tian, Y. Q., Granillo, J. A., Keller, G. R., 2007. Suitable remote sensing method and data for mapping and measuring active crop fields, **Remote Sens.** 28: 395-411.



RESUME

Personal Information

Name and Surname : Fatih AKKOYUN

Place and Date of Birth : Afyonkarahisar, 28/05/1984

Education

Undergraduate (BSc):

Kocaeli University (2005-2009)

Faculty of Technical Education

Department of Electronics and Computer Education

Postgraduate (MSc):

Kocaeli University (2009-2011)

Faculty of Technical Education

Department of Electronics and Computer Education

Postgraduate (PhD):

Aydın Adnan Menderes University (2013-2019)

Graduate School of Natural and Applied Sciences

Department of Mechanical Engineering

Foreign Languages : English

Scientific Activities

Publications.

Demirciođlu Pınar, Böđrekci İsmail, **Akkoyun Fatih**, Yavařođlu Hüseyin, Özel Kesit Profil Flap Diskinin Üretim Performansının Belirlenmesi, 1, 2018

Akkoyun Fatih, Böđrekci İsmail, Demirciođlu Pınar, Vardin Salih , An Experimental Study to Investigate the Effect of the Angle of Attack on VTOL UAV Propellers, Elsevier, 9, 2018

Presentations.

Böđrekci İsmail, Demirciođlu Pınar, **Akkoyun Fatih**, Kösem M Alptekin, Development of Load Cell and Real-Time Force Measurement System, Welmo 2017, 06.05.2017

Sucuođlu Hilmi Saygın, **Akkoyun Fatih**, Demirciođlu Pınar, Böđrekci İsmail, Çoklu Sensör Yaklaşımıyla Erken Algılama Sisteminin Geliştirilmesi, TÜYAK 2015, 13.11.2015

Demirciođlu Pınar, Böđrekci İsmail, **Akkoyun Fatih**, Yavařođlu Hüseyin, Performance of Tailor Made Production of Flap Disc for Special Section Profile, 8th International Conference and Exhibition on Design and Production of MACHINES and DIES/MOLDS, 20.06.2015

Akkoyun Fatih, Erkan Kadir, Fpga Tabanlı Dokunmatik Ekranlı Kullanıcı Arabirimi Tasarlanması Ve Gerçekleştirilmesi, Fırat Üniversitesi Elektrik-Elektronik ve Bilgisayar Sempozyumu, 01.01.2011.

Book Chapters.

Proceedings of the International Symposium for Production Research 2018 , Bilimsel Kitap , Bölüm(ler),Implementation of a Real-Time Data Acquisition System with Wireless Sensor Network for Temperature Measurement, Böđrekci İsmail, **Akkoyun Fatih**, Demirciođlu Pınar, Vardin Salih, Durakbasa, Numan M. Gencyilmaz, M. Günes,2019,978-3-319-92267-6

Proceedings of the International Symposium for Production Research 2018 , Bilimsel Kitap , Bölüm(ler),Design and Development of Human Machine

Interface for Unmanned Aerial Vehicle Control, **Akkoyun Fatih**, Böğreki İsmail, Demirciođlu Pınar, Vardin Salih, Durakbasa, Numan M. Gencyilmaz, M. Günes,2019,978-3-319-92267-6

Contact

e-mail: fatih.akkoyun@adu.edu.tr

Address: Aydın Adnan Menderes Üniversitesi, Mühendislik Fakültesi,
Makina Mühendisliği Bölümü, PK:09100 Efeler/AYDIN.

Phone: +90 (256) 213 7503

.././2019

AYDIN